

Mechanical Micromachining—Effect of Crystallographic Anisotropy on Machining Forces

Submitted in partial fulfillment of the requirements for

the degree of

Doctor of Philosophy

in

Mechanical Engineering

Nithyanand Kota

B.Tech, Mechanical Engineering, Indian Institute of Technology Madras

M.Tech., Intelligent Manufacturing, Indian Institute of Technology Madras

Carnegie Mellon University

Pittsburgh, PA

May, 2011

*To my parents,
Vasanthi and K.P. Aithal,*

Acknowledgements

The research presented in this thesis benefited from the insights and direction of many people. I have worked with a large number of people whose contributions deserve special mention. It is a pleasure to convey my gratitude to them.

First and foremost, I want to thank my advisor Prof. Burak Ozdoganlar for his guidance, mentoring and support during the past five years. His encouragement, combined with his constructive and insightful criticism has helped me continuously improve myself and my work. The more I look back at the time I have spent as his graduate student, the more I realize his effort towards my overall development as an independent researcher. I am also thankful for the drive and the energy he brings to research which have been a constant source of inspiration for me, and have provided an example that I hope to emulate for the rest of my life.

I wish to thank Prof. Anthony Rollett for his technical guidance on the various aspects of research during my doctoral studies. I greatly appreciate his patience in answering my queries despite his busy schedule. I have immensely benefitted from his vast experience through the interactions with him, both inside and outside the classroom.

I wish to thank my committee members, Prof. Fred Higgs and Prof. Philip LeDuc for serving on my committee and providing helpful suggestions regarding my research and its presentation. I also want to thank them for helping me obtain an important perspective on the applicability of my research.

I want to thank Prof. Amit Acharya, Prof. Kaushik Dayal, Prof. Craig Maloney and Prof. Greg Rohrer for helping me gain a formal understanding of the different aspects related to my research through the courses they offered. I also want to thank Prof. Yoosuf Picard for his assistance in performing the subsurface deformation measurements and Prof. Jeremy Michalek for providing the SuperEGO code.

I would like to acknowledge the financial support of the National Science Foundation and the Materials Research Science and Engineering Center of Carnegie Mellon University.

I want to thank Jim Dillinger, John Fulmer and Ed Wojciechowski of the Mechanical Engineering machine shop for their help during the experimental stages of my research. I want to thank Tom Nuhfer and Jason Wolf for their assistance in various microscopy techniques. I also want to thank Dolores Smiller, Bobbi Kostyak and Chris Hertz for their assistance in administrative issues. I

want to thank Jon Ledonne and Herb Miller for their assistance in various materials science related experimental procedures.

My stay in the basement office became more enjoyable in the company of my colleagues and friends. Thanks to Prashanth and Arda for the great company and support they provided during the past five years. I could not have asked for better lab mates. Thanks to Shin Hyung and JuEun for their company and support during the course of my PhD. I would like to thank Gerardo for initiating the coffee time sessions, and, Bekir and Recep, for participating in it. I want to thank my friends Amith, Sunil Prasad, Rahul, Piyush, Bharath, Trivikram, Ajay, Rohit, Kandarp, Vinay and Yogish for keeping me motivated during my PhD.

I want to greatly thank my brother Sadanand for his support, encouragement and advice throughout my academic life and especially so during my doctoral studies. The beneficial role he played, conscious and otherwise, in shaping my career cannot be overemphasized. I also want to thank my cousins, Vivek and Shashishekar, for their support during my graduate study.

Lastly, and most importantly, I want to thank my parents, Vasanthi and K.P. Aithal, for their unconditional love, support and encouragement. I also want to thank them for fully supporting my decisions throughout my academic life. Without their sacrifices towards my education and career, this thesis work would not be possible. For all their love and support, I dedicate this thesis to them.

Abstract

With increased application of mechanical micromachining for creating small features with complex geometries on a broad range of materials, the need for understanding the mechanics of machining at the micro-scale has been recognized. During mechanical micromachining of metals, the tool-workpiece interaction occurs entirely within either a single crystal or a few crystals of the workpiece material. Consequently, the crystallographic properties (e.g., anisotropy) of individual crystals strongly affect the machining response, including micromachining forces and resulting surface finish. Hence, the crystallographic effects that are generally neglected (due to the perceived isotropic nature of the workpiece) in macro-scale machining need to be studied both experimentally and theoretically for gaining a better understanding of the micromachining process.

This thesis aims to understand the effects of crystallographic anisotropy on machining response of face centered cubic metals through physics-based modeling and experimental analysis. The thesis begins with an introduction to micromachining and the associated crystallographic effects on the micromachining response. Subsequently, a literature review is presented and the shortcomings of the available research are identified. In particular, (a) the lack of physically realistic machining force models incorporating the effects of anisotropy, and (b) a necessity for experimental data analyzing the effect of anisotropy over a broad range of machining conditions, are addressed. The work is performed in three stages, with the first two addressing the former, and the last one addressing the latter shortcoming.

First, a simplified machining force model incorporating the effects of anisotropy is developed by combining a plasticity theory and the Merchant's machining model. Since the deformation geometry is unknown *a-priori* in machining operations, a shear angle determination scheme is necessary before predicting the forces. For a given crystallographic orientation, the model considers the minimization of the total power, including the shearing (plastic) and rake-face friction power, to determine the shear angle and predict the machining forces. The calculation of shearing power is performed using the Bishop and Hill's plasticity theory, thus incorporating the effects of anisotropy. The model is calibrated and validated using the available (but limited) machining force data from the literature. An analysis of the model is also performed to observe the effects of orientation, friction angle and rake angle. The simplified model neglected the effects of hardening and lattice rotation observed during large strain deformation (such as that experienced in machining).

Second, a more physically realistic rate sensitive plasticity-based machining (RSPM) force model is developed to enhance the simplified model by incorporating the hardening and lattice rotation

effects. Similar to the simplified model, minimization of the total power (sum of plastic and friction power) is used to determine the shear angle. When calculating the required plastic power, rate-sensitive constitutive equations with hardening and kinematics of single crystal deformation (including lattice rotation) are used. The obtained shear angle is then used to predict the machining forces. The RSPM model is calibrated using the Kriging-algorithm-based SuperEGO (efficient global optimization) code to obtain the five material parameters required. Both the calibration and the subsequent validation are performed using the machining force data available in the literature. Use of the RSPM model improved the match with the experiments over the use of the simplified model. The RSPM model is then used to analyze the effects of orientation, rake angle, coefficient of friction and material properties on machining forces.

Third, to address the need for comprehensive experimental data and analysis, a precision turning and a precision planing apparatus are designed and constructed. Initial machining experiments performed on single crystal and coarse-grained polycrystal aluminum showed that the machining force and surface finish values vary strongly with crystallographic orientations. A measurement of deformation below the cut surface also indicated the importance of measuring the subsurface deformation in future studies. Subsequently, a comprehensive study on the effect of anisotropy over a range of cutting parameters is performed for coarse-grained polycrystal aluminum. In these experiments, in addition to the machining parameters, the effect of subsurface deformation is studied by comparing experimental results from cases with and without cleanup cut. The results from these experiments quantified the effects of crystallographic anisotropy, its interaction with machining parameters and the effect of sub surface deformation on machining forces and surface finish.

The thesis concludes with a discussion of future work covering both modeling and experimental aspects of the research. The future work is divided into near term and long term future work, where the near term work includes planing and plunge turning experiments on single crystals and the extension of the RSPM model to oblique machining. In the longer term, modifications to the machining force model to include the non homogeneity of the shear zone, and extension of the model to three dimensional machining operations like milling are proposed.

The fundamental contributions of this thesis research are focused on modeling and experimental investigations on single-crystal and coarse-grained materials. Specific contributions include; (1) A simplified machining model that includes the crystallographic anisotropy; (2) A comprehensive rate-sensitive plasticity-based machining force model including hardening and crystal rotation effects and large deformations; (3) An experimental infrastructure, including precision planing and plunge-

turning testbeds, to facilitate experimental investigations and model validations in the presence of crystallographic effects; and (4) An experimental understanding on the effects of crystallography when micro-machining single-crystal and coarse-grained materials.

Contents

Acknowledgements	ii
Abstract	iv
List of Figures	xi
List of Tables	xv
1 Introduction	1
1.1 Basics of Machining Process	2
1.1.1 Plastic Deformation in Metals	4
1.2 Literature Review	6
1.3 Research Objectives	11
1.4 Research Contributions	11
2 A Simplified Model for Orthogonal Machining of FCC Single-crystal Materials	12
2.1 Model Description	13
2.1.1 Calculation of Plastic Power	13
2.2 Calculation of Forces and Power	17
2.2.1 Solution Procedure	18
2.3 Model Validation	19
2.3.1 Validation for Fixed Zone Axis	19

2.3.2	Validation for Fixed Cutting Plane	23
2.4	Model application	24
2.5	Model Simplification using Merchant's Shear Angle	29
2.6	Summary	32
3	Rate Sensitive Plasticity based Machining Model	35
3.1	Model description	35
3.2	Calculation of Plastic work	37
3.2.1	Plastic deformation in single-crystal fcc metals	38
3.3	Incremental plastic work	41
3.3.1	Calculation of incremental plastic strain	41
3.3.2	Calculation of the stress tensor	43
3.3.3	Determination of lattice reorientation	45
3.3.4	Incorporation of strain hardening	45
3.4	Modeling procedure	46
3.5	Calibration	48
3.5.1	Calibration Procedure	48
3.5.2	Calibration for Aluminum and Copper	50
3.5.3	Selection of the incremental strain value	50
3.6	Validation of the model	51
3.7	Model Analysis	51
3.7.1	Lattice rotation and hardening	52
3.7.2	Effect of material properties	53
3.8	Model application	55
3.8.1	Effect of the zone axis	56
3.8.2	Effect of rake and friction angles	71
3.9	Simplification of the model using Merchant's shear angle	73

3.10	Summary	74
4	Experimental Setups for Planing and Plunge-turning of Single Crystals and Coarse Grained Polycrystals	78
4.1	Motivation	78
4.2	Planing apparatus	79
4.2.1	Tool characterization	80
4.3	Turning apparatus	81
5	Machining of Coarse Grained Aluminum Including Crystallographic Effects	84
5.1	Experimental Methods	85
5.1.1	Experimental Facility	85
5.1.2	Tool Characterization	85
5.1.3	Workpiece Characterization	88
5.1.4	Cutting Conditions	89
5.1.5	Experimental Procedure	89
5.2	Results and Discussion	91
5.2.1	Machining after Cleanup Cuts	93
5.2.2	The Main Effects of Crystallographic Anisotropy	94
5.2.3	Machining Surfaces without Cleanup	102
5.2.4	Analysis of Surface Roughness	104
5.3	Comparison with the model	106
5.4	Summary	108
6	Experiments on Single Crystal Aluminum	110
6.1	Orthogonal machining of aluminum single crystals	110
6.1.1	Measurement of subsurface deformation	112
7	Conclusions	114

8	Future Work	117
8.1	Near Term Work	117
8.1.1	Experimental Measurement of Subsurface Deformation	117
8.1.2	Orthogonal Machining of Single Crystals	118
8.1.3	Oblique Machining of Single Crystals	118
8.2	Long term work	119

List of Figures

1.1	Examples of micro machined features (a) PMMA micro pillars, (b) Stainless steel gear, (c) Brass mold (for microfluidic devices), and (d) Green state ceramic wall. . .	2
1.2	Comparison between (a) Macro scale machining, and (b) Micro scale machining. . .	3
1.3	Basic machining geometries (a) Orthogonal machining, and (b) Oblique machining. .	3
1.4	Orthogonal machining nomenclature.	4
1.5	(a) Edge dislocation in a lattice and its motion, (b) Face centered cubic unit cell. . .	5
1.6	(a) Planing configuration, (b) Plunge-turning configuration, and (c) In-plane machining	8
2.1	(a) A depiction of the orthogonal cutting process with the Merchant's cutting force diagram, and (b) the coordinate system used for model derivation.	14
2.2	Definition of the orientation angle for fixed zone axis. A disk-type workpiece is considered in plunge-turning configuration.	16
2.3	The experimental data used for the calibration of the model for aluminum single-crystal machining with fixed zone axis ([0 0 1]); and the model with the calibrated CRSS value of 67 MPa: (a) Specific cutting energies, and (b) Shear angles.	20
2.4	The variation of calculated specific total power with shear angle candidates and orientation angles. The solid line indicates the minimum specific power.	21
2.5	Comparison of the model predictions and experimental data for aluminum single-crystal machining with fixed zone axis of [0 0 1]:(a) Specific cutting energies and (b) Shear angles.	22
2.6	Comparison of the predicted and experimentally obtained specific energies for copper single-crystal machining with fixed zone axis of [0 0 1].	23
2.7	Sample, crystal, and cutting orientations for the fixed cutting plane experiments and validation in planing configuration.	24
2.8	(a) Simulated variation in cutting force on (1 1 0) plane, (b) Experimental variation in cutting force on (1 1 0) plane [40], c) Simulated variation in cutting force on (1 1 1) plane and (d) Experimental variation in cutting force on (1 1 1) plane [40].	25
2.9	The standard stereographic triangle and the zone axes selected for the analysis. . .	26
2.10	The effect of zone axis on specific cutting energy.	27
2.11	The parameters that are defined to describe the specific energy variation with orientation angle for given zone axis. In addition to the shape of the curve, the mean value M , the amplitude Ω , and the phase angle η are defined.	28
2.12	The effect of $(\beta - \alpha)$ on (a) mean value of specific cutting energy and (b) mean value of specific thrust energy.	29

2.13	The effect of $(\beta - \alpha)$ on (a) the deviation of the specific energies, and (b) the phase angle of the specific energies.	30
2.14	The effect of $(\beta - \alpha)$ on mean value of shear angles for all analyzed zone axes. . . .	31
2.15	(a) Cutting and crystallographic orientations indicating the reversal of cutting direction, (b) Comparison of variation in specific cutting energy for forward and reverse direction with orientation angle for $[0\ 0\ 1]$ zone axis.	32
2.16	Comparison between specific energies calculated for $[2\ 1\ 2]$ zone axis using the complete model and using the simplified model with Merchant's shear angle.	33
3.1	(a) The geometry of orthogonal cutting process, indicating the workpiece zone axis $[abc]$, cutting direction $[hkl]$, and cutting plane normal $[uvw]$, and (b) Components of the machining force, Merchant's force-circle diagram, and the shear zone.	57
3.2	(a) Deformation in the primary deformation zone, (b) An incremental deformation $\Delta\gamma$ that occurs as a result of incremental plastic work ΔW_p^k	58
3.3	Illustration of the lattice rotation; the final deformation is a result of slip on (a) only one system (along 1_l), and (b) two slip systems (simultaneously along 1_l and 2_l), and a rotation. The same deformation is obtained with different lattice orientations. . . .	59
3.4	Typical behavior of reference stress.	59
3.5	Typical behavior of total power with shear angle candidates.	60
3.6	(a) Typical specific energy data from experiments as it varies with the orientation angle θ of the cutting plane, and (b) the definition of the zone axis, cutting direction, and cutting-plane orientation.	60
3.7	Typical iterations during the Kriging-based calibration procedure: (a) iteration points for the material parameters, and (b) the root mean squared error between the experimental data and the model with specified parameters. The first 60 steps involve a space-filling design-of-experiments.	61
3.8	Comparison of experimental and predicted specific cutting energy for (a) aluminum and (b) copper for the calibration cases.	61
3.9	Choice of incremental strain $\Delta\gamma$ through convergence: (a) Variation of plastic power for cutting direction $[hkl] = [100]$, cutting plane normal $[uvw] = [010]$, and zone axis $[abc] = [001]$ (see Fig. 1.6(a)) (the candidate shear angle for the graph shown is 39 degrees); and (b) percentage variation from limiting value with decreasing $\Delta\gamma$. The selected $\Delta\gamma$ value is identified in the figures with dashed lines.	62
3.10	Validation case: comparison of the specific energies from the model and from experiments for single-crystal aluminum for the zone axis of $[0\ 0\ 1]$	62
3.11	The effects of hardening and lattice rotation on specific energy: (a) and (b) no hardening and no lattice rotation; (c) and (d) hardening without lattice rotation; (d) and (f) lattice rotation without hardening cases. The former of each pair is for $[0\ 0\ 1]$ zone axis, and the latter is for $[1\ 0\ 1]$ zone axis. The full RSPM model (hardening and lattice rotation) is used as the reference for each case.	63
3.12	Definition of the metrics used for analyzing the effect of different parameters: M is the mean value, and Ω is the amplitude (about the mean) of the specific energy as it varies with the orientation angle.	64
3.13	Effect of material parameters on mean M and amplitude Ω of specific energies for <i>aluminum</i> : (a)-(f) The exponent of the power law a ; (b)-(g) the initial reference stress τ_o ; (c)-(h) the saturation stress τ_v ; (d)-(i) the initial hardening slope Θ_o ; and (e)-(j) the exponent of rate sensitivity n	65

3.14	Effect of material parameters on mean M and amplitude Ω of specific energies for <i>copper</i> : (a)-(f) The exponent of the power law a ; (b)-(g) the initial reference stress τ_o ; (c)-(h) the saturation stress τ_v ; (d)-(i) the initial hardening slope Θ_o ; and (e)-(j) the exponent of rate sensitivity n	66
3.15	Comparison between the (a) variation of the specific energy and (b) variation of the cumulative slip about $[0\ 0\ 1]$ axis for aluminum ($\alpha = 40$ deg. and $\beta = 50$ deg.). . . .	67
3.16	(a) The material model (plastic stress versus cumulative slip) with the hardening effect; and the effects of (b) the initial reference stress, (c) the saturation stress, (d) the initial hardening slope, and (e) the exponent of the power law on the material model.	67
3.17	The selected zone axes in the basic stereographic triangle.	68
3.18	The effect of zone axis on specific cutting energy for aluminum for zone axes (a) $[0\ 0\ 1]$, (b) $[1\ 0\ 1]$, (c) $[1\ 0\ 2]$, (d) $[1\ 1\ 1]$, (e) $[1\ 1\ 2]$, (f) $[2\ 1\ 2]$, (g) $[2\ 1\ 3]$, and (h) $[2\ 1\ 6]$	68
3.19	The effect of zone axis on (a) the mean and (b) the deviation of specific cutting energy for aluminum (<i>color online</i>).	70
3.20	The effect of zone axis on (a) the average cumulative slip and (b) the average lattice rotation for aluminum (<i>color online</i>).	71
3.21	Orthogonal machining geometry.	72
3.22	Variation of (a) the mean and (b) the amplitude with the rake and friction angles for aluminum (<i>color online</i>).	73
3.23	(a) The proportion of (average) power spent in plastic deformation (to total power) and (b) the actual power spent in plastic deformation for aluminum across the range of rake and friction angles (<i>color online</i>).	74
3.24	Comparison between the specific cutting energy obtained using Merchant's shear angle and that from the complete model including minimization of total work for (a) $[0\ 0\ 1]$, (b) $[1\ 0\ 1]$, (c) $[1\ 1\ 1]$, and (d) $[2\ 1\ 2]$ zone axes.	75
4.1	Planing apparatus.	80
4.2	Replica based measurement procedure (a) Aluminum workpiece, (b) Replica material applied on top of the workpiece, and (c) Replica removed for measurement. The process is repeated after the prescribed cut and the two replicas are compared for depths at the location marked by ridges for obtaining the actual uncut chip thickness.	81
4.3	(a) Diamond tool design, (b) Holder for adjusting the rake angle, (c) Holder for adjusting the inclination angle, (d) Tool assembly with rake angle adjusted, and (e) Tool assembly with rake and inclination angles adjusted.	82
4.4	Turning apparatus.	83
4.5	Single crystal workpiece.	83
5.1	(a) Planing apparatus and (b) Schematic for machining coarse grained workpieces. . . .	86
5.2	Replica based measurement procedure (a) Aluminum workpiece with the wall feature, (b) Replica material applied on top of the workpiece, and (c) Replica removed for measurement. The process is repeated after each cut and the depth of the replicas are measured at ridge locations to obtain the actual uncut chip thickness.	87
5.3	(a) Workpiece 1 and (b) Workpiece 2 with traced grain maps.	88
5.4	Projections of (a) Cutting plane normals and (b) Cutting directions, in the standard stereographic triangle.	89

5.5	Kinematics of the orthogonal cutting and the Merchant's force circle diagram.	91
5.6	Typical specific energy variations for (a) Workpiece 1 and (b) Workpiece 2, for 0 degree rake angle, 10 mm/s cutting velocity, and 40 μ m uncut chip thickness.	92
5.7	Main effect plots for (a-d) Specific cutting energy and (e-h) Effective coefficient of friction.	95
5.8	Schmid factors for the resultant machining force directions.	96
5.9	Effect of rake angle on specific cutting energy signatures at various cutting conditions for (a-c) Workpiece 1 and (d-f) Workpiece 2, at 10 mm/s cutting velocity. The guidelines show the approximate midpoint of each grain for visual correlation only.	97
5.10	Two- way interaction effects for specific cutting energy between (a) the grain orientation and the rake angle and (b) the grain orientation and the uncut chip thickness.	98
5.11	Two- way interaction effects for specific cutting energy between (a) the grain orientation and the rake angle, (b) the grain orientation and the cutting velocity, and (c) the grain orientation and the uncut chip thickness.	99
5.12	Effect of uncut chip thickness on specific cutting energy signatures at various cutting conditions for (a-c) Workpiece 1 and (d-f) Workpiece 2, at 50 mm/s cutting velocity. The guidelines show the approximate midpoint of each grain for visual correlation only.	101
5.13	Typical effect of cleanup cut on specific cutting energy for (a) Workpiece 1 and (b) Workpiece 2.	102
5.14	(a) Main effect of cleanup cut and (b) Two- way interaction effect for specific cutting energy between (a) the grain orientation and the cleanup cut.	103
5.15	(a-d) Main effect plots for surface roughness, and (e-f) Two- way interaction effects for surface roughness between (e) the grain orientation and the rake angle, and (f) the grain orientation and the uncut chip thickness.	106
5.16	Comparison between (a) Experimental specific cutting energy and (b) Predicted specific energy (scaled) from the RSPM model, at 25 degree rake angle	107
6.1	Cutting force variation about (a) [0 0 1] and (b) [1 1 1] zone axis	111
6.2	Cutting force variation about (a) [1 0 1] zone axis, and (b) alternation of force at orientation about [1 0 1] zone axis under planing	112
6.3	Orientation imaging (a) Capping Platinum layer, (b) Orientation map and (c) Mis-orientation along the depth of workpiece	113
8.1	(a) Reference nickel and (b) GBE nickel (source:www.integran.com)	122
8.2	(a) Machining force comparison, (b) Main effects plot, and (c) Interaction plot	123

List of Tables

1.1	Experimental studies on single-crystal machining from the literature, and associated machining parameters.	6
3.1	Material parameters obtained from calibration for single-crystal aluminum and single-crystal copper.	50
4.1	Variation in uncut chip thickness.	81
5.1	Results of the preliminary study to measure the difference between the actual and prescribed uncut chip thicknesses.	87
5.2	Orientations of the grains.	90
5.3	Experimental conditions for orthogonal machining studies.	90
5.4	ANOVA results for the specific cutting energy and the effective coefficient of friction, where “*” denotes the interaction between two parameters.	93
5.5	ANOVA results for the surface roughness, where “*” denotes the interaction between two parameters.	105
8.1	ANOVA results for machining of GBE materials.	123

Chapter 1

Introduction

As current trends towards miniaturization accelerate and ever more applications are realized, garnering a comprehensive understanding of the micro-manufacturing processes becomes imperative for optimizing current technologies and developing future technologies. Mechanical micromachining, which includes the application of traditional machining techniques such as milling, drilling, and turning to the micro scale, is gaining momentum as a flexible and efficient way to make truly three-dimensional micro-scale features and parts from a wide selection of materials [1–14] (see Fig. 1.1). Although kinematically similar, micromachining is fundamentally different from conventional (macro) machining.

An important difference arises from the considerable effect of workpiece microstructure on the micromachining processes. Characteristic dimensions of crystals in metals are commensurate with the uncut chip thickness values experienced in micromachining (see Fig. 1.2(b)). Therefore, the process takes place within individual crystals or within a few crystals at a time. Since elastic and plastic behavior of individual crystals are anisotropic, the mechanical properties vary when passing through different grains. Therefore, machining response, including forces, chip-thickness ratio, lamellae structure, surface finish, built-up edge and side flow will vary during the process. In contrast, since a large number of grains are encountered during macro-scale cutting processes, an averaged effect from the workpiece microstructure is experienced, and the material can usually be assumed to behave isotropically (see Fig. 1.2(a)).

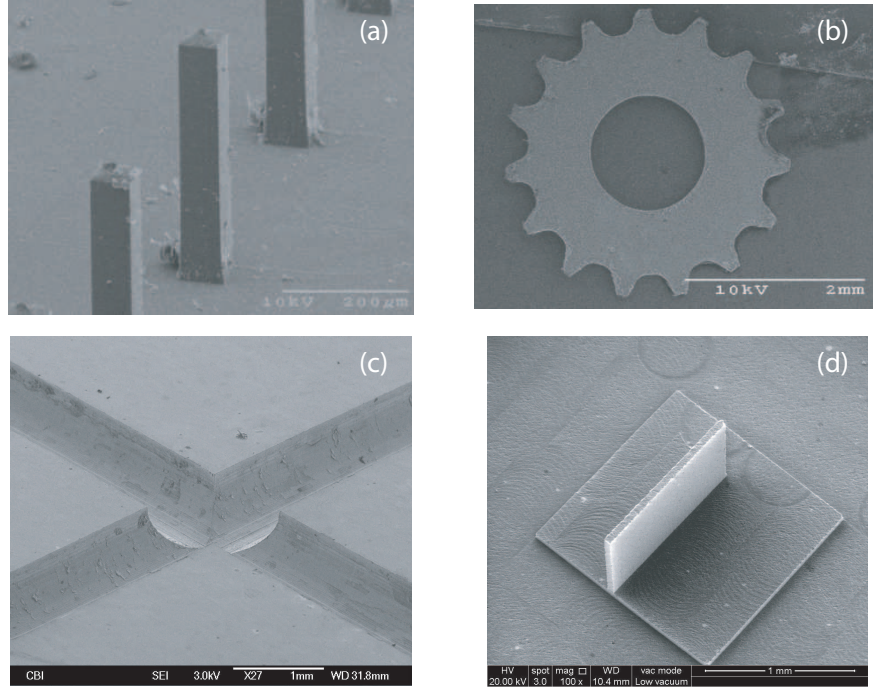


Figure 1.1: Examples of micro machined features (a) PMMA micro pillars, (b) Stainless steel gear, (c) Brass mold (for microfluidic devices), and (d) Green state ceramic wall.

1.1 Basics of Machining Process

Machining is a manufacturing process involving removal of thin layer of material (often called the chip) from a larger body (workpiece) using a tool. Most common machining operations include milling, drilling, boring, turning and broaching. Even though the actual operations can involve complicated tool, workpiece interaction geometries, all the machining processes can be modeled based on two basic geometries. These are orthogonal and oblique machining geometries shown in Fig. 1.3.

In orthogonal machining, the cutting edge is perpendicular to the cutting velocity, whereas, in oblique machining the cutting edge makes an inclination angle (λ) with respect to the cutting velocity normal. In both cases the chip formation happens through material separation at the cutting edge. Furthermore, the chip undergoes severe plastic deformation as it separates from the workpiece. Considering the focus of the current thesis, only the orthogonal machining geometry is described in detail here.

Figure 1.4 shows the various deformation zones and the nomenclature for the orthogonal machining geometry. The deformation of the chip mostly occurs in the primary deformation zone

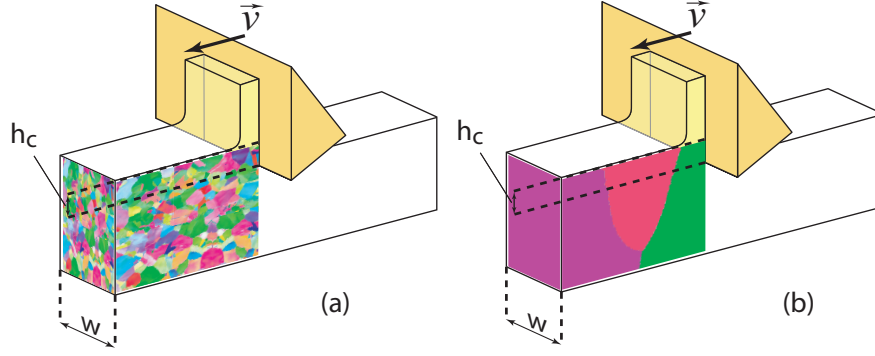


Figure 1.2: Comparison between (a) Macro scale machining, and (b) Micro scale machining.

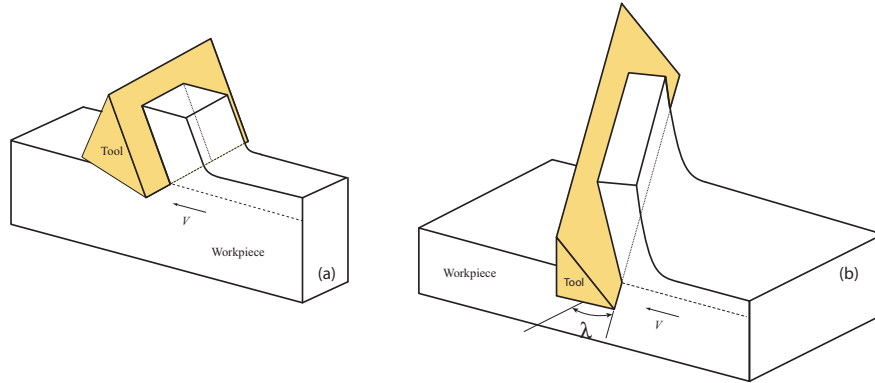


Figure 1.3: Basic machining geometries (a) Orthogonal machining, and (b) Oblique machining.

(PDZ) and the rubbing of the chip on tool face occurs in the secondary deformation zone (SDZ) as shown in Fig. 1.4. Orthogonal machining with continuous chip formation can be modeled as a steady state process. Researchers have used various approaches to model the machining problem, including mechanistic, empirical and numerical procedures.

Of all the available models, Merchant's machining model is frequently cited for its simplicity and effectiveness in capturing the machining kinematics [15]. Merchant idealized the machining process by considering the PDZ as a thin straight plane and the SDZ as a friction zone [16]. The angle the shear plane makes with the cutting velocity is known as the shear angle (see Fig. 1.4). Shear angle determines the amount of deformation and is unknown *a-priori* during machining operation.

In his machining model, Merchant identified the various velocities (viz., shear velocity, chip velocity) and forces involved in machining and arrived at governing relationships between them for a given shear angle. The velocity triangle and the Merchant's force circle diagram provide a graphical representation of these relationships. Furthermore, Merchant arrived at a scheme for

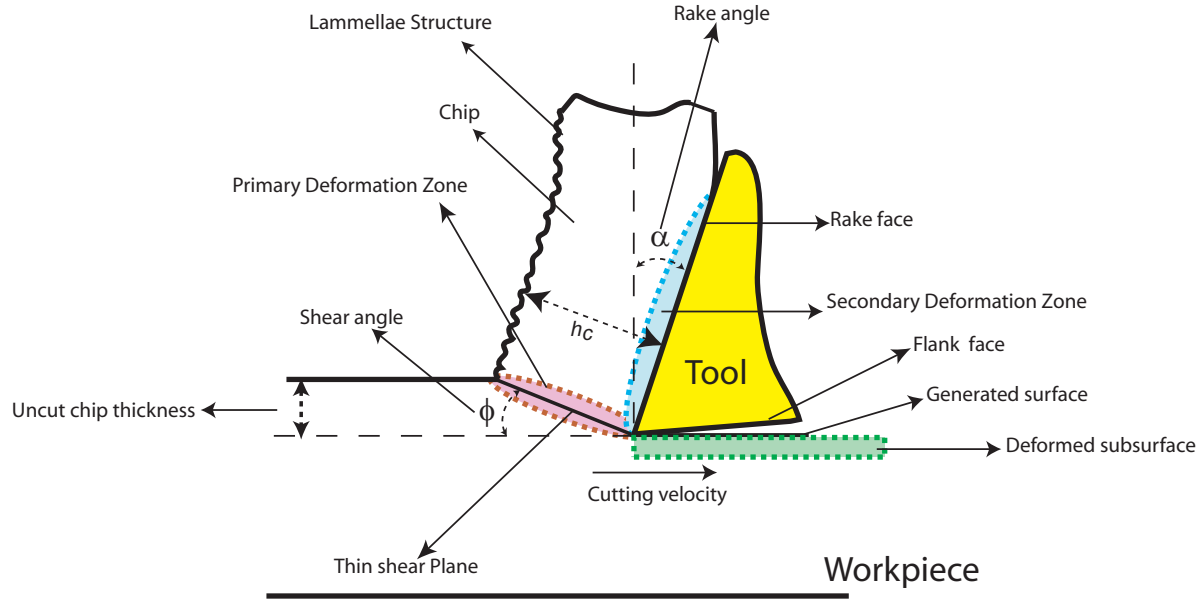


Figure 1.4: Orthogonal machining nomenclature.

determining the shear angle by minimizing the total power, including plastic power in PDZ and friction power in SDZ, consumed during machining. Such power calculation requires the knowledge of both, material behavior and friction conditions on the rake face.

1.1.1 Plastic Deformation in Metals

Plastic deformation in metals under most conditions is the result of the motion (also called slipping or glide) of line defects called dislocations (for example edge dislocation in Fig. 1.5(a)) on particular planes, called slip planes, in particular directions, called slip directions. The motion of dislocation does not result in the volume change of the material, consequently plastic deformation is an iso-volume process.

For face centered cubic (fcc) metals, the close packed directions on close packed planes are the slip directions, with the corresponding planes being the slip planes as shown in Fig. 1.5(b). A combination of slip plane and a slip direction is called a slip system. There are 12 such slip systems in fcc metals, resulting from 4 slip planes and 3 slip directions on each of those four planes. The slip plane normals belong to the $\{1\ 1\ 1\}$ family, and the slip direction belong to the $\langle 1\ 1\ 0 \rangle$ family.

The slipping action on slip systems manifests as a strain on the overall material geometry. In general applied plastic strains are accommodated by the material through combination of slipping action on multiple systems. In particular, any arbitrary strain can be achieved by a combination

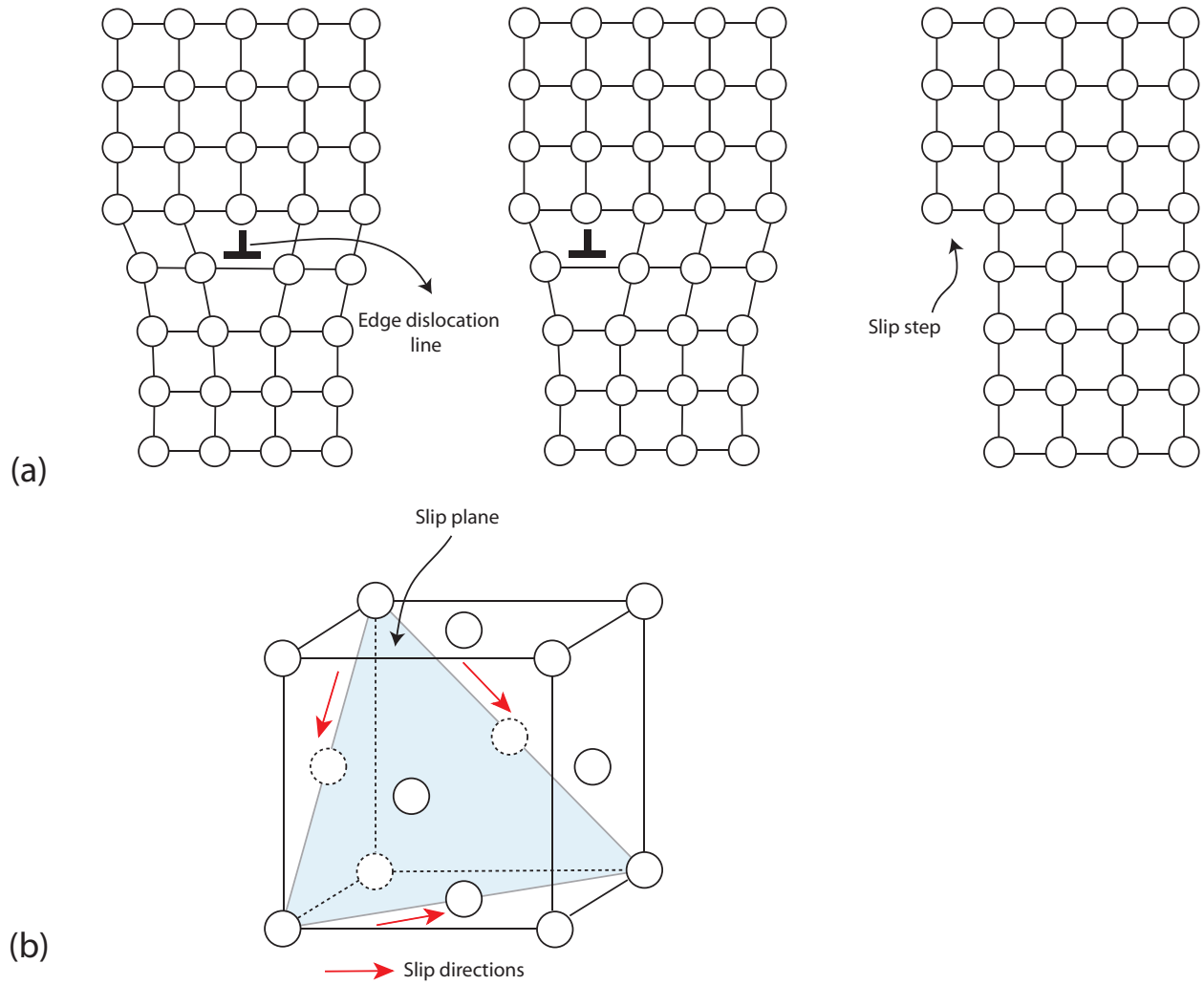


Figure 1.5: (a) Edge dislocation in a lattice and its motion, (b) Face centered cubic unit cell.

of slip on five independent slip systems [39]¹.

The arrangement of slip systems determined by the crystallographic structure is the cause of anisotropy during plastic deformation. Depending on the orientation of the crystal, the amount of work required in deforming fcc crystals can vary significantly.

¹A set of slip systems is said to be dependent if a non trivial combination of slips on those systems can result in zero strain.

Table 1.1: Experimental studies on single-crystal machining from the literature, and associated machining parameters.

	Material	Rake Angle	Feed (μm)	Speed (mm/s)
Clarebrough and Ogilvie (1950) [27]	Pb	60°	25	-
Black [29]	Cu, Al	-	0.0025 -2	1
Ramalingam and Hazra (1973) [17]	Al	40°	127	0.27
Williams and Gane (1977) [35]	Cu	40°	1-100	0.1-1
Ueda and Iwata (1980) [30]	β -brass	$0^\circ, 20^\circ$	0.1-200	0.0025
Williams and Horne (1982) [21]	Cu	40°	100	20
Cohen (1982) [19]	Cu, Al	$50^\circ-0^\circ$	114.3	0.44
Sato <i>et al.</i> (1979-83) [23, 31, 34]	Al	35°	100	1.66
Sato <i>et al.</i> (1991) [24]	Al	3°	0.5-3	16.66
Moriwaki <i>et al.</i> (1993) [22]	Cu	$0, 5^\circ$	0.01-3	8833.33
Yuan <i>et al.</i> (1994) [25]	Cu, Al	0°	1-10	0.16-0.83
To <i>et al.</i> (1997) [20]	Al	0°	1-10	0.16-0.83
Zhou and Ngoi (2001) [40]	Al, Cu	0°	5-10	1300
Lawson <i>et al.</i> (2007) [26]	Al	0°	5-20	5-15

1.2 Literature Review

Researchers have conducted both experimental and theoretical studies on the effect of crystallographic structure on machining response. A brief overview of these studies (with focus on face centered cubic (fcc) materials) is presented in this section.

A number of experimental studies have confirmed that machining response, including machining forces [17–26], chip lamellae [26–30], dynamic shear stress [17, 19–21], and surface roughness [20, 22, 31] depend on the crystallographic orientation in fcc metals. Some investigations also considered the effect of crystallographic anisotropy on the built-up edge (BUE) [27] and material side-flow [31]. Researchers have conducted both plunge-turning [19, 20, 25] and planing experiments [17, 21–24, 26–29, 31] on single-crystal metals. Some of the experimentation was conducted inside a scanning electron microscope (SEM), allowing visual observation of chip formation [19, 30]. Single-crystal fcc materials, mainly aluminum [17, 19–21, 23, 24, 26, 31], and copper [19, 21, 22], have been tested in these studies. The experimental conditions vary significantly across studies, hence a lookup table (see Table. 1.1) containing the conditions for each study is provided for clarity.

Early studies on machining single crystals were aimed at observing the lamellae structure of the chips formed during machining. The first known study was published in 1950 by Clarebrough and Ogilvie [27] who microtomed large crystals of lead, and observed a strong correlation between the crystallographic orientation and lamellae spacing. Subsequent studies of J.T. Black and von Turkovich shed light on various aspects of micro-scale chip formation in single-crystal cutting

[28,29,32,33]. They performed a quantitative study of chip formation mechanisms in single-crystal copper and aluminum via an ultra-microtomy process. Scanning Electron Microscopy (SEM) was used for the first time to examine chip morphology. The lamellae thickness was seen to be affected by the crystallographic orientation and uncut chip thickness (below $2\ \mu m$) [32,33].

In the subsequent years, researchers attempting to establish dynamic shear stress (DSS)² as a fundamental material property, machined coarse grained aluminum crystals [17]. Although the machining forces were seen to vary with the crystal orientation, the DSS was found to be invariant with respect to orientation [17]. However, it must be noted that in *in-situ* (inside an SEM) plunge-turning experiments conducted later, the DSS was found to vary with crystallographic orientation on single-crystal aluminum and copper [19]. In another study on copper, in addition to the orientation of the cutting plane, the cutting direction was also observed to affect DSS [21].

Of all the machining responses, the behavior of machining forces (and therefore the specific energies) while cutting single-crystal materials at different orientations has been studied in greater detail by various researchers [19,21–24,26,31,34,35].

A majority of the researchers [21–24,26,31,34,35] used the planing configuration, in which the tool cuts along a particular crystal direction for a fixed length of the workpiece (see Fig. 1.6(a)). The planing data on aluminum consists primarily of cutting forces on $(1\ 1\ 1)$ [21,24,31], $(1\ 1\ 0)$ [21,24,34] and $(0\ 0\ 1)$ [24,34] planes ((uvw) in Fig. 1.6(a)). Planing force data was also collected for cutting various directions about $[0\ 0\ 1]$ [26] and $[1\ 1\ 2]$ [31] zone axes on aluminum single crystals (i.e., the zone axis directions coincide with $[abc]$ in Fig. 1.6(a)). The planing forces on copper have been measured while cutting on $(1\ 1\ 0)$ and $(1\ 1\ 1)$ planes [21], and about $[1\ -1\ 0]$ zone axis [22,35]. The results from the planing studies showed that the anisotropy of fcc crystals strongly affects the machining forces, inducing up to 312% variation in machining forces at different crystallographic orientations for a given zone axis [26]. In addition to constant (stable) forces [17,21–24,26], monotonically-increasing [23], bi-stable [21,26] and periodically-varying [26,30] force signatures have been observed for different cutting parameters and crystallographic orientations during planing experiments. Abrupt, short-term reduction in forces was also observed in some studies [23].

While planing experiments provide detailed data in terms of cutting forces, only one crystal orientation can be machined at a time. As an alternative to the planing configuration, the plunge-turning configuration shown in Fig. 1.6(b) has been used in [19,20,25]. This configuration provides near-continuous data for the entire range of cutting directions for a given zone axis. These turning

²Dynamic shear stress is the ratio of shear force to shear plane area [16].

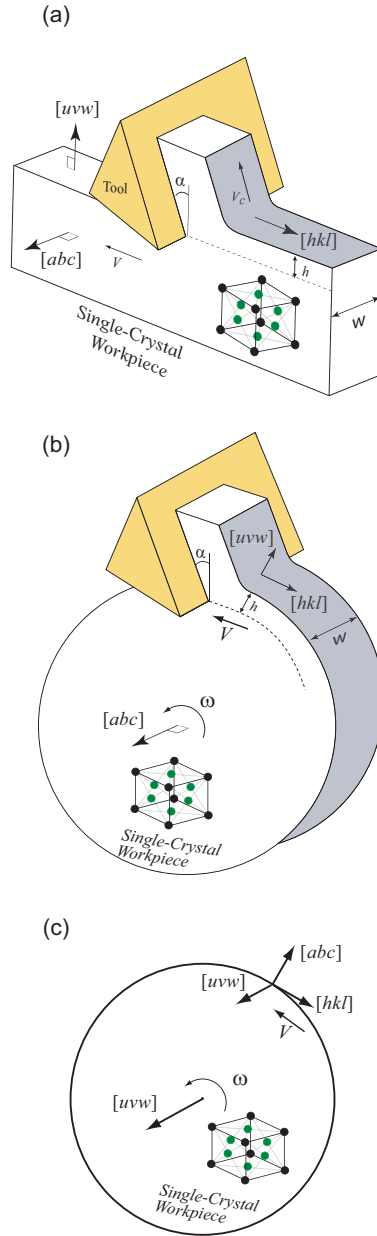


Figure 1.6: (a) Planing configuration, (b) Plunge-turning configuration, and (c) In-plane machining

experiments can be further divided into two types. While Fig. 1.6(b) shows the case where the zone axis $[abc]$ serves as axis of rotation, Fig. 1.6(c) has the cutting plane normal as axis of rotation. Henceforth, the case shown in Fig. 1.6(c) will be referred to as in-plane machining for clarity.

In the plunge turning experiments of Cohen [19] cutting forces were collected about the $[0\ 0\ 1]$ zone axis ($[abc]$ in Fig. 1.6(b)) while cutting both aluminum and copper single-crystals. The force measurements from these experiments showed a repeatable four-fold symmetry expected from the crystallographic symmetry of $[0\ 0\ 1]$ zone axis. While the $[1\ 0\ 0]$ cutting direction produced the minimum force, the maximum force was consistently observed to occur at an offset of 15-20 degrees from $[1\ 1\ 0]$ cutting direction.

The in-plane machining results [20,25] consist of machining force variation with cutting directions about $(1\ 1\ 0)$ and $(1\ 1\ 1)$ cutting plane normals. The experimental force variation with cutting directions on $(1\ 1\ 0)$ plane were found to be larger than those on $(1\ 1\ 1)$ cutting plane due to the increased crystallographic symmetry on $(1\ 1\ 1)$ plane as compared to $(1\ 1\ 0)$ plane.

Despite the above described studies, the available force data is scattered sparsely over the possible cutting conditions, posing a difficulty for validating the developed machining models or gaining a thorough understanding on the effects of crystallographic anisotropy during machining. Although both planing and plunge-turning studies suggest a strong effect of crystallographic anisotropy on machining forces, the available data is insufficient to elaborate on the effects of rake angle, cutting velocity and uncut chip thickness while machining single crystal fcc metals.

Apart from forces another important machining response is the roughness of the machined surface. Experimental studies have found a correlation between different crystallographic orientations and resulting surface roughness [20]. The roughness variation results showed expected crystallographic symmetries in the in-plane machining experiments on copper [20]. In a contrasting result, Moriwaki observed that for uncut chip thicknesses below $0.1\ \mu\text{m}$ when micromachining already-machined surfaces the surface roughness (and machining forces) were not affected by the crystallographic orientation [22]. This was explained by considering the significant sub-surface damage (dislocations) left from previous cutting passes.

While the relatively large body of experimental evidence suggests a strong dependence of machining response parameters (lamellae, DSS, forces, and surface quality) on crystallographic orientation, relatively few attempts have been made to incorporate explicitly the effects of crystallographic anisotropy into machining models [34,36–38]. Modeling the effects of anisotropy requires incorporating the underlying physical phenomenon causing the anisotropy. Additional complications in

machining modeling arise from the lack of knowledge of the actual amount of deformation (often characterized by the shear angle). As a consequence, strategies for incorporating the effects of anisotropy must at first include the determination of shear angle.

Researchers have considered a few different approaches for incorporating the anisotropy into machining models. An early work by Sato *et al.* [34] used the Schmid factor to obtain the active slip systems during machining. The amount of slip on each slip system was assumed to be proportional to the Schmid factor of that slip system. The value of shear angle was then calculated from the vector sum of slip directions on active slip systems.

While the aforementioned approach provides some physical basis, the actual function of Schmid factor is only to predict one active slip system [39]. Hence, Schmid factor-based approaches are more relevant while discussing deformation caused solely by single slip, unlike deformations during machining. To obtain the shear deformation during machining on any arbitrary orientation requires simultaneous activation of five or more independent slip systems. Recognizing this fact, later attempts by researchers incorporated Taylor-factor [39] based models, which are more relevant for multi-slip scenarios.

In a more recent effort, Lee *et al.* [37, 38] used a modified form of the Taylor factor, referred to as the effective Taylor factor, to predict the shear angle in single-crystal cutting. For each crystallographic orientation, the Taylor factor was calculated for all possible shear angles. The effective Taylor factor was then obtained by dividing the Taylor factor with cosine of two times the difference between the candidate shear angle and 45 degrees. Essentially, the effective Taylor factor was used to incorporate the geometrical aspect of variation of strain with shear angle by “penalizing” those shear angle candidates away from the geometrically optimal 45 degrees. This form of effective Taylor factor is only applicable for zero rake angle case, since 45 degrees is not geometrically optimal for non-zero rake angles. While the goal was to choose the shear angle from the orientation that provided the minimum effective Taylor factor, this approach did not yield a unique solution in most cases. A texture softening factor was subsequently used to uniquely predict the shear angle as the angle that results in the minimum texture softening factor. This work was then extended to predict the variation in cutting forces with crystallographic orientation using Merchant’s model.

While the Taylor-factor based models significantly improve the prediction capability as compared to Schmid-factor based models, they do not incorporate the kinematic aspects (rake angle, strain variation with shear angle) and friction (on the rake face) while arriving at shear angle solutions. In determining the shear angles, all of the aforementioned models used only crystal plasticity models,

while the mechanics of material removal was considered after the determination of shear angle. Therefore, the shear angles and shear forces were insensitive to the changes in friction on the rake face.

1.3 Research Objectives

The literature review suggests a critical need for physically realistic force models for micromachining operations. The models need to simultaneously incorporate both the effects of crystallographic anisotropy and the kinematics of the machining process. Furthermore, a careful observation of the available experimental results also reveals a necessity for experimental data on the effects of anisotropy covering a broad range of machining conditions.

The overarching goal of this thesis is to understand and model the effects of crystallography during the micromachining process. We will address this goal through the following specific objectives:

- To develop physically realistic machining force models incorporating anisotropy.
- To perform experimental analysis and understand the effects of crystallography on machining of coarse grained polycrystal and single-crystals.

1.4 Research Contributions

The fundamental contributions of this thesis research are focused on modeling and experimental investigations on single-crystal and coarse-grained materials. Specific contributions include;

1. Development of a simplified machining model incorporating crystallographic anisotropy by combining Bishop and Hill's plasticity model with Merchant's machining force model
2. Development of a comprehensive rate-sensitive plasticity-based machining force (RSPM) model to include the effects of lattice rotation and strain hardening.
3. Development of experimental infrastructure, including a precision planing and a precision turning apparatus for performing micro planing and micro plunge turning operations.
4. An experimental understanding on the effects of crystallography when micro-machining single-crystal and coarse-grained materials.

Chapter 2

A Simplified Model for Orthogonal Machining of FCC Single-crystal Materials

This chapter presents a simplified crystal-plasticity based machining force model and its analysis. First, the model, which combines the Bishop and Hill's plasticity theory and Merchant's machining model, is described in detail. For a given crystallographic orientation (workpiece zone axis and cutting plane), the model considers the minimization of the total power, including the shearing and rake-face friction power, to determine the shear angle and specific energies. Next, the results from the model are validated against experimental data from the literature for machining on single-crystal aluminum and copper, indicating the model's capability to capture the effects of crystallographic anisotropy. The model is then used to investigate the effects of friction, rake angle, and crystallographic orientation on specific energies and shear angles. A set of metrics, including the mean value, the deviation from the mean, and the phase shift of the specific energies, are used to facilitate evaluation of the results over a wide range of parameters. Finally, a simplification to the model, based on the use of Merchant's shear angle, is proposed. The validity of the simplification is mathematically proven, and the simplified model is shown to capture important trends regarding crystallographic anisotropy.

2.1 Model Description

In this section, the crystal plasticity based model for orthogonal cutting of fcc metals is described. The model requires the calculation of the plastic power (for shearing) and the friction power. In determining the friction power, the shear and friction forces, as well as the shear strain, are related to the shear angle through Merchant's model [16]. Subsequently, a procedure is used to determine the shear angle that will result in the minimum machining power (i.e., the sum of shearing and friction powers). Once the shear angle is determined, shear strain, and cutting and thrust specific energies, can be calculated. The present model assumes that the effects of lattice rotation during the calculation of plastic power is negligible. A constant coefficient of friction on the rake face is considered. Furthermore, the shear is assumed to occur along a thin shear plane. In contrast to earlier models (e.g., [34]), an *a-priori* selection of slip systems involved in deformation is not required in the proposed model. Rather, the model provides a superset of potentially active slip systems based on the chosen yield vertex within the Bishop and Hill's theory.

2.1.1 Calculation of Plastic Power

Calculation of plastic power necessitates the knowledge of work done in plastic deformation along with the volumetric flow rate. In the presented model, Bishop and Hill's theory [41] is used to obtain the plastic work. The incremental plastic work, dW_p , can be expressed as

$$dW_p = -B\epsilon_{11} + A\epsilon_{22} + 2F\epsilon_{23} + 2G\epsilon_{13} + 2H\epsilon_{12}. \quad (2.1)$$

where the coefficients A , B , F , G and H depend on the critical resolved shear stress (CRSS) τ_c as described in [39], and ϵ_{ij} are the elements of the strain tensor in the crystallographic coordinate system. Using Eq. (2.1), dW_p can be calculated for each of the 56 possible yield vertices that exists for an fcc metal, assuming CRSS is same for all the slip systems. The maximum value of work, out of the 56 yield vertices, is then considered as the work of plastic deformation¹.

To calculate the strain tensor for the cutting process, the geometry of orthogonal cutting process given in Fig. 2.1(a) is considered, where ϕ is the shear angle, h is the uncut chip thickness, and α is the rake angle. For a shear of $d\gamma$ along the shear plane, with the plane-strain condition, the

¹Equivalently, the work can be obtained by minimizing the plastic work over 384 sets of independent slip systems in Taylor's model [43, 44].

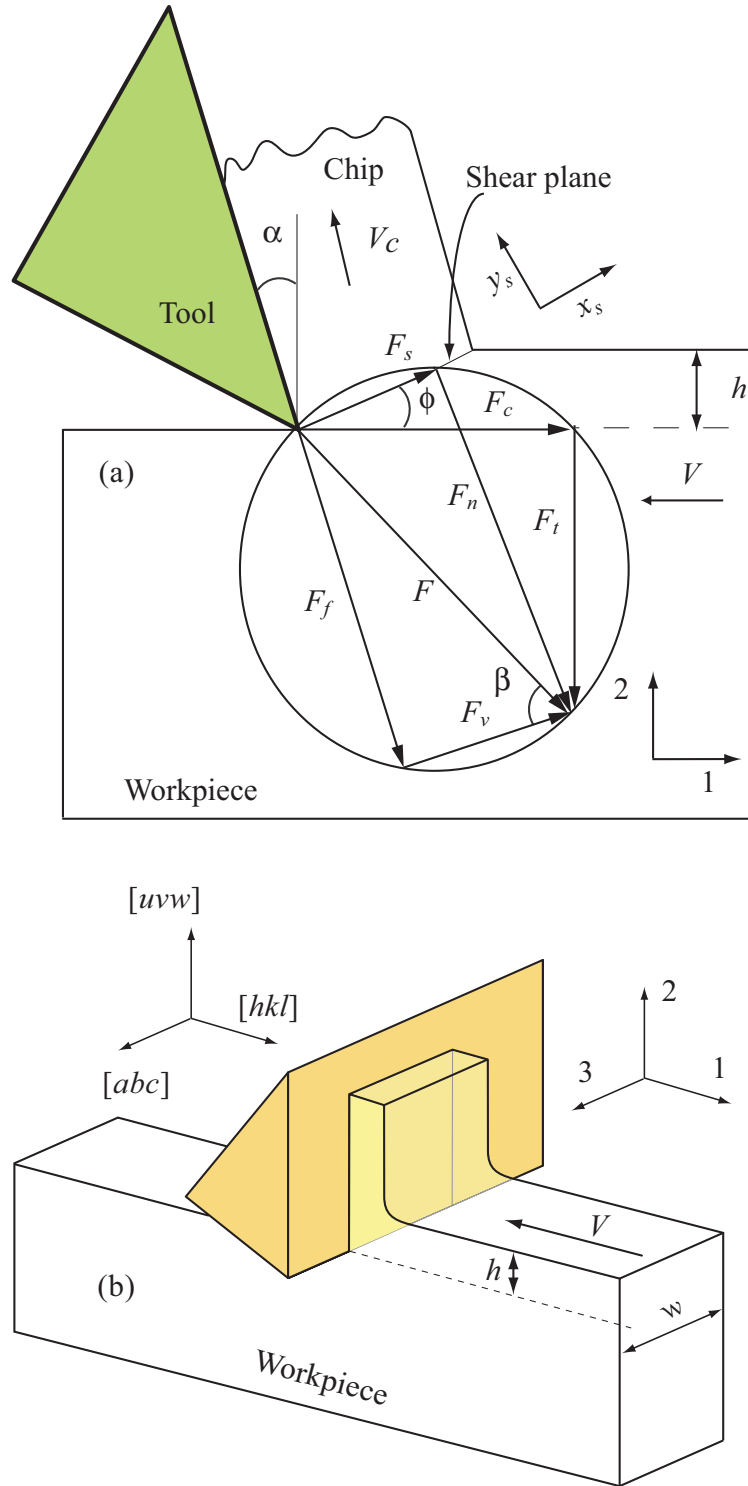


Figure 2.1: (a) A depiction of the orthogonal cutting process with the Merchant's cutting force diagram, and (b) the coordinate system used for model derivation.

displacement gradient in the shear plane coordinates (x_s, y_s) is given by

$$E_s = d\gamma \begin{bmatrix} 0 & 1 & 0 \\ 0 & 0 & 0 \\ 0 & 0 & 0 \end{bmatrix}. \quad (2.2)$$

The symmetric part of the displacement gradient gives the strain tensor ϵ_s as

$$\epsilon_s = \frac{E_s + E_s^T}{2} = \frac{d\gamma}{2} \begin{bmatrix} 0 & 1 & 0 \\ 1 & 0 & 0 \\ 0 & 0 & 0 \end{bmatrix}. \quad (2.3)$$

Using a coordinate transformation matrix, the strain tensor ϵ_w in the workpiece coordinate system (1-2-3) shown in Fig. 2.1(b) can be written as

$$\epsilon_w = T_\phi \epsilon_s T_\phi^T = \frac{d\gamma}{2} \begin{bmatrix} -\sin(2\phi) & \cos(2\phi) & 0 \\ \cos(2\phi) & \sin(2\phi) & 0 \\ 0 & 0 & 0 \end{bmatrix}, \quad (2.4)$$

where the coordinate transformation matrix T_ϕ is given as

$$T_\phi = \begin{bmatrix} \cos(\phi) & -\sin(\phi) & 0 \\ \sin(\phi) & \cos(\phi) & 0 \\ 0 & 0 & 1 \end{bmatrix}. \quad (2.5)$$

Since Eq. (2.1) requires the strain components to be expressed in the crystal coordinate system, a coordinate transformation can be used to obtain the strain tensor ϵ in the crystal coordinates as

$$\epsilon = P \epsilon_w P^T, \quad (2.6)$$

where coordinate transformation matrix P is determined from the orientation of current coordinate system with respect to the crystal coordinates. Based on the orthonormal Miller indices associated with the directions 1-2-3 given in Fig. 2.1(b), P can be written as

$$P = \begin{bmatrix} h & u & a \\ k & v & b \\ l & w & c \end{bmatrix}. \quad (2.7)$$

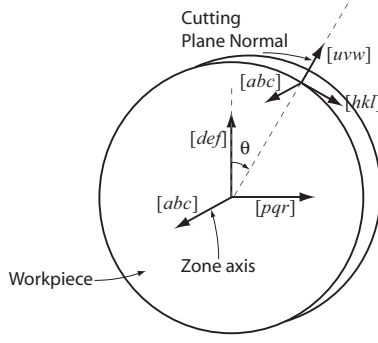


Figure 2.2: Definition of the orientation angle for fixed zone axis. A disk-type workpiece is considered in plunge-turning configuration.

One way to describe the cutting orientation (i.e., the cutting-plane normal) is to define an angle θ from a reference axis perpendicular to the zone axis, as illustrated in Fig. 2.2. Based on this definition, the P matrix can be expressed as

$$P = RT_{\theta}, \quad (2.8)$$

where

$$R = \begin{bmatrix} p & d & a \\ q & e & b \\ r & f & c \end{bmatrix}, \quad T_{\theta} = \begin{bmatrix} \cos(\theta) & \sin(\theta) & 0 \\ -\sin(\theta) & \cos(\theta) & 0 \\ 0 & 0 & 1 \end{bmatrix}. \quad (2.9)$$

Combining Eqs. (2.3)-(2.9), an expression for ϵ can be obtained as

$$\epsilon = RT\epsilon_s T^T R^T, \quad (2.10)$$

where T is given by

$$T = T_{\theta}T_{\phi} = \begin{bmatrix} \cos(\phi - \theta) & -\sin(\phi - \theta) & 0 \\ \sin(\phi - \theta) & \cos(\phi - \theta) & 0 \\ 0 & 0 & 1 \end{bmatrix}. \quad (2.11)$$

The incremental work for shearing the material along the shear plane can now be calculated from Eq. (2.1) using the elements of the ϵ matrix (ϵ_{ij} 's) obtained from Eq. (2.6). The total work of plastic deformation, W_p , is obtained by summing the incremental work until the prescribed

engineering shear strain γ is reached. Under the assumption of no lattice-reorientation during plastic deformation, the total work for any given zone axis and angle θ in terms of prescribed engineering shear strain simplifies to

$$W_p = \int dW_p = \int_0^\gamma g(\phi - \theta) d\gamma = g(\phi - \theta) \gamma. \quad (2.12)$$

Here, $g(\phi - \theta)$ represents a function that is obtained by maximizing (over the 56 possible vertices) the work expression in Eq. (2.1) after substituting the required elements of the ϵ tensor from Eq. (2.10). The shearing power (i.e., the power spent in plastic deformation), \dot{W}_p , can now be obtained from the product of volumetric flow rate of the material and the plastic work as

$$\dot{W}_p = (hwV) W_p, \quad (2.13)$$

where w is the width of cut and V is the cutting velocity.

2.2 Calculation of Forces and Power

Since the shear angle solution will be determined through the minimization of *total* power, it is necessary to obtain the power spent in overcoming friction on the rake face. The friction power can be obtained if the friction force and chip velocities are known. Where as the chip velocity can be determined from the geometry, the determination of the friction force requires the knowledge of shear force and coefficient of friction on the rake face.

The shear force, F_s , in Merchant's model can be calculated from shearing power using

$$F_s = \frac{\dot{W}_p}{V_s}, \quad (2.14)$$

where the shear velocity V_s can be related to the cutting velocity V as

$$V_s = V \frac{\cos(\alpha)}{\cos(\phi - \alpha)}. \quad (2.15)$$

The friction force, F_f , can be given in terms of the tangential force F_c and thrust force F_t as

$$F_f = F_c \sin(\alpha) + F_t \cos(\alpha) \quad (2.16)$$

where,

$$F_c = \frac{F_s \cos(\beta - \alpha)}{\cos(\phi + \beta - \alpha)}, \quad F_t = \frac{F_s \sin(\beta - \alpha)}{\cos(\phi + \beta - \alpha)},$$

and β is the friction angle, which can be related to the coefficient of friction μ as

$$\tan \beta = \mu. \quad (2.17)$$

To calculate the friction power \dot{W}_f , the friction force is multiplied with the chip velocity V_c as

$$\dot{W}_f = F_f V_c, \quad (2.18)$$

where,

$$V_c = V \frac{\sin(\phi)}{\cos(\phi - \alpha)}. \quad (2.19)$$

The total power, P_t , can now be calculated by summing the shear power and friction power as

$$P_t = \dot{W}_f + \dot{W}_p = g(\phi - \theta) \frac{(hwV) \cos(\beta - \alpha)}{\sin(\phi) \cos(\phi + \beta - \alpha)}, \quad (2.20)$$

where

$$\gamma = \frac{\cos(\alpha)}{\sin(\phi) \cos(\phi - \alpha)} \quad (2.21)$$

is used to express the engineering shear strain in terms of shear and rake angles.

2.2.1 Solution Procedure

The first step of the modeling procedure is the determination of shear angle within the physically allowable ranges. The force relations in Merchant's machining model indicates that shear angles larger than $(90 - (\beta - \alpha))$ would reverse the direction of shear force along the shear plane. Furthermore shear angles are required to be positive. Therefore, the physically allowable range of shear angles are within $(0, (90 - (\beta - \alpha)))$.

The crystallographic strain tensor is then calculated from Eq. (2.6) for the specified crystallographic orientations of the cutting plane normal and cutting direction. These strain values are used to determine the plastic work using Eqs. (2.1) and (3.10). The product of volumetric flow rate of

the material and the calculated plastic work results in the shearing power following Eq. (3.6).

Next, for the given friction angle and cutting velocity, the shearing force, shearing velocity, and the friction force are determined using Eqs. (2.14), (2.15) and (2.16), respectively. Summing the friction power obtained from Eq. (3.2) with the shearing power yields the total power for the cutting process according to Eq. (3.1).

For a given cutting orientation, total power is calculated for every shear angle candidate (with a specific increment) within the allowable range. The shear angle candidate resulting in the minimum power is then selected as the shear angle for the specified conditions. Therefore, the shear angle and the cutting forces are uniquely determined for given crystallographic orientations of the cutting plane normal and cutting direction.

2.3 Model Validation

In this section, we provide experimental validation using data from the literature for both single-crystal aluminum and single-crystal copper (both fcc metals). In addition to varying cutting direction for constant zone axis, comparisons with data are also provided for varying zone axis for constant cutting plane.

2.3.1 Validation for Fixed Zone Axis

The first set of experimental validation includes varying cutting direction (with respect the crystal axes) for $[0\ 0\ 1]$ zone axis (see Fig. 2.2). The experimental data presented in [17, 19] from *in-situ* diamond-turning experiments inside an SEM on single-crystal aluminum and copper are used for the validation study. The experiments are conducted in a plunge-turning configuration, where a disk of single-crystal aluminum or copper is cut by feeding the cutting tool along the disk diameter as the disk is rotated. For aluminum, Cohen [19] used the rake angles of 40 and 50 degrees. The cutting velocity and uncut chip thickness were set to 0.44 mm/s and 0.11 mm, respectively, for each rake angle. The width of workpieces varied between 1.27 mm to 1.65 mm. For the copper single crystals, the rake angles of 20 and 40 degrees were used, and the cutting velocity and uncut chip thickness were set to 0.55 mm/s and 0.11 mm, respectively. The width of workpieces varied between 2.03 mm to 2.67 mm. The zone axis of the machined single crystals for both aluminum and copper was parallel to $[0\ 0\ 1]$ direction. To evaluate the proposed model, the shear angles and specific cutting energy obtained from the model are compared to Cohen's experiments.

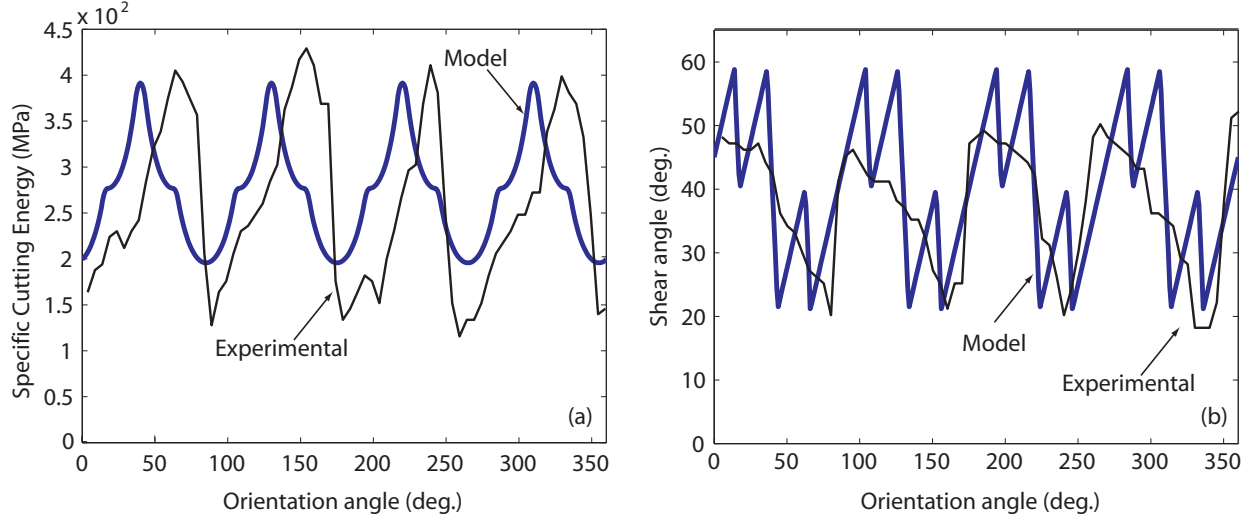


Figure 2.3: The experimental data used for the calibration of the model for aluminum single-crystal machining with fixed zone axis ($[0\ 0\ 1]$); and the model with the calibrated CRSS value of 67 MPa: (a) Specific cutting energies, and (b) Shear angles.

The model requires the effective CRSS, which depends on the deformation history and strain rate. To determine the effective CRSS value for aluminum through calibration, the mean horizontal force for orientations about $[0\ 0\ 1]$ direction for the 40 degree rake angle case was used. It is critical to note that the model calibration requires only one value, the mean specific cutting energy. For this reason, only a few extremum points are sufficient for model calibration. Since the horizontal force, and subsequently the specific cutting energy, depend linearly on the CRSS, this calibration does not change the calculated variations of shear angle and specific energies with crystallographic orientations, but only scales the magnitudes of specific energies. The calibration yielded a CRSS value of 67 MPa considering an average workpiece width of 1.46 mm and a friction angle of 50 degrees (as given in [19]). This relatively higher value of CRSS is expected due to the large strain and high strain rates, and associated increase in hardening and strain-rate effects, experienced during machining.

Figure 2.3(a) shows the calibration data along with the modeling result obtained using the CRSS value of 67 MPa. In this figure, the orientation angles are measured between the cutting plane normal and $[0\ 1\ 0]$ direction about zone axis ($[0\ 0\ 1]$) as shown in Fig. 2.2. The direction of cutting velocity (assigned to the workpiece) is given by the cross product between zone axis and cutting plane normal. It is seen that the model captures the general trend of variation in forces with crystallographic orientation. A slight phase shift is also observed between the model and experiments. As pointed out by Cohen, however, this could be the result of complexity of chip

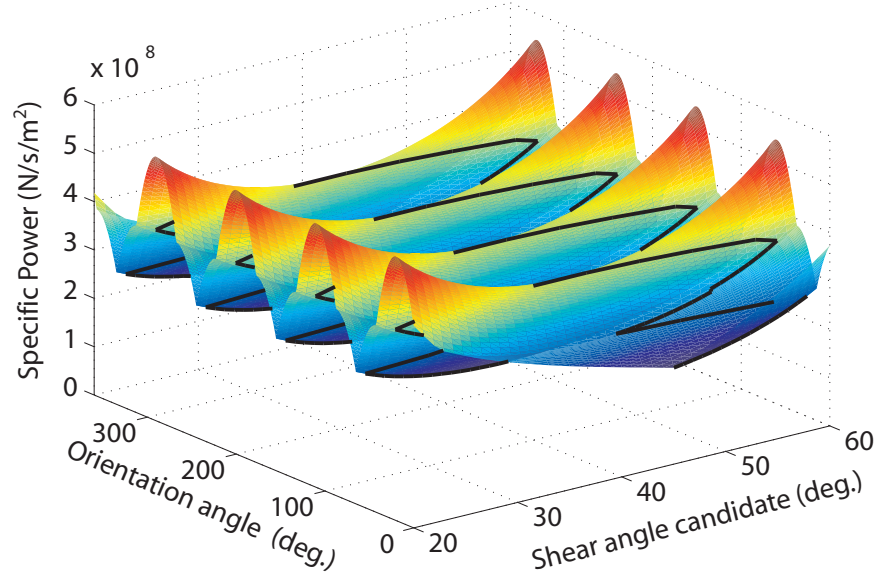


Figure 2.4: The variation of calculated specific total power with shear angle candidates and orientation angles. The solid line indicates the minimum specific power.

formation due to continuously varying crystallographic orientation experienced during the turning processes.

Figure 2.3(b) compares the calculated shear angle with the experimental results. Although the cyclic variation of the shear angles was captured, the specific trend of shear angles show some differences from that seen in the experiments. Those differences may be explained considering Fig. 2.4, which shows the values of total specific power calculated for all the orientations at different shear angle candidates. At a fixed orientation angle, the surface shows how the specific total power varies with shear angle candidates. The shear angle candidate that provides the minimum power is selected as the shear angle solution. In Fig. 2.4, these minimum power values obtained at every orientation angle are joined by a solid line. The predicted shear angle curve seen in Fig. 2.3(b) is the projection of this line on the shear angle candidate - orientation angle plane. A closer examination of Fig. 2.4 indicates that the total power changes very slowly with the shear angle around the minimum shear angle. This indicates that the total power for a relatively large range of shear angles are approximately the same. This phenomenon causes a relatively large deviation on selected shear angles. However, since the forces depend on the total power, and since the total power does not vary appreciably, the forces can still be identified accurately.

The calculated DSS using the calibrated CRSS was found to vary between 82 MPa and 164 MPa for orientations about $[0\ 0\ 1]$ direction. The calculated range closely matches the range (105-166

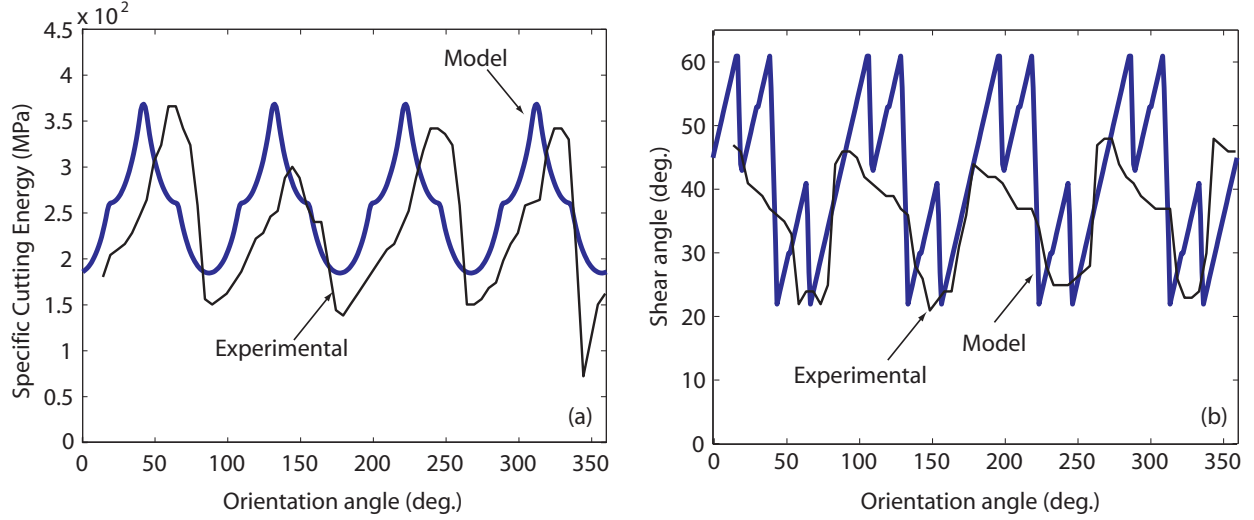


Figure 2.5: Comparison of the model predictions and experimental data for aluminum single-crystal machining with fixed zone axis of $[0\ 0\ 1]$: (a) Specific cutting energies and (b) Shear angles.

MPa) reported in literature [17] for single crystal aluminum while cutting under similar conditions (40 degree rake angle).

The validation for aluminum is done by comparing the calculated value of cutting specific energy and shear angles with the experimental value for a separate set of data (from calibration). For the validation case, a 50 degree rake angle and a 56.5 degree friction angle are used Fig. 2.5. It can be seen that the variation in specific energies arising from the crystallographic anisotropy (with $\pm 31\%$ variation about the mean), as well as the particular trend of variation (peaks and valleys at certain orientations) is well captured by the model. For the reasons explained above, the shear angles do not show as close of a match as the specific energies.

For copper, the calibration was performed using the case of 20 degree rake angle and 40 degree friction angle about $[0\ 0\ 1]$ zone axis [19]. The calibrated value of the CRSS, considering an average workpiece width of 2.35 mm, is 300 MPa, which is reasonable considering the large strain and high strain rates involved during cutting.

The validation for copper is performed by comparing the predicted values using the calibrated CRSS for the case of 40 degree rake angle and 57 degree friction angle about $[0\ 0\ 1]$ zone axis using the calibrated CRSS value. As shown in Fig. 2.6, similar to that for aluminum, the specific cutting energy matches well with the experimental values. It should be noted that the experimental data shows some anomalous behavior, as noted by Cohen [19], above an orientation angle of 300 degrees; as expected from crystallographic symmetry, the data was supposed to continue the periodic

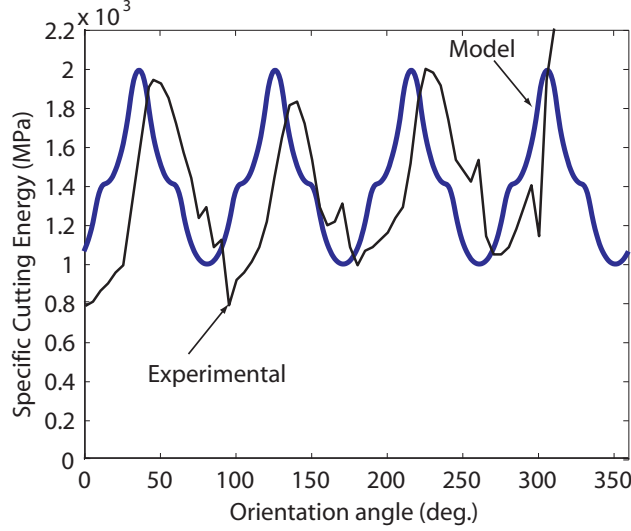


Figure 2.6: Comparison of the predicted and experimentally obtained specific energies for copper single-crystal machining with fixed zone axis of $[0\ 0\ 1]$.

pattern. This portion of the data is disregarded due to experimental error [19]. In general, the variation in specific energies arising from the crystallographic anisotropy and the particular trend of variation is, again, successfully captured by the model.

2.3.2 Validation for Fixed Cutting Plane

The second set of experimental validation includes varying zone axis for fixed value of cutting plane normals (see Fig. 2.7). Zhou and Ngoi [40] presented cutting forces for planing of single-crystal copper, where different cutting directions on the $(1\ 1\ 0)$ and $(1\ 1\ 1)$ cutting planes were considered. Unlike the fixed zone axis, where the observation direction (i.e., the zone axis) is kept the same, in-plane machining keeps the cutting plane normal the same while changing the cutting direction about the normal. The experiments are conducted in a face cutting operation where the depth of cut is given along the plane normal of the rotating single crystal disk.

A comparison between the predicted cutting-force variation with the direction of cut on the $(1\ 1\ 0)$ and $(1\ 1\ 1)$ cutting planes of single-crystal copper with the experimental data is provided in Fig. 2.8. Since the friction coefficient was not specified in [40], only a qualitative comparison can be made, i.e., the variation of forces with crystallographic orientation, rather than the exact force magnitudes, are compared. It should be noted that, irrespective of actual friction coefficient, the predicted trend of variation remains similar. As seen in Fig. 2.8, the model successfully captures the force variation on both planes. The predicted variation on the $(1\ 1\ 0)$ plane is larger than

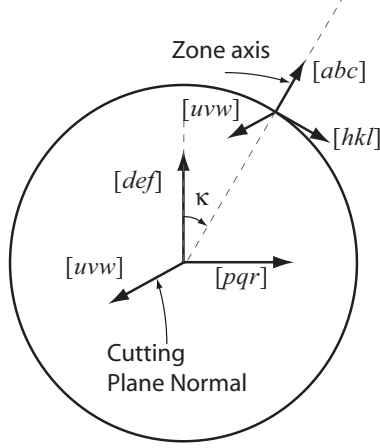


Figure 2.7: Sample, crystal, and cutting orientations for the fixed cutting plane experiments and validation in planing configuration.

the variation on (1 1 1) plane as observed in experiments due to the increased crystallographic symmetry on (1 1 1) plane as compared to (1 1 0) plane.

2.4 Model application

Using the calibrated values of critical resolved shear stress, the model is used to analyze the effects of crystallographic orientation, rake angle and friction angles on specific energies and shear angles for both aluminum and copper. An examination of the model indicates (Eq.3.1) that the specific energies and shear angles depend only on the difference between friction and rake angles. The effect of change in workpiece material is incorporated in the model through change in $(\beta - \alpha)$ and CRSS. Furthermore, since the only effect of CRSS (at a fixed $(\beta - \alpha)$) is to uniformly scale the specific energies, the effect of orientation and $(\beta - \alpha)$ is studied for one fcc material. The behavior for another fcc material can be obtained by scaling the specific energy plots with the ratio of CRSSs of the materials. Hence, the effect of crystallographic orientation and $(\beta - \alpha)$ is studied only for aluminum.

To study the effect of orientation, the variation in specific energies are plotted for orientations about eight different zone axis, namely [0 0 1], [1 1 1], [1 0 1], [1 1 2], [2 1 2], [2 1 3], [2 1 6] and [1 0 2]. As indicated in Fig. 3.17, the zone axes are chosen such that they are uniformly distributed over the basic stereographic triangle. The orientation angles about [0 0 1], [1 1 1], [1 0 1], [1 1 2], [2 1 2], [2 1 3], [2 1 6] and [1 0 2] zone axis were measured clockwise from [0 1 0], [1 1 -2], [0 1 0], [-1 1 0], [-1 0 1], [-1 -1 1], [1 4 -1] and [0 1 0] directions, respectively, according to Fig. 2.2.

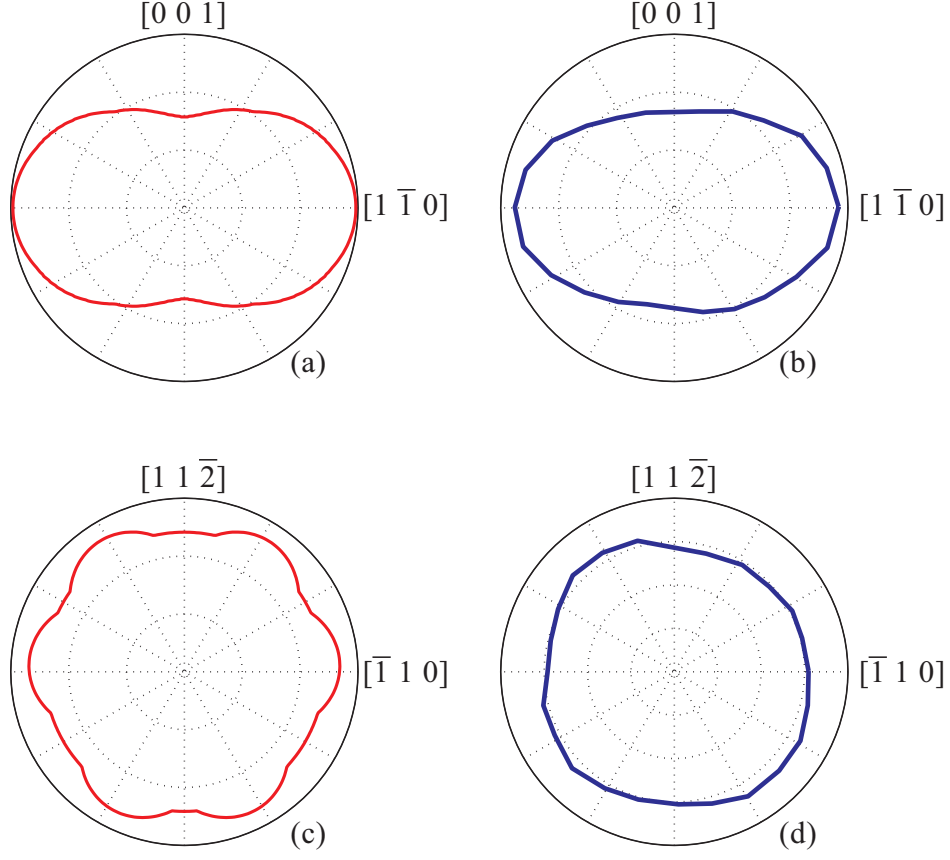


Figure 2.8: (a) Simulated variation in cutting force on (1 1 0) plane, (b) Experimental variation in cutting force on (1 1 0) plane [40], c) Simulated variation in cutting force on (1 1 1) plane and (d) Experimental variation in cutting force on (1 1 1) plane [40].

The specific cutting energies for $(\beta - \alpha)$ of 10 degrees are shown in Fig. 2.10. Since the thrust force, F_t , is equal to $F_c \tan(\beta - \alpha)$, the specific thrust energy plots can be obtained by scaling the specific cutting energy plots by $\tan(\beta - \alpha)$.

For a given zone axis, the overall shapes of the specific energy curves are seen to vary only negligibly with changing $(\beta - \alpha)$. Thus, as seen in Fig. 3.12, the shape of the specific energy curve can be parameterized by using three parameters, including the mean value M , the deviation about the mean (amplitude Ω divided by the mean M), and the phase angle η (the phase lag of the maximum value of specific energy from 0 degrees). This parameterization allows us to represent the variation of $(\beta - \alpha)$ for a given zone axis by presenting the specific energy curve once, and then plotting the change in the three parameters with changing $(\beta - \alpha)$.

The deviation is useful in an operation like milling, where the rotation of the tool causes continuously changing cutting direction about the zone axis (aligned along the rotation axis). The

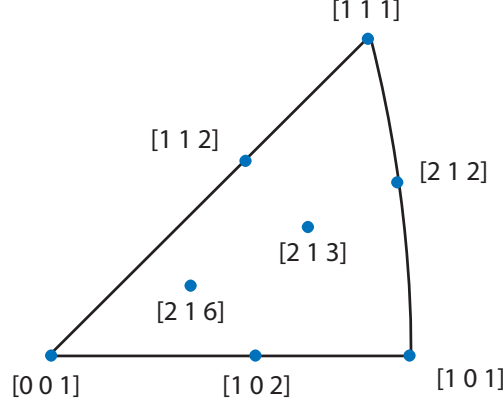


Figure 2.9: The standard stereographic triangle and the zone axes selected for the analysis.

deviation in specific energy can also have a significant effect in determining the quality of machined surface. The mean specific energy, M , provides information on the ease of machinability about a particular zone axis. It should be noted that the phase angle is meaningful only within an orientation, and the phase angles cannot be compared across orientations since they are measured from different directions for each zone axis. The phase angles are provided only to qualitatively observe how the specific energies shift with varying $(\beta - \alpha)$ for different zone axes.

Although most of the zone axes chosen do not have a structural four-fold symmetry, the specific energies and shear angles showed a four-fold symmetry in all cases. This was observed to be the result of sparsity of strain tensor of the form given by ϵ_w in Eq. (2.4). The resulting strain tensor ϵ in crystal coordinates for two cutting plane normals, separated by 90 degrees about any zone axis, were observed to be the negative of each other for any orientation. Furthermore, the symmetries in the Bishop and Hill theory (symmetries of yield vertices) result in same maximum work values irrespective of the sign of the strain tensor. Thus, for the two orientations separated by 90 degrees, the resulting total power are equal for any shear angle candidate. Hence, the chosen shear angle and the corresponding specific energies are also equal, and a four fold symmetry is observed at any zone axis.

Figures 2.12(a) and 2.12(b) show the effect of varying the $(\beta - \alpha)$ on the mean specific cutting energy and mean specific thrust energy, respectively, for various zone axes. Although the mean specific thrust energy plots can be obtained by scaling the mean specific cutting energy plots by $\tan(\beta - \alpha)$, they are provided here for added clarity. Increasing $(\beta - \alpha)$ is seen to increase mean specific energies, indicating, as expected, that increasing rake face friction or reducing the rake angle increases the mean specific energies. Although the mean specific energy was seen to vary

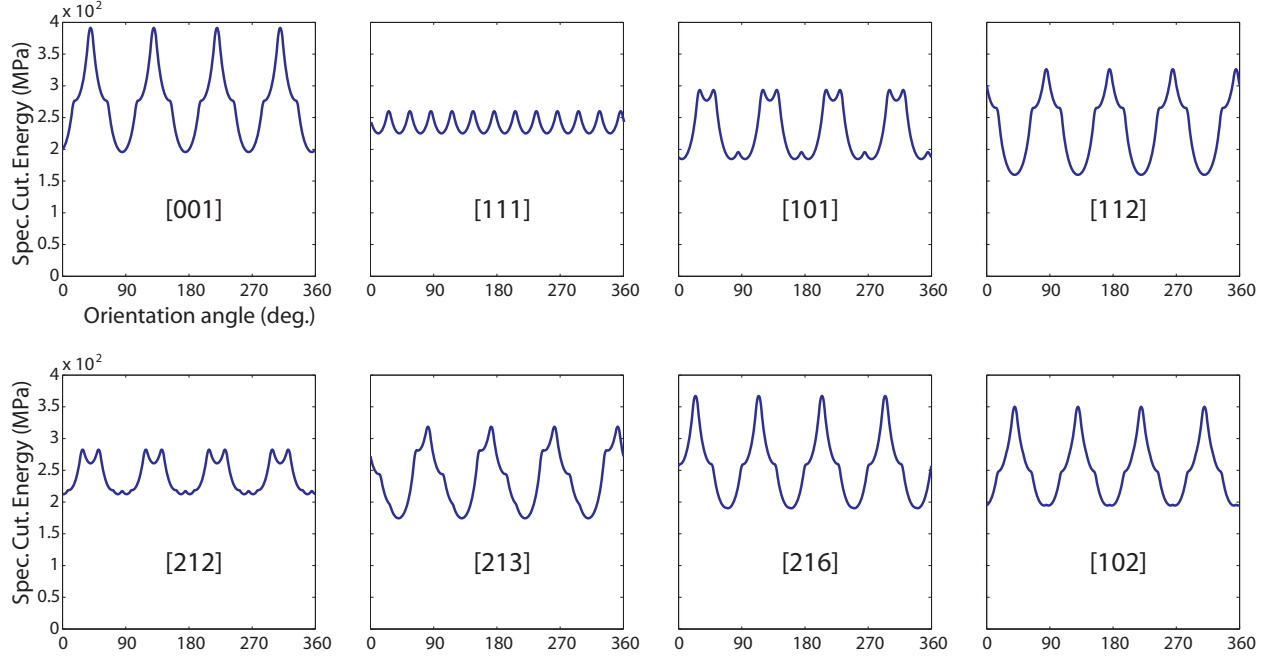


Figure 2.10: The effect of zone axis on specific cutting energy.

with zone axes, this variation was seen to be small relative to the values of mean specific energy. It should be noted that since the specific energy values scale with the CRSS value, the amount of (absolute) variation would be larger for copper. The $[1\ 0\ 1]$ and $[0\ 0\ 1]$ zone axes exhibit the minimum and maximum values of mean specific energy, respectively. This can be explained by the fact that the model yielded a higher (8) number of potential slip systems for $[0\ 0\ 1]$, as opposed to 6 for $[1\ 0\ 1]$. Thus $[1\ 0\ 1]$ required a lower amount of slip to achieve the given deformation, resulting in lower specific energy values.

It is also seen that the specific thrust energy is more sensitive to $(\beta - \alpha)$ than the specific cutting energy, as can be seen by comparing Fig. 2.12(a) and Fig. 2.12(b). This is due to the dependence of specific thrust energy on $\sin(\beta - \alpha)$, as opposed to $\cos(\beta - \alpha)$ in the case of specific cutting energy.

Figure 2.13(a) shows the effect of varying the $(\beta - \alpha)$ on the deviation of specific energy. The deviation values do not vary significantly with $(\beta - \alpha)$, which is in agreement with the earlier assertion that the shape of the specific energy plots do not vary significantly with $(\beta - \alpha)$. This means that, for a given zone axis direction, neither the rake angle nor the rake face friction affect the deviation significantly. The $[0\ 0\ 1]$ and $[1\ 1\ 1]$ zone axes exhibit the maximum and minimum values of deviation, respectively. The deviation in specific energies about the $[1\ 1\ 1]$ zone axis

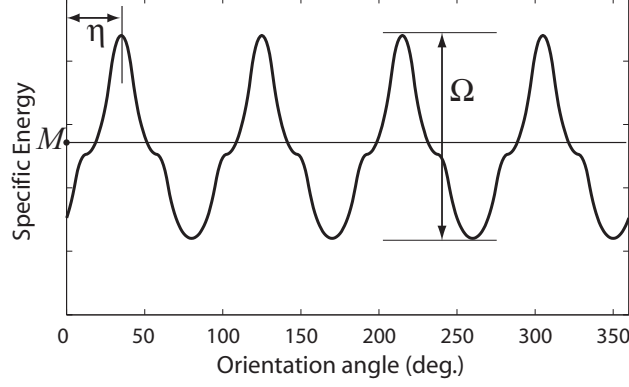


Figure 2.11: The parameters that are defined to describe the specific energy variation with orientation angle for given zone axis. In addition to the shape of the curve, the mean value M , the amplitude Ω , and the phase angle η are defined.

is experimentally observed to be less than that about the $[0\ 0\ 1]$ axis [25]. The model predicts this phenomenon as seen in Fig. 2.13(a), in congruence with the existing literature. The reduced deviation about $[1\ 1\ 1]$ arises from the increased crystallographic symmetry about this zone axis. It should be noted that the deviation is the same for both specific cutting and thrust energies, since both Ω and M for specific thrust and cutting energies are related by $\tan(\beta - \alpha)$.

Figure 2.13(b) shows the effect of varying $(\beta - \alpha)$ on the phase η of specific energy. Similar to the deviation, the phase plots will remain the same for both specific cutting and specific thrust energies. The plots show a shift in position of maximum specific energies with varying $(\beta - \alpha)$. The shift is similar for all the zone axes. The phase angle η cannot be compared across orientations since they are measured from different directions for each zone axis.

The mean values of shear angle about each zone axis are calculated and plotted in Fig. 2.14. It is seen that the variation of mean shear angles between different zone axes are negligible. Furthermore, the mean shear angle value is seen to be approximately equal to

$$\phi_{mean} = \frac{\pi}{4} - \frac{\beta - \alpha}{2}. \quad (2.22)$$

Indeed, this is the shear angle calculated by Merchant through minimization of total power while considering an isotropic material.

An interesting consequence of crystallographic anisotropy and machining geometry is that, for the same zone axis and cutting plane, reversal of cutting direction results in different forces. This is an unexpected result when isotropic, or effectively isotropic, workpiece material is considered;

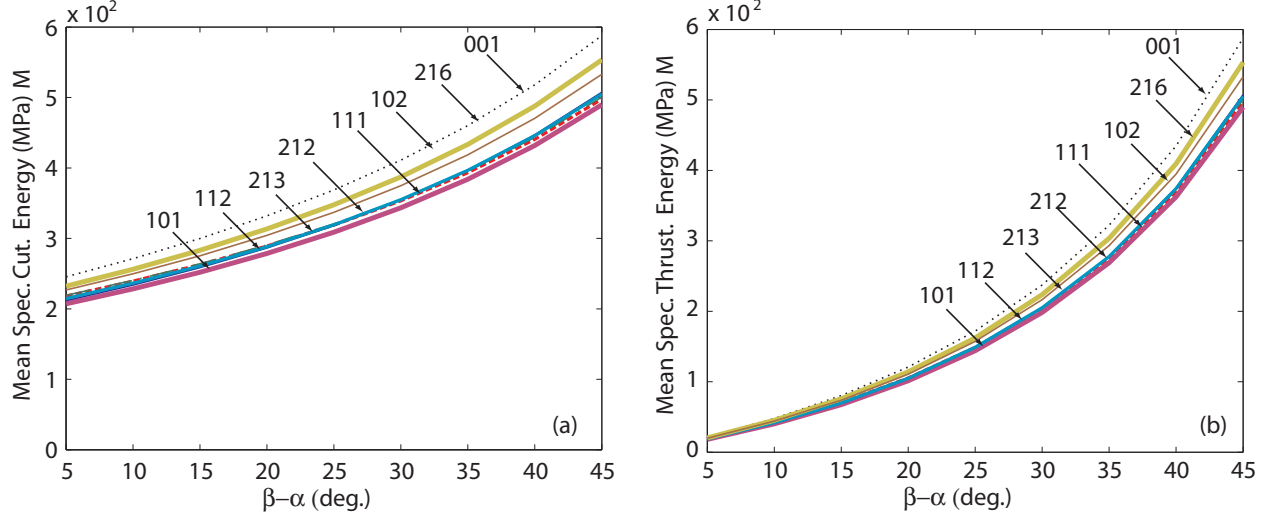


Figure 2.12: The effect of $(\beta - \alpha)$ on (a) mean value of specific cutting energy and (b) mean value of specific thrust energy.

in those cases, when cutting on the same plane and under the same cutting conditions, reversal of the cutting direction would not cause a change in the forces. Indeed, in their experimental study, William and Horne [21] observed that reversing the cutting direction on a given crystallographic plane results in a variation in cutting force. The current framework provides a simplified analysis for understanding the effect of reversal of cutting direction. The effect of reversal of cutting direction can also be shown analytically by considering the modeling framework (i.e., the T matrix in Eq. (2.11) becomes a function of $(\phi + \theta)$ rather than $(\phi - \theta)$ with the reversal of cutting direction, which alters the work expression of Eq. 3.10).

Figure 2.15(a) considers the cutting direction opposite to that shown in Fig. 2.2. The cutting plane is kept the same in both cases. The zone axis is taken such that the cutting direction, cutting plane normal and zone axis form a right-handed coordinate system. It is seen in Fig. 2.15(b) that the reversal of cutting direction induces a shift on the specific energies for $[0\ 0\ 1]$ zone axis. While this seems like a small change at the first look, at some orientation angles, it causes a specific energy variation by as much as 24% (e.g., see 50 degrees orientation angle).

2.5 Model Simplification using Merchant's Shear Angle

During the model calculations presented above, irrespective of the zone axis, the mean value of the shear angle has been seen to be close to Merchant's shear angle solution. To further explore

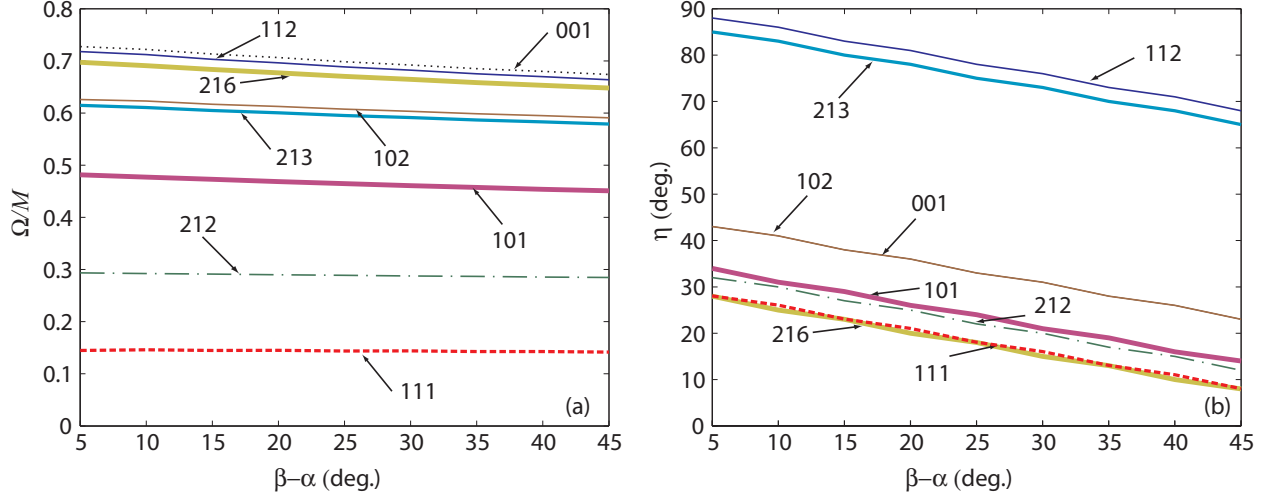


Figure 2.13: The effect of $(\beta - \alpha)$ on (a) the deviation of the specific energies, and (b) the phase angle of the specific energies.

this phenomenon, the specific energies are re-calculated for all crystallographic orientations about each zone axis by using Merchant's shear angle ϕ_M *without* the power minimization procedure and compared with the specific energies from the model. The power minimization is circumvented by substituting ϕ_M into Eq. (2.10), and determining the power from Eq. (3.1) for a given crystallographic orientation (i.e., A , B , F , G and H are known). As shown in Fig.2.16 for a representative case of $(\beta - \alpha)$ of 10 degrees and $[2\ 1\ 2]$ zone axis, the specific energy from the model is seen to be always less than or equal to that calculated using ϕ_M . This is an expected result since the complete model will match the one that is calculated using ϕ_M only when the shear angle determined from the model is equal to ϕ_M . In other cases, the complete model will result in a shear angle that gives the minimum power (and thus the minimum specific energy), which is less than the power (specific energy) that is calculated by using ϕ_M . Moreover, an exact match between the amplitude of variation (Ω) and a close match between the mean (M) was found in all cases.

The mathematical description of the model can be considered to explain the above observations. The power minimization procedure can be expressed as

$$\frac{\partial P_t}{\partial \phi} = 0, \quad (2.23)$$

which is solved to determine the shear angle ϕ . For a given zone axis, the expression for total power

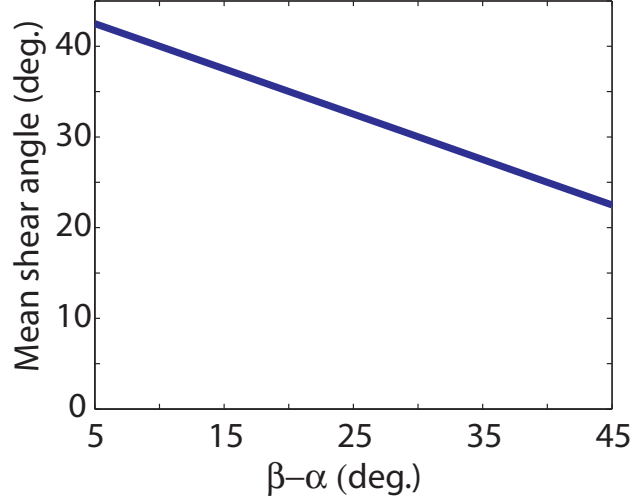


Figure 2.14: The effect of $(\beta - \alpha)$ on mean value of shear angles for all analyzed zone axes.

can be simplified from Eq. (3.1) as

$$P_t = g(\phi - \theta) f(\phi), \quad \text{where} \quad f(\phi) = \frac{(hwV) \cos(\beta - \alpha)}{\sin(\phi) \cos(\phi + \beta - \alpha)}. \quad (2.24)$$

Substituting this equation into Eq. (2.23) results in

$$f \frac{\partial g}{\partial \phi} + g \frac{\partial f}{\partial \phi} = 0. \quad (2.25)$$

The shear angle from the Merchant's solution is obtained from

$$\frac{\partial f}{\partial \phi} = 0, \quad (2.26)$$

which implies from Eq. (2.25) that ϕ_M is the solution of the complete model if

$$\left. \frac{\partial g}{\partial \phi} \right|_{\phi=\phi_M} = 0. \quad (2.27)$$

From Eqs. (2.10) and (3.1), it can be shown that

$$\frac{\partial g}{\partial \phi} + \frac{\partial g}{\partial \theta} = 0. \quad (2.28)$$

Same conclusion can be arrived at by realizing that g is a function of $(\phi - \theta)$. Therefore, Eqs. (2.27)

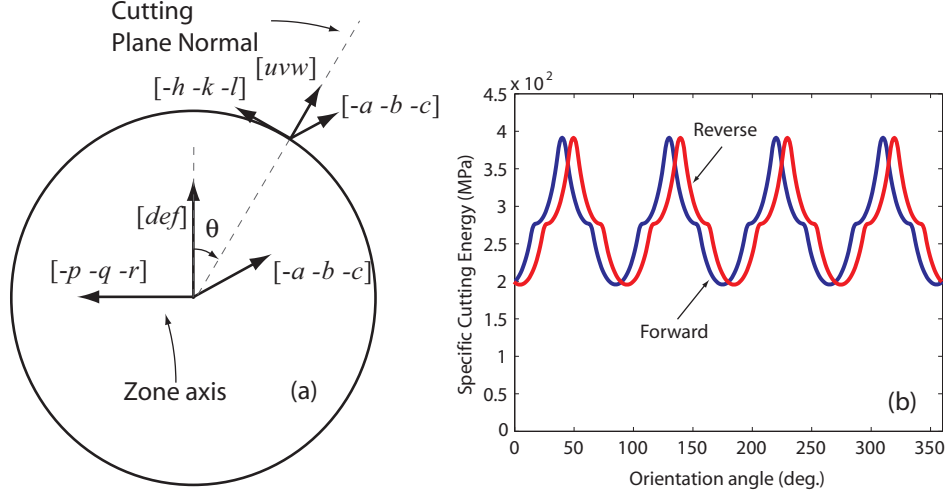


Figure 2.15: (a) Cutting and crystallographic orientations indicating the reversal of cutting direction, (b) Comparison of variation in specific cutting energy for forward and reverse direction with orientation angle for $[0\ 0\ 1]$ zone axis.

and (2.28) imply that ϕ_M is the shear angle solution if and only if

$$\frac{\partial g}{\partial \theta} = 0. \quad (2.29)$$

This indicates that the Merchant's shear angle is the solution of the model when the slope of power (and the specific energy) with θ is zero. This conclusion agrees with the observations from Fig.2.16(b); since the slope is zero at the extremum points, the complete solution and the simplified solution using ϕ_M will match one another at those points. Therefore, the amplitude of variation will be exactly the same for both cases, and the mean values will be similar (while not necessarily exact). Thus, rather than exact dependence of specific energies on crystallographic orientation, if the amplitude of variation and mean value are of interest, the Merchant's shear angle can be used without the power minimization procedure, thereby simplifying the calculations but yet still indicating the effect of crystallographic anisotropy.

2.6 Summary

This chapter presented a machining model and analysis for cutting forces while machining single-crystal fcc metals. The plasticity-based machining force model combined Bishop and Hill's crystal plasticity model with Merchant's orthogonal cutting model. An experimental validation of the model was carried out by using data from the literature for aluminum [19] and copper [25, 40]

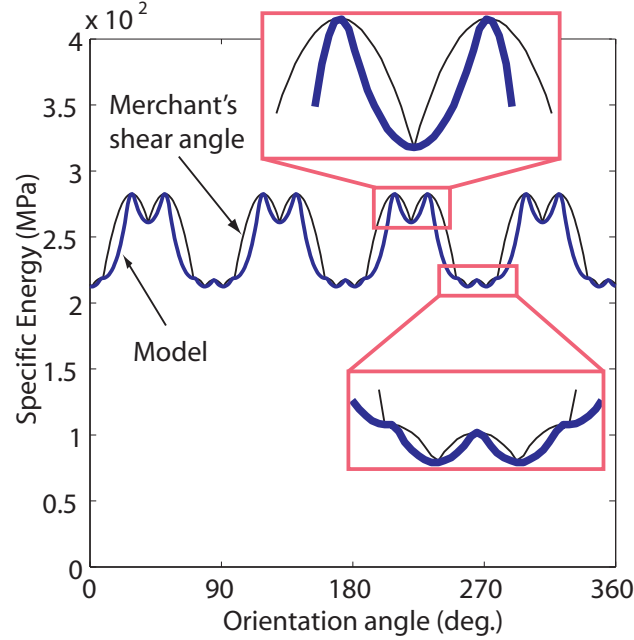


Figure 2.16: Comparison between specific energies calculated for $[2\ 1\ 2]$ zone axis using the complete model and using the simplified model with Merchant's shear angle.

single-crystal machining. The model was then applied to analyze the effect of friction, rake angle, and crystallographic orientation on specific energies for eight crystallographic orientations that are uniformly distributed over the basic stereographic triangle.

The following items can be summarized from the simplified model;

- A good match (in terms of average and amplitude of variation about zone axes) between the model and the experiments (from literature) is seen for both copper and aluminum single crystals.
- The variation of the mean specific energy with the zone axis is seen to be relatively small. Increased rake-face friction and/or reduced rake angle are seen to increase the mean specific energies. The thrust specific energy is found to be more sensitive to friction and rake angle variations than the cutting specific energy.
- Although the deviation (about the mean) of the specific energies with crystal orientation changes significantly with the zone axis, the friction and rake angles have a small effect on the deviation for a given zone axis. The minimum deviation is observed for the $[1\ 1\ 1]$ zone axis, which is the zone axis with the maximum crystallographic symmetry.

- For a given zone axis, the friction and rake angles affect (induce a phase shift) the orientation that produces the maximum specific energy. This phase shift changes linearly with the difference between the friction and rake angles.
- The mean shear angle for all zone axes is seen to be approximately the same. Furthermore, the mean shear angle value is found to be approximately equal to Merchant's shear angle. An analytical derivation proved that the use of Merchant's shear angle, instead of the complete solution (minimization), results in an exact match at the maximum and minimum specific energies. Thus, a simplified model, where the Merchant's shear angle solution is used, is also proposed.

Although the simplified model provides a clear methodology for incorporating the crystallographic anisotropy into machining model, it consists of a few important shortcomings as listed below.

- The model results in (atleast) four-fold symmetry about all zone axes even if the zone axis does not possess a structural four fold symmetry. While the model is consistent in explaining why this happens, the physical evidence for such four-fold symmetry (for all zone axes) in forces is lacking.
- During machining, workpiece material undergoes large strain deformation (1~5), consequently the material hardens, thus changing material properties (like CRSS) during the operation.
- Lastly, in the case of crystallographic materials, due to the kinematics of slip the lattice orientation changes with deformation. The simplified model discounts this physical phenomenon while arriving at force predictions.

To address these issues, a rate-sensitive plasticity based machining force (specific energy) (RSPM) model is developed in the next chapter.

Chapter 3

Rate Sensitive Plasticity based Machining Model

In this chapter, a rate-sensitive plasticity based machining force (specific energy) (RSPM) model for incorporating crystallographic anisotropy is presented. In contrast to the existing models [34, 36, 37, 45] the current work considers the deformation to be “large” within a deformation zone (rather than a plane), and incorporates the effects of lattice rotation and strain hardening in arriving at specific energies. Minimization of total power is used in obtaining the shear angle, and specific energies. Subsequently, rate-sensitive constitutive equations combined with hardening and kinematics of single crystal deformation (including lattice rotation) are used in arriving at the specific energy values. In the following, we first describe the kinematic model that relates different force components and shear angle to cutting geometry. Next, the calculation of incremental and total plastic work for a single crystal fcc workpiece is described, including the rate sensitive constitutive equations, lattice rotation, and strain hardening. The modeling procedure is then outlined. We then outline a calibration procedure to obtain material parameters from the cutting-force data, and present experimental validation of the model.

3.1 Model description

The orthogonal machining considered in this work is described in Fig. 3.1(a), where α is the rake angle, ϕ is the shear angle, V is the cutting velocity, w is the width of cut, and h is the uncut chip thickness. The geometry shown in Fig. 3.1(a) assumes that the radius of cutting edge is very small

compared to the uncut chip thickness, and the workpiece undergoes a plane-strain deformation during machining.

The forces encountered during machining by the tool, the workpiece and the chip are shown in Fig. 3.1(b). The (total) machining force F can be decomposed into its cutting edge components of cutting force F_c and the thrust force F_t ; or to its rake face components of friction force F_f and the normal force F_n . The relationship between the different forces can be obtained by considering a force equilibrium between the chip, the workpiece and the tool [16]. This relationship is represented in Fig. 3.1(b) using Merchant's force circle diagram.

The modeling approach considered here is based on the minimization of total machining power, including the power spent in shearing the material inside the primary shear zone, and the power dissipated through friction between the rake face and the chip. For the calculation of the shearing power, (strain) rate-sensitive constitutive equations and kinematics of crystal plasticity that capture crystallographic anisotropy, strain hardening and lattice rotation are used. *The minimization of the total machining power over the geometrically allowable shear angle candidates is performed to obtain a shear angle solution.* Subsequently, the minimum total power is used to calculate the cutting force and the specific cutting energy.

The total power can be calculated as a summation of the plastic power \dot{W}_p (for shearing) and the friction power \dot{W}_f (for overcoming friction on the rake face) as [16]

$$P_t = \dot{W}_f + \dot{W}_p. \quad (3.1)$$

The power spent for creation of new surface is assumed to be negligible with respect to the plastic and friction powers. The friction power, \dot{W}_f , can be written in terms of friction force F_f and chip velocity V_c [16] as

$$\dot{W}_f = F_f V_c, \quad (3.2)$$

where

$$V_c = V \frac{\sin(\phi)}{\cos(\phi - \alpha)}. \quad (3.3)$$

Using Merchant's force circle diagram shown in Fig. 3.1(b), the friction force can be written in

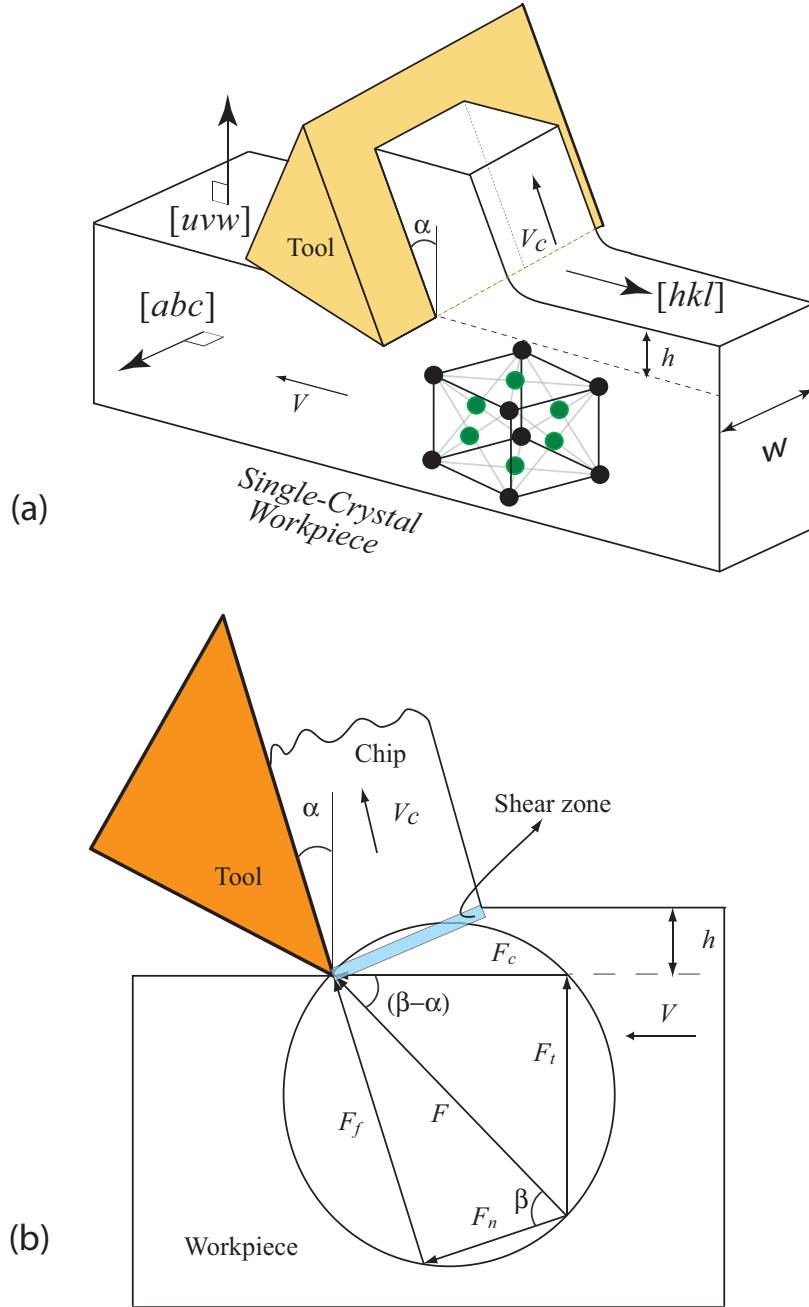


Figure 3.1: (a) The geometry of orthogonal cutting process, indicating the workpiece zone axis $[abc]$, cutting direction $[hkl]$, and cutting plane normal $[uvw]$, and (b) Components of the machining force, Merchant's force-circle diagram, and the shear zone.

terms of the tangential cutting force F_c as

$$F_f = F_c (\sin(\alpha) + \tan(\beta - \alpha) \cos(\alpha)), \quad (3.4)$$

where β is the friction angle, which is related to the coefficient of friction μ as

$$\tan \beta = \mu. \quad (3.5)$$

The shearing power, \dot{W}_p , can be obtained from the product of volumetric flow rate of the material and specific work of plastic deformation W_p as

$$\dot{W}_p = (hwV) W_p, \quad (3.6)$$

Substituting Eqs. (3.2)-(3.6) in Eq. (3.1), the total power can be written as

$$P_t = (hwV) W_p + F_c V \frac{(\sin(\alpha) + \tan(\beta - \alpha) \cos(\alpha)) \sin(\phi)}{\cos(\phi - \alpha)}. \quad (3.7)$$

The total machining power can also be written in terms of cutting force and cutting speed as

$$P_t = F_c V. \quad (3.8)$$

Substituting Eq. (3.8) into Eq. (3.7), an expression for total machining power in terms of plastic work can be obtained as

$$P_t = hwV W_p \left(1 - \frac{(\sin(\alpha) + \tan(\beta - \alpha) \cos(\alpha)) \sin(\phi)}{\cos(\phi - \alpha)}\right)^{-1}. \quad (3.9)$$

Equation (3.41) indicates that, for given shear angle, cutting geometry and coefficient of friction, the total power can be calculated if the work done in plastic deformation is known. It should be noted here that more sophisticated friction models that consider non-uniform stress distribution on the rake face can be integrated into the model presented in this work.

3.2 Calculation of Plastic work

As seen in the previous section (from Eq. (3.41)), calculation of the total power requires knowledge of the plastic work. The plastic work can be calculated based on the material properties and shear angle, which, in turn, is determined using a suitable shear angle criterion. For example, for the idealized case of isotropic, non-hardening material, the product of yield shear stress and the shear strain determines the plastic work. Alternately, under a mechanistic modeling approach, the shear force is expressed in terms of shear stress (a calibrated material parameter), following which the

plastic power is obtained as the product of the shear force and the shear velocity [46]. To determine the shear angle, different criteria, including maximum shear stress and minimum total power [46], have been considered in the literature. When the cutting process occurs within a single crystal, or within a few crystals, the strong plastic anisotropy of the workpiece material cannot be ignored. In that case, the isotropic-material assumption becomes invalid, and the solution of process mechanics necessitates the use of crystal-plasticity techniques.

3.2.1 Plastic deformation in single-crystal fcc metals

Plastic deformation in crystalline metals at ambient conditions is largely due to the motion (slip) of crystal defects called dislocations along specific crystal directions (slip direction) on specific crystallographic planes (slip planes). A pair of slip plane and slip direction forms a slip system. For face centered cubic (fcc) materials considered in this document, the family of $\{1\ 1\ 1\}$ planes and $\langle 1\ 1\ 0 \rangle$ directions form the slip planes and slip directions, respectively. In fcc materials, there are 12 such slip systems available, and any plastic strain applied to the material is accommodated by a combination of slips on the 12 slip systems. Since there exists only a finite number of slip systems (on particular orientations), the plastic response of the material varies with the orientation of applied shear strain, i.e., the material behaves anisotropically.

As a result of anisotropy, the amount of plastic work required to obtain a given amount of strain for a given orientation depends on the particular combination of slip systems that accommodates the deformation. For small deformations, Bishop and Hill's model can be used for evaluating the plastic work [41]. The plastic work for a given strain is calculated as the maximum of the value calculated over 56 yield vertices. The yield vertex resulting in the maximum value also determines the set (consisting of 6 or 8 slip systems, depending on the yield vertex) of *potentially* active slip systems. Since any combination of five independent slip systems (of the 6 or 8 slip systems that make up the vertex) can accommodate arbitrary plastic deformation, the determination of the yield vertex neither determines the specific slip systems nor the amount of slip on slip systems active during the deformation [47].

During the large deformations experienced in machining, as the material progressively deforms in the primary deformation zone, the lattice rotates (with respect to a fixed frame) and the material properties (such as the critical resolved shear stress ¹) change due to hardening. If lattice rotation and strain hardening are neglected [48], the plastic work can be calculated by dividing the

¹Critical resolved shear stress is the amount of stress required on a slip plane to cause slip on that particular plane

deformation into a number of small steps and applying the Bishop and Hill model at each step. However, when lattice rotation and strain hardening are incorporated, calculation of plastic work requires the amount of slip on the active slip systems to be determined, which cannot be obtained from the Bishop and Hill model.

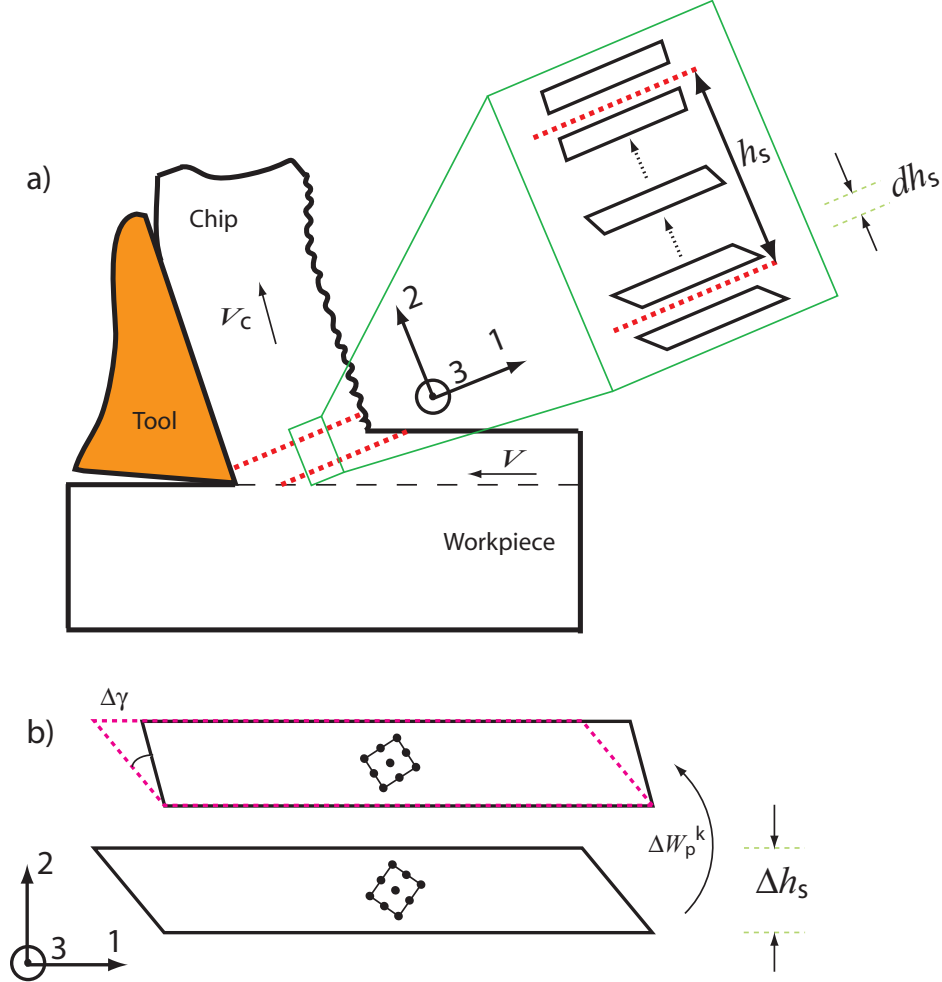


Figure 3.2: (a) Deformation in the primary deformation zone, (b) An incremental deformation $\Delta\gamma$ that occurs as a result of incremental plastic work ΔW_p^k .

As the material progressively deforms, lattice rotation causes the orientation of the crystal to change with respect to the coordinate system fixed with respect to the cutting geometry (1–2–3 frame in Fig. 3.2(a)). Figure 3.3 illustrates the lattice rotation and resulting change in the orientation for a simplified two dimensional crystal with two slip systems. In the figure, the lattice frame is represented by 1_l-2_l , and the fixed reference frame is represented by 1–2. For the two cases shown, the total deformations are identical (as observed from the initial and final shapes

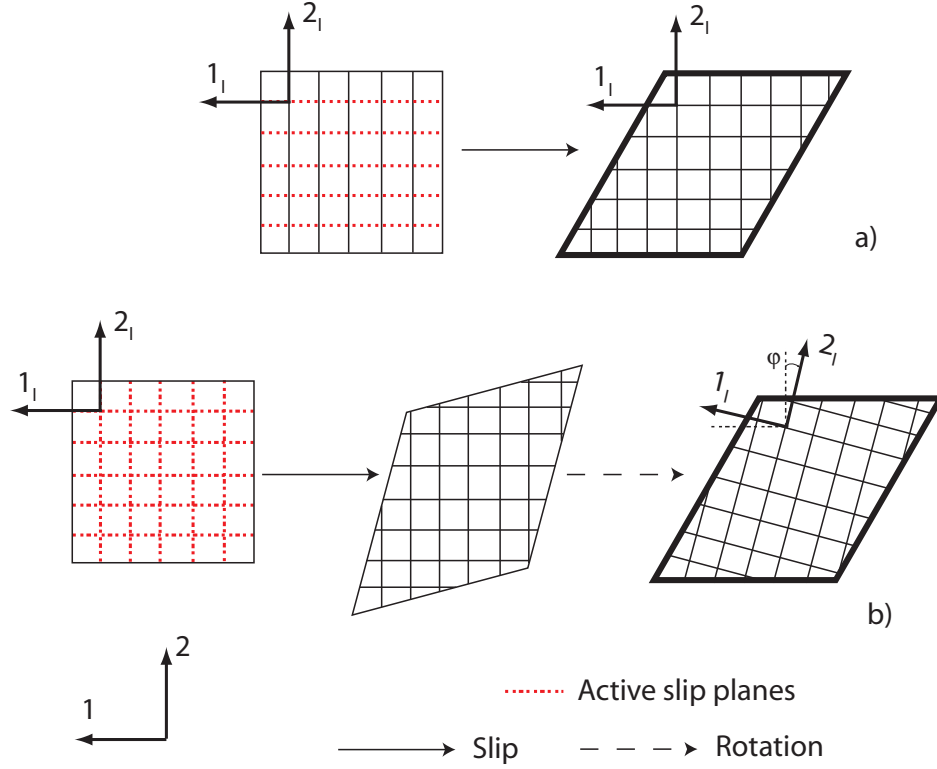


Figure 3.3: Illustration of the lattice rotation; the final deformation is a result of slip on (a) only one system (along 1_l), and (b) two slip systems (simultaneously along 1_l and 2_l), and a rotation. The same deformation is obtained with different lattice orientations.

of the element). For the element shown in Fig. 3.3(a), this deformation is obtained by slip on a single active slip system along the 1_l direction. For the element shown in Fig. 3.3(b), however, the two active slip systems operate simultaneously along the 1_l and 2_l directions. Note that a simple rotation is required in Fig. 3.3(b) to obtain the same orientation of the deformed element. Although the deformations are the same, the final crystal (lattice) orientations (1_l-2_l) are different in Fig. 3.3(a) and Fig. 3.3(b). While the lattice did not rotate in Fig. 3.3(a), activated slip systems in Fig. 3.3(b) required the lattice to be rotated by an angle of φ to achieve the same deformation.

There are two important consequences of lattice rotation to the calculation of shearing power. First, the determination of lattice rotation requires unique determination of the active slip systems. Such a unique determination of active slip systems is most easily obtained by using a rate-sensitive solution, in which the slip-rate on a slip system depends on the resolved shear stress on that slip system. Once the stress distribution within the material is determined, rate sensitive constitutive equations enable the identification of the active slip systems, and the amount of slip in each of those systems.

Second, the amount of work required to prescribe a fixed shear deformation of $\Delta\gamma$ depends on the lattice orientation immediately prior to the deformation. Since the lattice orientation varies during large deformation, an incremental approach to the calculation of plastic work is required.

The work done in the shear zone to impose the total strain γ can be written as

$$W_p = \int dW_p, \quad (3.10)$$

where dW_p is the incremental work required to cause an incremental engineering shear strain $d\gamma$ to a layer of material within the shear zone with the thickness dh_s . As a layer of material moves through the shear zone, it is progressively deformed. Therefore, unlike in earlier models [45], that assume an infinitesimally thin shear plane, the material here is considered to shear along a *finite* thickness shear zone, as shown in Fig. 3.2(a). Numerical evaluation of plastic work can be performed by discretizing the process into a finite number of steps. It is assumed that a material of finite thickness moves through the plastic deformation zone, undergoing a finite amount of shear at every step.

Considering an element with thickness $\Delta h_s = h_s/N_s$ and an elemental engineering shear strain $\Delta\gamma^k$ at the k -th step, Eq. (3.10) can be rewritten in a discretized form as

$$W_p \approx \sum_{k=1}^{N_s} \Delta W_p^k, \quad \text{where} \quad \gamma = \sum_{k=1}^{N_s} \Delta\gamma^k = N_s \Delta\gamma. \quad (3.11)$$

The amount of shear $\Delta\gamma^k$ at every step is assumed to be a constant value ($\Delta\gamma$), implying a constant rate of shear throughout the primary deformation zone. It should be noted that a sufficiently large number of steps must be considered to ensure that the calculated plastic work does not depend on the number of steps. A convergence study provided later addresses the selection of incremental strain, and consequently of the number of steps to be used in Eq. (3.11).

The strain-hardening phenomenon also necessitates incremental analysis of large deformations encountered during machining. The dislocation density within the deformation zone increases with increased amount of deformation. Existing dislocations within the material increases the resistance against the movement of dislocations, i.e., against slip. As a result, the amount of work required to induce an incremental strain of $\Delta\gamma$ on an element depends on the deformation history and lattice orientation of the element. Hence, ΔW_p^k is different at each step k and, unlike in [45], cannot be taken out of the summation sign in Eq. (3.11).

3.3 Incremental plastic work

The incremental plastic work at the k -th step, ΔW_p^k , can be expressed as a tensor inner-product of the stress tensor σ_w^k and the incremental strain tensor $d\epsilon_w$ as

$$\Delta W_p^k = \sigma_w^k : d\epsilon_w, \quad (3.12)$$

where the subscript w indicates the 1–2–3 coordinate frame (see Fig. 3.2). In the lattice frame of reference, the same equation can be written as

$$\Delta W_p^k = \sigma^k : d\epsilon^k, \quad (3.13)$$

where

$$\sigma^k = (P^k)\sigma_w^k(P^k)^T \quad \text{and} \quad d\epsilon^k = (P^k)d\epsilon_w(P^k)^T. \quad (3.14)$$

Here P^k represents the orthogonal transformation from sample reference frame (w) to the lattice frame of reference. Although the incremental strain tensor $d\epsilon_w$ in the workpiece frame is constant at each step due to constant incremental shear strain $\Delta\gamma$, the lattice rotation causes P^k to vary at each step, thereby causing the incremental strain tensor on the lattice frame ($d\epsilon^k$) to change at every step.

3.3.1 Calculation of incremental plastic strain

The incremental strain in the crystal frame depends on the plastic strain rate D^k . For the small displacement and displacement gradients experienced during an incremental deformation $\Delta\gamma$, the plastic strain is approximated as [49]

$$d\epsilon^k = D^k \Delta t, \quad (3.15)$$

where Δt is the (incremental) time it takes for deformation $\Delta\gamma$ to occur, *viz.*,

$$\Delta t = \frac{\Delta\gamma}{\dot{\gamma}}, \quad (3.16)$$

where

$$\dot{\gamma} = V \sin(\phi) \frac{\gamma}{h_s} \quad (3.17)$$

is the strain rate. The strain rate $\dot{\gamma}$ is assumed to be constant within the deformation zone. The plastic strain rate D^k is defined as the symmetric part of the velocity gradient L^k . The velocity gradient represents the spatial rate of change of velocity, whose components L_{ij}^k are given by

$$L_{ij}^k = \frac{\partial v_i^k}{\partial x_j^k}, \quad (3.18)$$

in terms of velocity field v^k . This velocity field in the lattice reference frame arises as a result of slip rates on slip systems. The plastic strain rate can subsequently be written as

$$D^k = \frac{(L^k) + (L^k)^T}{2}. \quad (3.19)$$

The velocity gradient L^k is obtained through the coordinate transformation of velocity gradient L_w in the sample $(1 - 2 - 3)$ frame. For the simple-shear deformation shown in Fig. 3.2(b), the constant (step-independent) velocity gradient in the sample frame can be written as

$$L_w = \begin{bmatrix} 0 & \dot{\gamma} & 0 \\ 0 & 0 & 0 \\ 0 & 0 & 0 \end{bmatrix}. \quad (3.20)$$

In calculating the shear rate $\dot{\gamma}$ in Eq. (3.17), the total shear strain is expressed from the geometry of the deformation as [16]

$$\gamma = \frac{\cos(\alpha)}{\sin(\phi) \cos(\phi - \alpha)}. \quad (3.21)$$

For the thickness of the deformation zone h_s , Oxley's [50] assumption that considers the h_s to be 10% of the shear-plane length l_s is used, *viz.*,

$$h_s = \frac{l_s}{10} = \frac{h}{10 \sin \phi}. \quad (3.22)$$

From the coordinate transformation of velocity gradient in the sample frame L_w , the velocity

gradient in the crystal frame L^k can be written as,

$$L^k = (P^k)L_w(P^k)^T + \dot{P}^k(P^k)^T, \quad (3.23)$$

where \dot{P}^k represents the rate of the change of orthogonal transformation P^k [51]. The second term in Eq. (3.23) is related to the rotation of lattice with respect to fixed frame of reference and arises from the fact that the crystal frame of reference is a rotating reference frame.

The representation given in Eq. (3.23) can be used to express the symmetric part of strain rate D^k as

$$D^k = \frac{(P^k)L_w(P^k)^T + (P^k)L_w^T(P^k)^T}{2}. \quad (3.24)$$

In arriving at this expression, it was considered that $\dot{P}^k(P^k)^T$ is a skew-symmetric matrix, i.e.,

$$\dot{P}^k(P^k)^T + (P^k)(\dot{P}^k)^T = 0. \quad (3.25)$$

Equation (3.25) can be obtained by taking the time derivative of orthogonality condition $P^k(P^k)^T = I$. Thus, from Eq. (3.15) and Eq. (3.24), the incremental strain $d\epsilon^k$ can be expressed in terms of the (known) velocity gradient L_w , and the (known) coordinate transformation matrix P^k .

3.3.2 Calculation of the stress tensor

To calculate the incremental work in Eq. (3.12), in addition to the incremental strain $d\epsilon^k$, the stress tensor σ^k must be determined. For a rate-sensitive material, a standard way to express the relation between the stress and the strain rate on the s -th slip system ($\dot{\gamma}_s^k$) is to use a power law [47] given by

$$\dot{\gamma}_s^k = \dot{\epsilon} \left(\left| \frac{m_s : \sigma^k}{\tau^k} \right| \right)^n \text{sgn}(m_s : \sigma^k), \quad (3.26)$$

where m_s is the symmetric part of Schmid tensor (see Appendix), τ^k is the flow stress at the k -th step (the flow stress τ_k corresponds to the critical resolved shear stress in a rate-insensitive material), and n is the exponent of rate sensitivity. The flow stress τ^k is updated at each step to incorporate strain hardening. The orientation of the slip system with respect to crystallographic frame is imposed using m_s , and thus, the tensor inner product ($m_s : \sigma^k$) represents the resolved shear stress on the s -th slip system. Equation (3.26) provides a unique relationship between the

slip rate on a slip system and the resolved stress on that slip system. In a rate insensitive case, no such relationship exists. The (scalar) absolute strain rate $\dot{\epsilon}$ in Eq. (3.26) is used as the reference strain rate, around which Eq. (3.26) is valid. In other words, for a set of material parameters (n and τ_k) Eq. (3.26) is not valid over a wide range of strain rates [47]. Hence, the reference strain rate is chosen as the average value of the strain rate over all geometrically possible shear angles (i.e., $0 \leq \phi \leq (90 - (\beta - \alpha))$), calculated using Eq. (3.16).

The velocity gradient L^k in the lattice frame is a result of slip rates on different slip systems. Mathematically, the velocity gradient L^k can be represented as

$$L^k = \sum_{s=1}^{12} \dot{\gamma}_s^k (b_s \otimes n_s), \quad (3.27)$$

where $(b_s \otimes n_s)$ represents the Schmid tensor for the s -th slip system, and is known for every slip system (see Appendix). Equating the symmetric part of L^k in Eq. (3.27) and to that in Eq. (3.23) gives

$$D^k = \sum_{s=1}^{12} \dot{\gamma}_s^k m_s. \quad (3.28)$$

Substituting Eq. (3.26) into Eq. (3.28) results in

$$D^k = \sum_{s=1}^{12} \dot{\epsilon} \left(\left| \frac{m_s : \sigma^k}{\tau^k} \right| \right)^n \text{sgn}(m_s : \sigma^k) m_s. \quad (3.29)$$

In the above equation, the stress tensor σ^k is unknown, whereas plastic strain rate D^k is known from Eq. (3.24). Since the symmetric plastic strain rate D^k has five independent components (as a result of zero volumetric strain rate during plastic deformation), whereas σ^k has six, solving the Eq. (3.29) allows the unique determination of only the deviatoric component of stress. This means that any arbitrary value for hydrostatic stress will satisfy the Eq. (3.29). Since hydrostatic stress performs work only in the presence of volumetric strain, which is zero in the case of plastic deformation, the plastic work calculation is unaffected by its non-uniqueness. Furthermore the resolved stress given by $(m_s : \sigma^k)$ is also unaffected by the value of hydrostatic stress, since the trace of m_s (which is equal to $(b_s \cdot n_s)$) is zero for any slip system.

For the iterative solution of the set of nonlinear equations given in Eq. (3.29), a set of initial stress values are required. In this work, the initial stress values are obtained from Bishop and Hill model for a strain of $D^k \Delta t$. The calculated yield vertex, which depends on the flow stress τ^k and

the lattice orientation, results in the coefficients A^k , B^k , C^k , F^k , G^k and H^k . The initial value of the stress is then calculated in terms of these coefficients as

$$\begin{aligned} \sigma_{11} &= \frac{C^k - B^k}{3}, \quad \sigma_{12} = H^k, \quad \sigma_{13} = G^k, \\ \sigma_{22} &= \frac{A^k - C^k}{3}, \quad \sigma_{23} = F^k, \quad \text{and} \quad \sigma_{33} = \frac{B^k - A^k}{3}. \end{aligned}$$

Choosing the initial stress through the Bishop and Hill's solution implies that the stress state σ^k calculated from Eq. (3.29) will be in the vicinity of the yield vertex calculated from the Bishop and Hill model [47]. Since the effect of rate sensitivity is to smooth or round off the yield vertices, thus providing a well defined normal (representing the direction of strain), it is expected that for a given strain direction, the value of stress is close to the vertex.

3.3.3 Determination of lattice reorientation

The plastic deformation causes the lattice to rotate within the deformation zone with respect to a fixed frame of reference (see Fig. 3.3). The coordinate transformation matrix P^k must be updated at every step to take into account the rotation of lattice. Equation (3.23) allows the determination of \dot{P}^k (consequently the change in P^k), provided that the velocity gradient in the crystal frame L^k is known. The calculation of stress tensor from Eq. (3.29) allows the calculation of slip rates on each slip system from Eq. (3.26). Subsequently, the velocity gradient L^k is calculated from Eq. (3.27), allowing the determination of \dot{P}^k as

$$\dot{P}^k = \Omega^k P^k, \quad (3.30)$$

where the lattice spin Ω^k is given by the skew-symmetric part of the velocity gradient as

$$\Omega^k = L^k - (P^k)L_w(P^k)^T. \quad (3.31)$$

To maintain the orthogonality of P^k , an Euler angle-based scheme is used to update P^k using the components of lattice spin (see Appendix).

3.3.4 Incorporation of strain hardening

As described above, the deformation history of a material changes the plastic behavior of the material through the strain hardening phenomenon. To incorporate strain hardening, the (reference)

flow stress to be used in the subsequent step τ^{k+1} can be written as [47]

$$\tau^{k+1} = \tau^k + \Theta^k \Delta(\Gamma^k), \quad (3.32)$$

where Θ^k is the current hardening-slope and $\Delta(\Gamma^k)$ represents the sum of absolute value of slips, i.e.,

$$\Delta(\Gamma^k) = \sum_{s=1}^{12} |\dot{\gamma}_s^k| \Delta t. \quad (3.33)$$

Updating the flow stress through Eq. (3.32) imposes the isotropic-hardening assumption, which asserts that each slip system experiences the same strain hardening irrespective of the amount of slip on that particular slip system [47]. The current hardening-slope Θ^k can be expressed by a power law relationship as

$$\Theta^k = \Theta_o \left(1 - \frac{(\tau^k - \tau_o)}{(\tau^v - \tau_o)}\right)^a, \quad (3.34)$$

where Θ_o , τ^v , $\tau^1 = \tau_o$, and a are the initial hardening slope, the saturation stress, the initial reference stress, and the exponent of the power law, respectively [47]. These four parameters are material constants that are determined through experimental calibration. Typical behavior of the reference stress with cumulative slip is shown in Fig. 3.4.

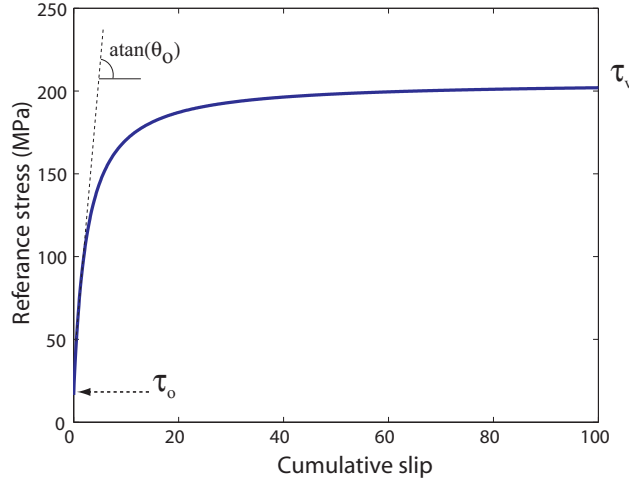


Figure 3.4: Typical behavior of reference stress.

3.4 Modeling procedure

For a given cutting orientation, the range of physically possible shear angles is given by $(0, (90 - (\beta - \alpha)))$. While the lower bound of the range ensures that the chip is flowing away from the material (see Eq. (3.3) and Fig. 3.1(b)), the upper bound ensures that the force in the direction of shear, given by $F \sin(\phi + \beta - \alpha)$ [46], stays positive, implying that the plastic work is positive. Within this range, the shear angle candidates are selected with a one degree increment to evaluate the total power using the following procedure. A typical variation of total power with shear angle candidate is shown in Fig. 3.5. As expected the variation of power (with shear angle) around the minimum is observed to be very small (because $\partial P_t / \partial \phi = 0$ at minimum total power). Consequently, the value of total power stays within 1% of minimum total power for a range of shear angle candidates around the shear angle producing minimum total power (in the Fig. 3.5, this range is ± 2 degrees). Thus, a choice of one degree increment keeps the errors in forces (see Eq. (3.35)) within 1% while significantly reducing the computational burden associated with the solution.

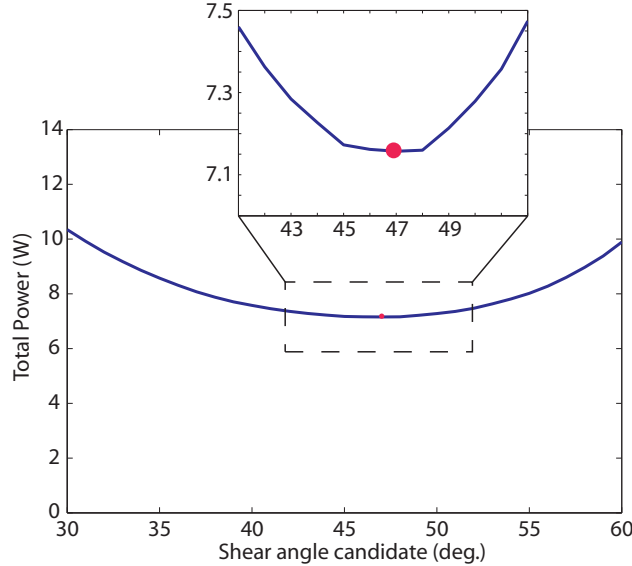


Figure 3.5: Typical behavior of total power with shear angle candidates.

To calculate the total power for a candidate shear angle, the value of the shear strain is obtained from Eq. (3.21). Equation (3.11) indicates that the total strain γ is divided into N_s identical incremental strains $\Delta\gamma$. The selection of the incremental strain value, thus N_s , is completed through a numerical convergence study outlined later. With decreasing values of $\Delta\gamma$, it is seen that plastic work reaches a limiting value. The actual value of $\Delta\gamma$ is chosen such that the calculated plastic work is within 0.25% of this limiting value. The value of strain rate is simultaneously evaluated

using Eq. (3.17), following Oxley's assumption for the thickness of shear zone (Eq. (3.22)). The calculated strain rate is then used to evaluate the velocity gradient L_w in the sample frame using Eq. (3.20).

The incremental strain $d\epsilon^k$ for the chosen $\Delta\gamma$ is evaluated using Eq. (3.15), where the plastic strain rate D^k is obtained from Eq. (3.24) using the known L_w , and P^k . Subsequently, the stress σ^k is calculated using Eq. (3.29). The incremental plastic work is then evaluated following Eq. (3.13). The stress σ^k is also used to evaluate the individual slip rates on each system using the constitutive equation (Eq. (3.26)). Thus obtained slip rates are used to calculate the velocity gradient in the lattice frame using Eq. (3.27). The lattice rotation and the strain hardening are updated at the end of every step. Lattice rotation is incorporated by updating the orientation matrix P^k using the lattice spin calculated from Eq. (3.31) through an Euler angle based update scheme (see Appendix). For the first step ($k = 1$), the initial orientation of the lattice is used to obtain the orientation matrix. Strain hardening is incorporated by updating the reference stress τ^k following Eq. (3.32). The cumulative slip (see Eq. (3.42)) necessary for reference stress update is obtained by summing the individual slips on each slip system.

The procedure is repeated for the number of steps given by Eq. (3.11). The total plastic work thus obtained from Eq. (3.11) is subsequently used in Eq. (3.41) to evaluate the total power.

Following the above detailed procedure, the total power is calculated for each candidate shear angle. The shear angle that produces the minimum total power P_t^{min} is then selected as the shear angle for the specified conditions (i.e., orientation, rake angle, friction angle). The corresponding cutting force F_c and thrust force F_t can be obtained using the total power as

$$F_c = \frac{P_t^{min}}{V}, \quad \text{and} \quad F_t = \frac{P_t^{min} \tan(\beta - \alpha)}{V}. \quad (3.35)$$

The corresponding specific cutting energy (u_c) and specific thrust energy (u_t) can be obtained by dividing the forces by chip area (a), i.e.,

$$u_c = \frac{F_c}{a} = \frac{F_c}{hw} \quad \text{and} \quad u_t = \frac{F_t}{a} = \frac{F_t}{hw}. \quad (3.36)$$

A calibration scheme for identifying the aforementioned material properties from the cutting forces is presented in the following section. Subsequently, experimental validation of the model (for copper and aluminum single-crystals) is presented. The model is then used to analyze the effects of rake angle and coefficient of friction, as well as the material properties on machining forces.

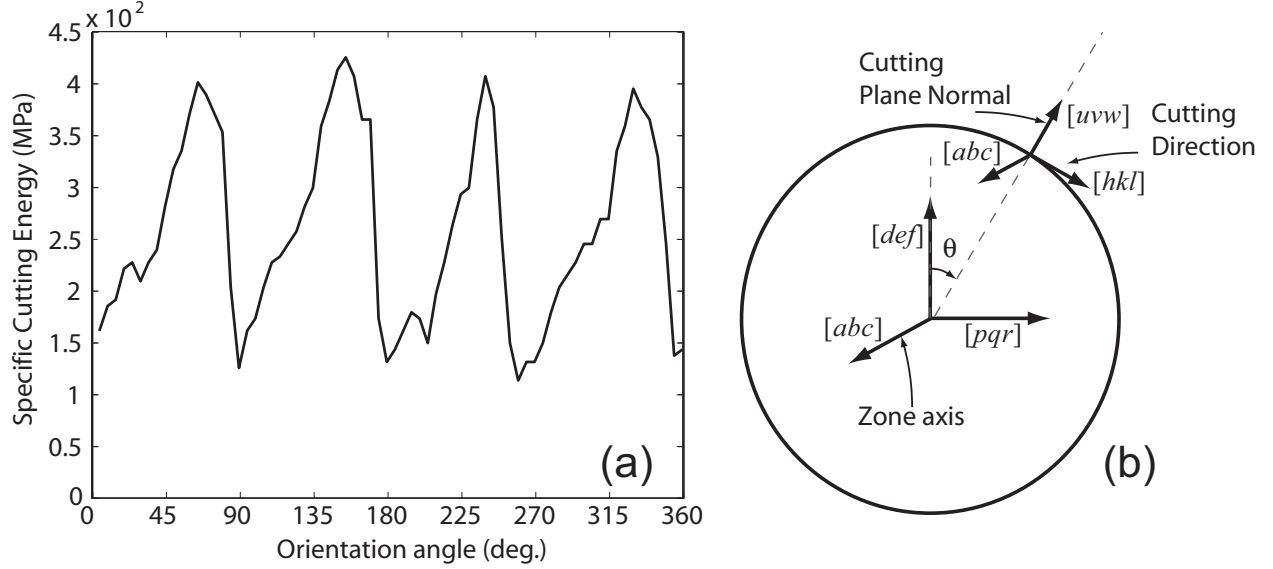


Figure 3.6: (a) Typical specific energy data from experiments as it varies with the orientation angle θ of the cutting plane, and (b) the definition of the zone axis, cutting direction, and cutting-plane orientation.

3.5 Calibration

The machining force (specific energy) model developed above requires the initial hardening slope Θ_o , the saturation stress τ_v , the initial reference stress τ_o , the exponent of the power law a , and the exponent of rate sensitivity n . Due to the unavailability of these parameters under machining conditions, a calibration procedure is used for determining the material parameters. Available specific energy data [19] on plunge-turning of single crystal face centered cubic (fcc) metals is used for performing the calibration.

Figure 3.6(a) shows a typical specific cutting energy data obtained when turning a single-crystal fcc material. As the orientation angle (θ) varies from 0 to 360 degrees (see Fig. 3.6(b)), the specific energy varies in a cyclic fashion due to the crystallographic symmetry about the zone axis (denoted by $[abc]$ in Fig. 3.6(b)).

3.5.1 Calibration Procedure

The calibration procedure required for obtaining the material parameters depends on the formulation of the model. In cases where the formulation lends itself to writing the specific energies explicitly in terms of material parameters, the least square method can be used as the calibration

procedure [52]. In the current model, due to the rotation of lattice during deformation, the relationship between the specific energy and material parameters is implicit and nonlinear. Consequently, least square algorithm based methods cannot be applied to perform the calibration. Instead, the calibration procedure is posed as a minimization problem, where the error between the experimental and predicted specific energies is minimized to obtain the material parameters. The minimization is performed by using the Kriging-based SuperEGO (efficient global optimization) program [53].

SuperEGO is a Kriging-based program to perform constrained optimization [53] in the form of

$$\min f(x) \quad \text{over } x, \quad (3.37)$$

$$\text{subject to } g(x) \leq 0. \quad (3.38)$$

The program is intended for problems where the number of independent variables (dimension of x) is relatively small (less than 10).

During calibration of material parameters, the root-mean-square error between the simulated and experimental specific cutting energies is used as the function ($f(x)$ in Eq. 3.37) to be minimized. The root-mean-square error e_r is defined as

$$e_r(\Theta_o, \tau_v, \tau_o, a, n) = \sqrt{\frac{\sum_{i=1}^{N_d} |u_{cm_i}(\Theta_o, \tau_v, \tau_o, a, n) - u_{ce_i}|^2}{N_d}}, \quad (3.39)$$

where u_{cm_i} and u_{ce_i} represent the specific cutting energy from the model and the experiment, respectively, for the i^{th} experimental data point. The number of available experimental points is represented by N_d in Eq. (3.39). The material parameters $x = [\tau_o, \Theta_o, \tau_v, a, n]$ are chosen as the independent parameters for the optimization. For the calibration, the minimization algorithm is used without any constraint functions.

The algorithm first completes a space-filling design of experiments (DOE) over the specified range for material constants. For each set of parameters ($x = [\tau_o, \Theta_o, \tau_v, a, n]$), the value of the minimization function ($f(x) = e_r$) is calculated. Subsequently, a polynomial Kriging meta-model of $f(x)$ is obtained through curve-fitting using the results of the DOE. Subsequently, the infill sampling criteria [53] is maximized to determine the parameter values for the next iteration ($x = [\tau_o, \Theta_o, \tau_v, a, n]$). The Kriging meta-model is then updated using the results from the new iteration. The process is repeated until the termination criteria is met. In the current case, if the change in the error value of next iterate is observed to be less than 0.5 % for four consecutive iterations, then the algorithm is terminated.

Figures 3.7(a) and 3.7(b) show the typical variation of the iterate points and the root-mean-square error e_r with increased number of iterations, respectively. The first 60 iterations shown in Fig. (3.7) are comprised of the initial space-filling DOE, following which the optimization is continued until the termination criterion is met.

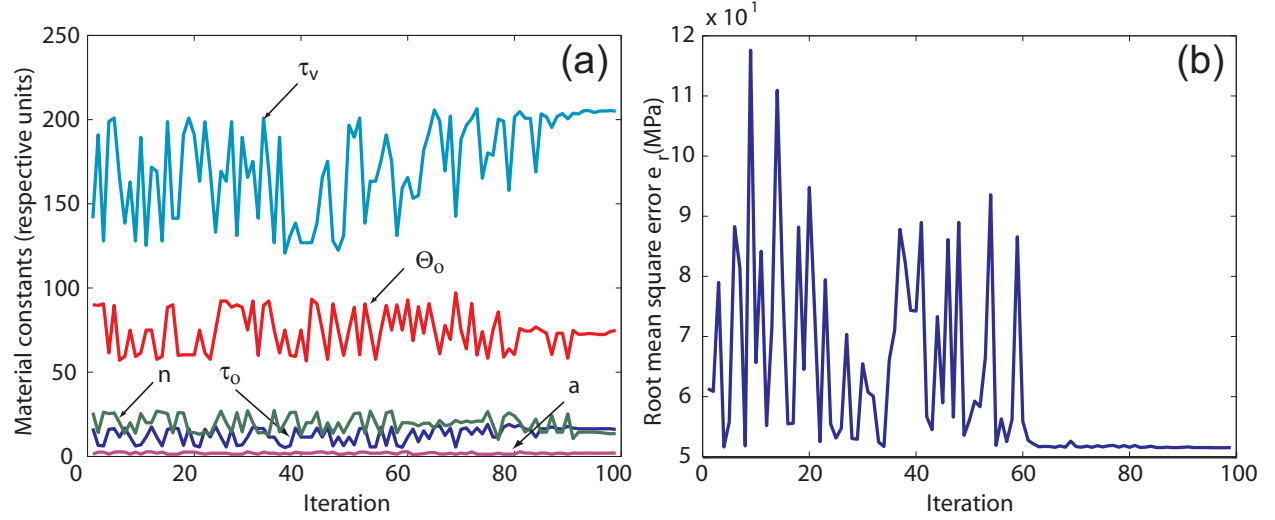


Figure 3.7: Typical iterations during the Kriging-based calibration procedure: (a) iteration points for the material parameters, and (b) the root mean squared error between the experimental data and the model with specified parameters. The first 60 steps involve a space-filling design-of-experiments.

3.5.2 Calibration for Aluminum and Copper

Using the calibration algorithm and experimental data from [19], the material parameters for aluminum and copper single crystals have been determined. For both materials, the experimental specific energies (in the format of Fig. 3.6(a)) for the cutting directions about [001] zone axis are used during the calibration. It should be noted that the calibration algorithm does not alter the effect of crystal symmetry (cyclic behavior) observed in the specific energies. The crystal symmetry and the overall shape of the specific energies are imposed by the RSPM model.

For aluminum, the calibration data was obtained at the cutting velocity, uncut chip thickness, and average width of cut of 0.44 mm/s, 0.11 mm, and 1.43 mm, respectively [19]. The rake angle is 40 degrees, and the friction angle calculated from the ratio of specific cutting and thrust energy is observed to vary between 45 degrees and 55 degrees [19]. An average friction angle of 50 degrees was used while performing the calibration. For the copper single crystals, the cutting velocity, uncut chip thickness and average width of cut were 0.55 mm/s, 0.11 mm, and 2.35 mm, respectively. An

Table 3.1: Material parameters obtained from calibration for single-crystal aluminum and single-crystal copper.

Material	τ_0 (MPa)	n	Θ_0 (MPa)	τ_v (MPa)	a
Aluminum	16.43	13.8	72.44	205.11	1.88
Copper	56.69	20.33	341.53	483.36	1.00

average friction angle of 60 degrees was used for copper. For both materials, the experimental data is collected at five-degree intervals of orientation angle (θ , measured from $[0\ 1\ 0]$ direction). Thus, the number of available experimental data points (N_d) is 72 for a 360 degree rotation about the zone axis.

Table 3.1 gives the resulting material parameters obtained from calibration. Figure 3.8 compares the experimental specific cutting energy with the specific cutting energy obtained from the model using the calibrated material constants. It is seen that the calibration scheme successfully determined the material parameters to be used in the RSPM model.

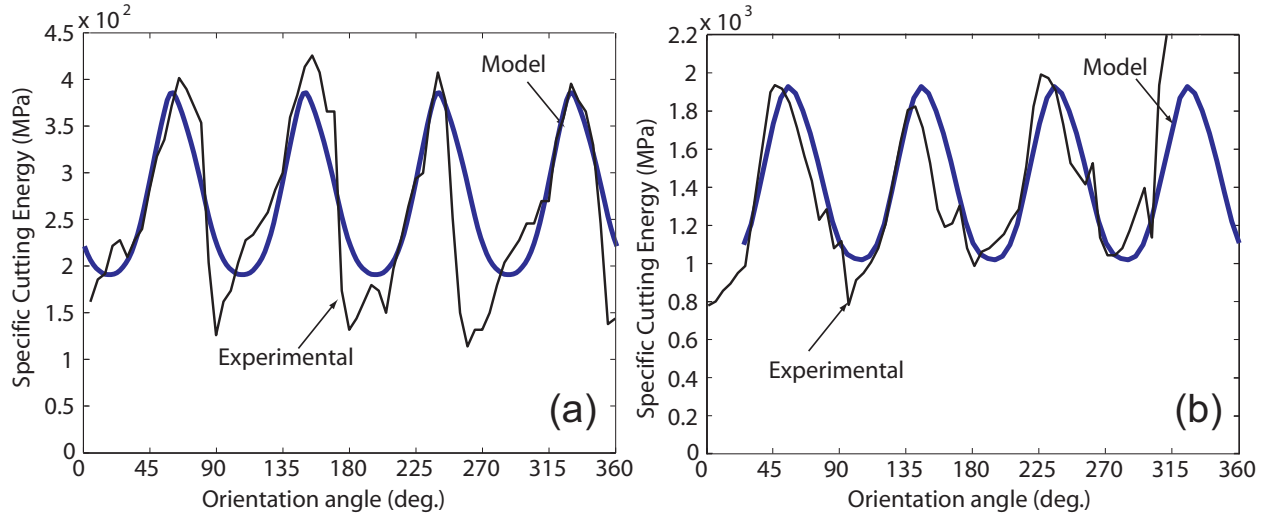


Figure 3.8: Comparison of experimental and predicted specific cutting energy for (a) aluminum and (b) copper for the calibration cases.

3.5.3 Selection of the incremental strain value

When calculating the plastic power, the value of the incremental strain $\Delta\gamma$ must be chosen, such that $N_s\Delta\gamma = \gamma$ (see Eq. (3.11)). The incremental strain must be chosen sufficiently small to ensure the accuracy of the results. However, if the value is too small, it would induce undue computational burden during the simulation of the model. To identify the incremental strain value that can strike

a balance between the accuracy and numerical efficiency of the model, a convergence study is performed in this section.

Figure 3.9(a) shows the typical variation of plastic power \dot{W}_p for decreasing values of incremental strain $\Delta\gamma$ (or increasing values of $(\Delta\gamma)^{-1}$). The material parameters of aluminum used for obtaining Fig. 3.9 are given in Table 3.1. As seen in the figure, the value of plastic power reaches a plateau (limiting value) with decreasing $\Delta\gamma$. Figure 3.9(b) shows percentage difference between the calculated plastic power and the limiting value. It is seen that an incremental strain value of $\Delta\gamma = 0.003$ ensures that the plastic power is within 0.25% of the limiting value. Based on this observation, for the work presented below, an incremental strain value of $\Delta\gamma = 0.003$ is used. This choice of the incremental strain value is smaller than generally adopted in the computation of texture evolution, for which the concern is to capture lattice reorientation with sufficient accuracy [47].

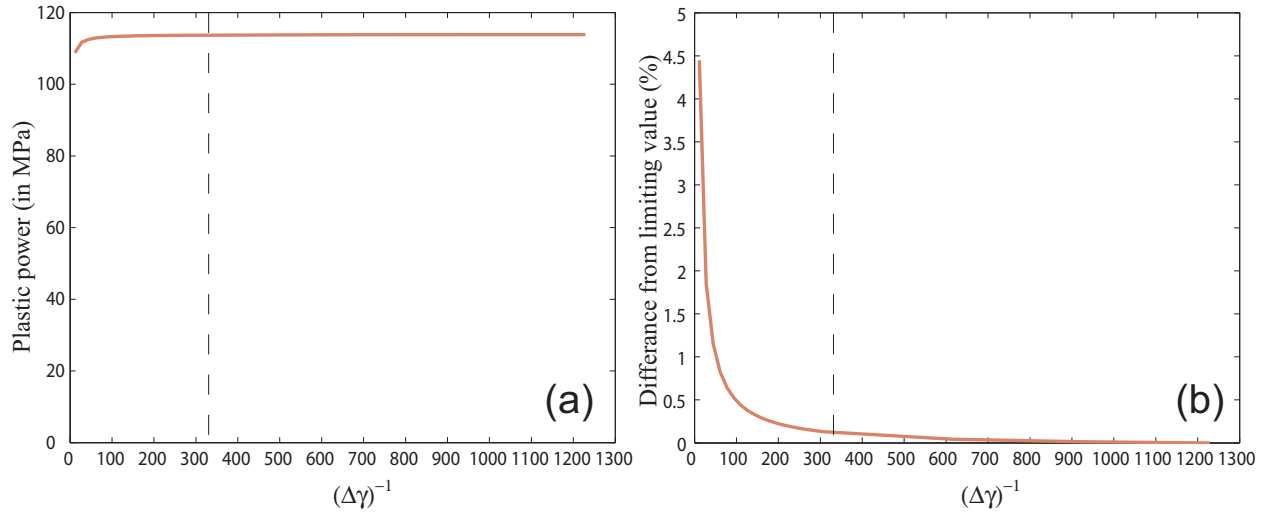


Figure 3.9: Choice of incremental strain $\Delta\gamma$ through convergence: (a) Variation of plastic power for cutting direction $[hkl] = [100]$, cutting plane normal $[uvw] = [010]$, and zone axis $[abc] = [001]$ (see Fig. 1.6(a)) (the candidate shear angle for the graph shown is 39 degrees); and (b) percentage variation from limiting value with decreasing $\Delta\gamma$. The selected $\Delta\gamma$ value is identified in the figures with dashed lines.

3.6 Validation of the model

The validation of the model is performed by comparing the specific energies from the model with those from plunge-turning experiments on single-crystal aluminum [19]. For this comparison, the calibrated material parameters (provided in Table 3.1) are used for the model. The validation data

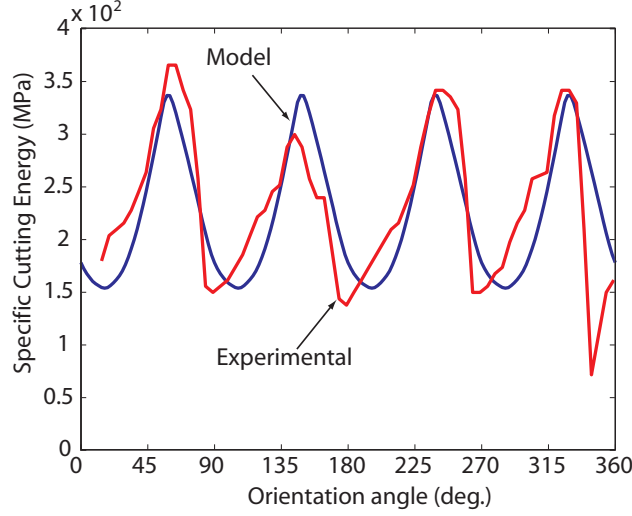


Figure 3.10: Validation case: comparison of the specific energies from the model and from experiments for single-crystal aluminum for the zone axis of $[0\ 0\ 1]$.

was collected at a cutting velocity of 0.44 mm/s, an uncut chip thickness of 0.11 mm, cutting width of 1.43 mm, and a rake angle 50 degrees [19]. The average friction angle was estimated to be 57 degrees. The zone axis ($[abc]$ in Fig. 3.6(b)) of the machined crystal was $[0\ 0\ 1]$, and the orientation angle was measured from $[0\ 1\ 0]$ direction.

The comparison between the predicted and the experimental data for validation is given in Fig. 3.10. It is seen that the model is able to capture the crystallographic symmetry about the $[001]$ zone axis. More importantly, both the relative magnitude and the trend of specific energy calculated from the model follow closely those from the experiment. As outlined below, unlike the simplified model presented in [45], the RSPM model was able to capture successfully the phase angle (the location of the peaks) of the specific energies with the orientation angle.

3.7 Model Analysis

This section presents an in-depth analysis of the model, including the effects of lattice rotation and hardening, and the sensitivity of model response to variations in material properties.

3.7.1 Lattice rotation and hardening

The main difference between the machining force models in [38,45,48] and the RSPM model is that the latter includes the lattice rotation and hardening effects through rate-sensitive constitutive

equations. In this section, lattice rotation and hardening are analyzed individually to observe their contribution to the specific energies. For this purpose, the specific cutting energies obtained from the RSPM model are compared to simplified versions of the model, which are obtained by removing either or both of the lattice rotation and hardening effects. The comparisons are made for two different zone axes with different symmetries ($[1\ 0\ 1]$ with two-fold symmetry and $[0\ 0\ 1]$ with four-fold symmetry). The rake angle and friction angle are fixed at 40 degrees and 50 degrees, respectively. The calibrated material properties of aluminum are used in arriving at the results. When the hardening effect is neglected for the simplified models, the critical resolved shear stress (for the simplified models) is selected such that the mean values of specific energy (for a given zone axis) of the RSPM model match that of the simplified model. For each zone axis, the specific energies, as they vary with the cutting plane orientation, are compared based on the overall shape (trend), amplitude, orientation (phase) angle of the peak specific energies, and symmetry (i.e., the periodicity of the data with the crystal orientation angle).

Figures 3.11(a) and 3.11(b) compare the RSPM model with the simplified version of the model, which neglects both hardening and lattice rotation (but utilizes rate-sensitive constitutive equations for obtaining stress and consequently power values)². While the amplitude of the specific energy from both the models is similar for $[0\ 0\ 1]$ and $[1\ 0\ 1]$ zone axes, the simplified version fails to capture the overall shape and the two-fold symmetry about $[1\ 0\ 1]$ zone axes. Furthermore, in both zone axes, the simplified model cannot capture the orientation (phase) angle of the peak specific energy. Therefore, while the simplified version of the model without the hardening and lattice rotation effects is capable of approximating the variation of specific energy about the mean, it does not capture the detailed trend, symmetry, and the phase angle of the specific energies as they vary with the orientation angle.

To show the effect of hardening without lattice rotation, Figs. 3.11(c) and 3.11(d) compare the RSPM model with another simplified version of the model that neglects lattice rotation but includes hardening. Compared to the previous case (of no hardening or lattice rotation) there is a slight improvement in the the orientation angle of the peak specific energy. The amplitude of variation is overestimated considerably for the $[0\ 0\ 1]$ zone axis. The specific trend and symmetry are still not captured.

Another comparison outlines the effect of lattice rotation in the absence of the hardening effect. Figures 3.11(e) and 3.11(f) compare the RSPM model with a simplified version of the model that

²The simplified version closely mimics the behavior of results from force model in [45,48] (also shown in Fig.3.11(a) and 3.11(b)). The small difference between the two stems from the rounding of the yield vertex when the rate-sensitive constitutive equations are used.

neglects hardening but includes lattice rotation. It is seen that the specific trend, symmetry, and the phase angle are now well-captured by the simplified model. The amplitude, however, is underestimated for both zone axes. The results from this no-hardening scenario match closely to that of current model in terms of overall shape for both zone axes. Similar to the current model, this scenario captures the symmetries about both zone axes. It can therefore be concluded that the specific trend, symmetry, and phase angle of the specific energies are mainly affected by the lattice rotation, whereas the amplitude of variation is determined by both hardening and lattice rotation.

Based on the observations from Figs. 3.11(a)-(f), it can be seen that the inclusion of lattice rotation is required for capturing the crystallographic symmetry, specific trend, and the phase angle (hardening has only a small effect in phase angle). However, both lattice rotation and hardening play a role in determining the amplitude of specific energies.

3.7.2 Effect of material properties

In this section, the sensitivity of the specific energy to variation in material properties is analyzed. For a given zone axis, variation of the material parameters (within a relatively wide range) has been observed to have only a little effect on the specific trend and the orientation (phase) angle of the peak specific energy. The mean value and the amplitude (of variation about the mean), on the other hand, have a stronger dependence on the material parameters. Therefore, to simplify the sensitivity analysis, the specific energy signature is represented by the mean value (M) and the peak-to-valley amplitude (Ω) as shown in Fig. 3.12. The effect of variation of material parameters on the mean value and amplitude are studied for both aluminum and copper. In both cases, the rake angle and zone axis are fixed at 40 degrees and $[0\ 0\ 1]$ direction, respectively. Considering the experimentally observed difference between the friction angles for copper and aluminum [19], a friction angle of 50 degrees for aluminum and 60 degrees for copper is selected. For each material, one parameter is varied at a time, keeping the others equal to the calibrated values. The chosen analysis range for each material parameter represents $\pm 50\%$ variation of that parameter about the calibrated value.

Figures 3.13 and 3.14 shows the change in mean value and magnitude of specific energies with changing material parameters for aluminum and copper, respectively. The five material parameters, including the initial hardening slope Θ_o , the saturation stress τ_v , the initial reference stress τ_o , the exponent of the power law a , and the exponent of rate sensitivity n are analyzed. It is observed that, although the actual values of the mean and amplitude are different for aluminum and copper,

the specific energy for both materials vary similarly with varying material parameters. In both cases, the mean value and amplitude increase with increasing values of the reference stress (τ_o), saturation stress (τ_v), initial hardening slope (Θ_o), and decrease with increasing exponent of the power law (a).

To explain the observed behavior, the deformation (slip) behavior must be considered. The similarity of the results for aluminum and copper indicates that the deformation kinematics—which depend on the arrangement of the slip systems, and thus, are identical for all fcc metals—play a major role in determining the specific energy signatures. Therefore, the cumulative slip, i.e., the total slip that occurs in all active slip systems for a given state of deformation, must be analyzed.

As seen from Eq. (3.41), the total power is proportional to the plastic power, which depends on the cumulative slip. The cumulative slip can be calculated as

$$\gamma_t = \sum_{s=1}^{12} \gamma_s, \quad \text{where} \quad \gamma_s \approx \sum_{k=1}^{N_s} |\dot{\gamma}_s^k| \Delta t, \quad (3.40)$$

Here, γ_s represents the absolute value of slip on the s^{th} slip system. Figure 3.15 indicates that the change in specific energy closely follows that in cumulative slip. The small difference between the specific energy and cumulative slip variations arises from the variation of shear angle.

Recognizing the effect of cumulative slip, the material model with hardening (i.e., the variation of reference stress with cumulative slip) is used to describe the observed phenomena. Figure 3.16(a) shows the material model, and defines the initial reference stress τ_o , the saturation stress τ_v , and the initial hardening slope θ_o . Two different levels of cumulative stress γ_c^1 and γ_c^1 are also shown in the figure. The actual shape of the material model is controlled by the exponent of the power law a and the initial hardening slope. To obtain the plastic work for a given level of cumulative slip γ_c^i , the reference stress is integrated from $\gamma_c = 0$ to $\gamma_c = \gamma_c^i$, which gives the area under the curve up to γ_c^i .

Figures 3.16(b)-(e) show the effect of the initial reference stress, the saturation stress, the initial hardening slope, and the exponent of the power law on the material behavior, where the arrows indicate change in reference stress curve with the *increase* in given parameter. It is seen that the area under the curve for a given level of cumulative slip (e.g., γ_c^1)—and thus the plastic work for *any* orientation angle—increases with increasing initial reference stress, saturation stress, or the initial hardening slope. Thus, the mean value M of the specific energy is expected to be positively correlated to τ_o , τ_v , and θ_o , which explains the behavior observed in Figs. 3.13(b)-(d)

and Figs. 3.14(b)-(d). Increasing the exponent of the power law (a) decreases the area under the reference stress for *any* given cumulative slip (see Eq. (3.34)). Consequently, an increase in a yields a reduction in specific energy, as observed in Figs. 3.13(a) and 3.14(a).

Since Ω represents the difference between maximum and minimum specific cutting energy, its behavior follows the area under the curve between respective cumulative slips, e.g., γ_c^1 and γ_c^2 , resulting in those specific energies (with $\gamma_c^1 > \gamma_c^2$). Since the area between γ_c^1 and γ_c^2 increases with increasing τ_o , τ_v and Θ_o and decreases with increasing a , the observed behavior of Ω with material parameters is similar to that of the mean, as observed in Figs. 3.13(f)-(i) and Figs. 3.14(f)-(i).

Lastly, it is observed that the exponent of rate sensitivity n has the smallest effect on the mean value and the amplitude for both materials. Since the exponent causes the yield vertices to round-off, changing its value results in changing the radius of rounding-off. Beyond a sufficiently large value of n , the rounding-off radius is very small, and hence the stress solutions obtained from solving Eq. (3.29) are quite similar for different values of n . As a result, the plastic work, and consequently specific energies, do not vary significantly with the exponent of the rate sensitivity, as observed in Figs. 3.13(e) and 3.13(j) and Figs. 3.14(e) and 3.14(j).

3.8 Model application

The main purpose of developing a machining force model is to predict the specific energies under varying input conditions encountered during machining. To demonstrate the application of the model for prediction, specific energies are analyzed for different crystallographic orientation, rake angle, and friction angle. Since the uncut chip thickness, cutting velocity and width of cut do not affect the specific cutting energy within the framework of the current model, these input parameters are not considered in this analysis. Based on the discussion above that all fcc materials are expected to behave similarly, the analysis is only performed for aluminum, using the calibrated material properties given in Table 3.1. Furthermore, since the thrust and cutting specific energies can be directly related (see Fig. 3.21), only cutting specific energies are analyzed, and the thrust specific energy can be calculated from $u_t = u_c \tan(\beta - \alpha)$.

3.8.1 Effect of the zone axis

To analyze the effect of the crystallographic orientation of the sample zone axis ($[abc]$ in Fig. 3.6(b)) the specific cutting energy is calculated for eight different zone axis, including $[0\ 0\ 1]$, $[1\ 1\ 1]$, $[1\ 1\ 0]$, $[1\ 0\ 1]$, $[1\ 0\ 0]$, $[0\ 1\ 1]$, $[0\ 1\ 0]$, and $[0\ 0\ 1]$.

0 1], [1 1 2], [2 1 2], [2 1 3], [2 1 6] and [1 0 2]. For each zone axis, the orientation angle (which corresponds to cutting plane orientation $[uvw]$ in Fig. 3.6(b)) is varied from 0 to 360 degrees, starting from a reference orientation angle according to Fig. 3.17, the zone axes are chosen such that they are uniformly distributed over the basic stereographic triangle, thereby uniformly distributing the analyzed zone axes within all possible orientations. For this analysis, a rake angle of 40 degrees and friction angle of 50 degrees are used³.

³The orientation angles about [0 0 1], [1 1 1], [1 0 1], [1 1 2], [2 1 2], [2 1 3], [2 1 6] and [1 0 2] zone axes were measured clockwise from [0 1 0], [1 1 -2], [0 1 0], [-1 1 0], [-1 0 1], [-1 -1 1], [1 4 -1] and [0 1 0] directions, respectively

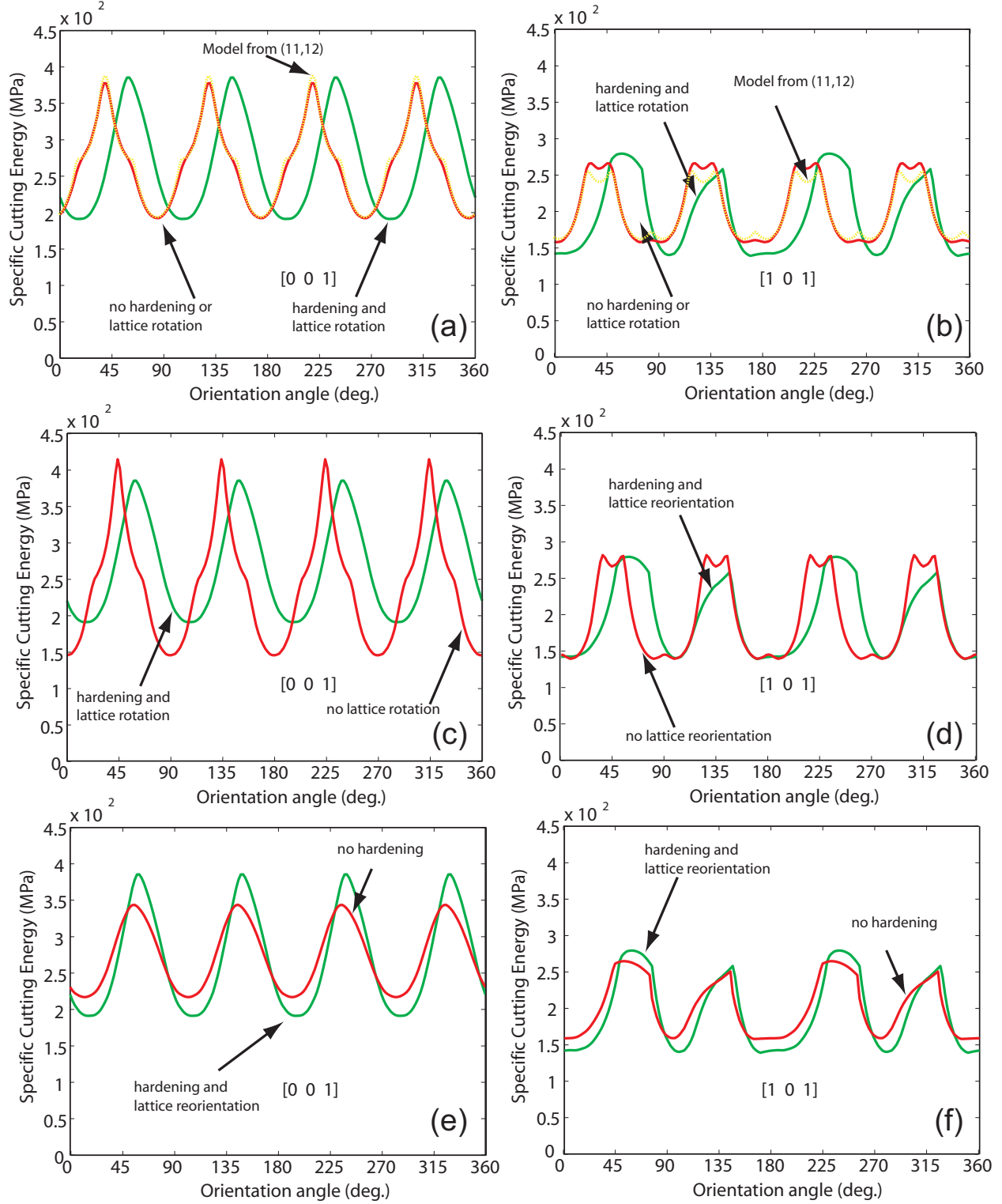


Figure 3.11: The effects of hardening and lattice rotation on specific energy: (a) and (b) no hardening and no lattice rotation; (c) and (d) hardening without lattice rotation; (d) and (f) lattice rotation without hardening cases. The former of each pair is for [0 0 1] zone axis, and the latter is for [1 0 1] zone axis. The full RSPM model (hardening and lattice rotation) is used as the reference for each case.

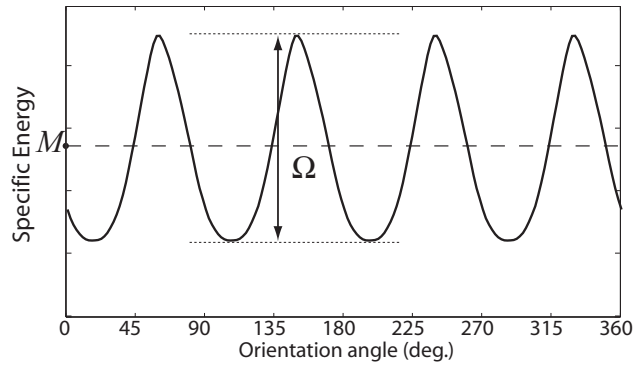


Figure 3.12: Definition of the metrics used for analyzing the effect of different parameters: M is the mean value, and Ω is the amplitude (about the mean) of the specific energy as it varies with the orientation angle.

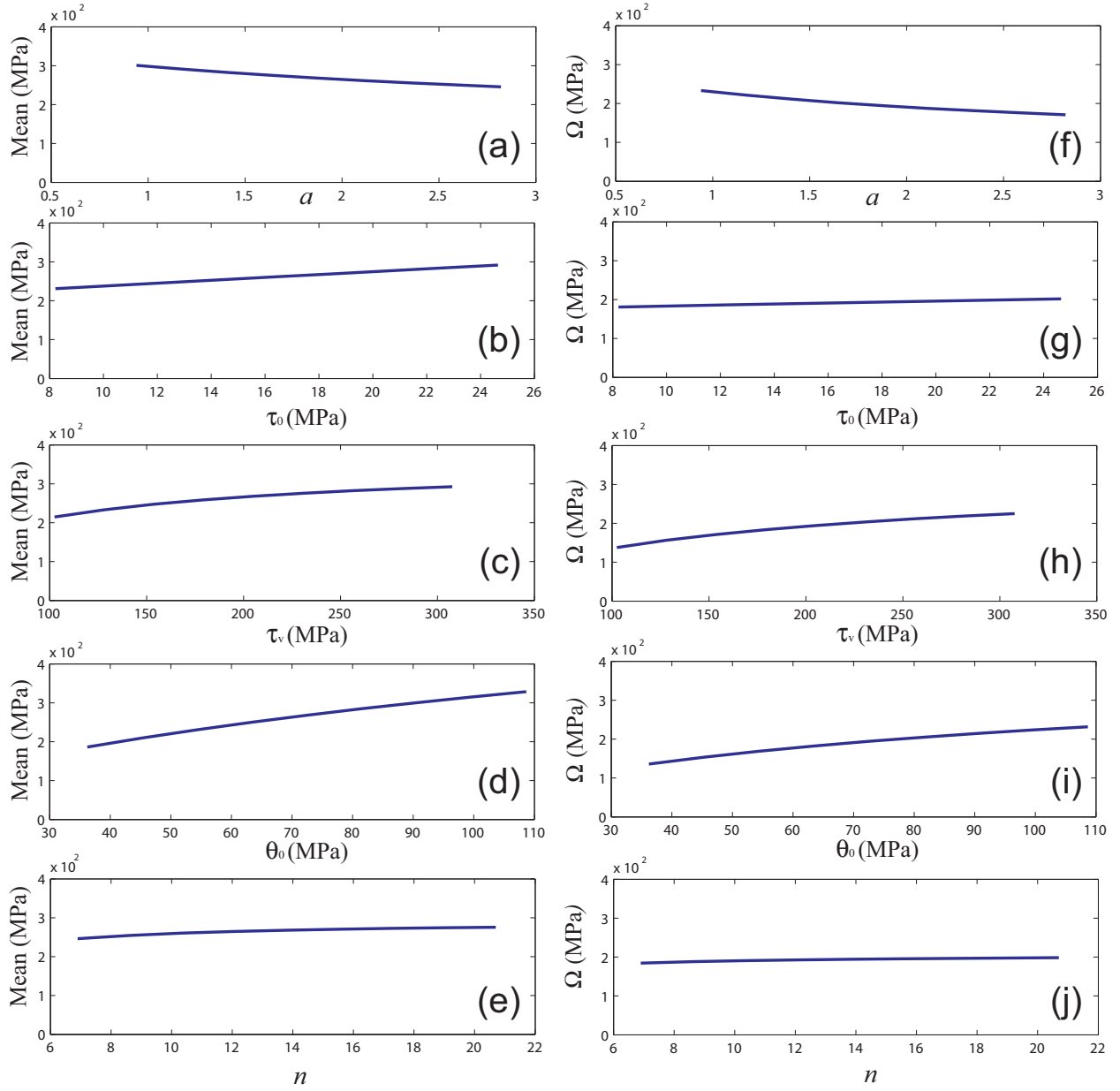


Figure 3.13: Effect of material parameters on mean M and amplitude Ω of specific energies for *aluminum*: (a)-(f) The exponent of the power law a ; (b)-(g) the initial reference stress τ_0 ; (c)-(h) the saturation stress τ_v ; (d)-(i) the initial hardening slope Θ_0 ; and (e)-(j) the exponent of rate sensitivity n .

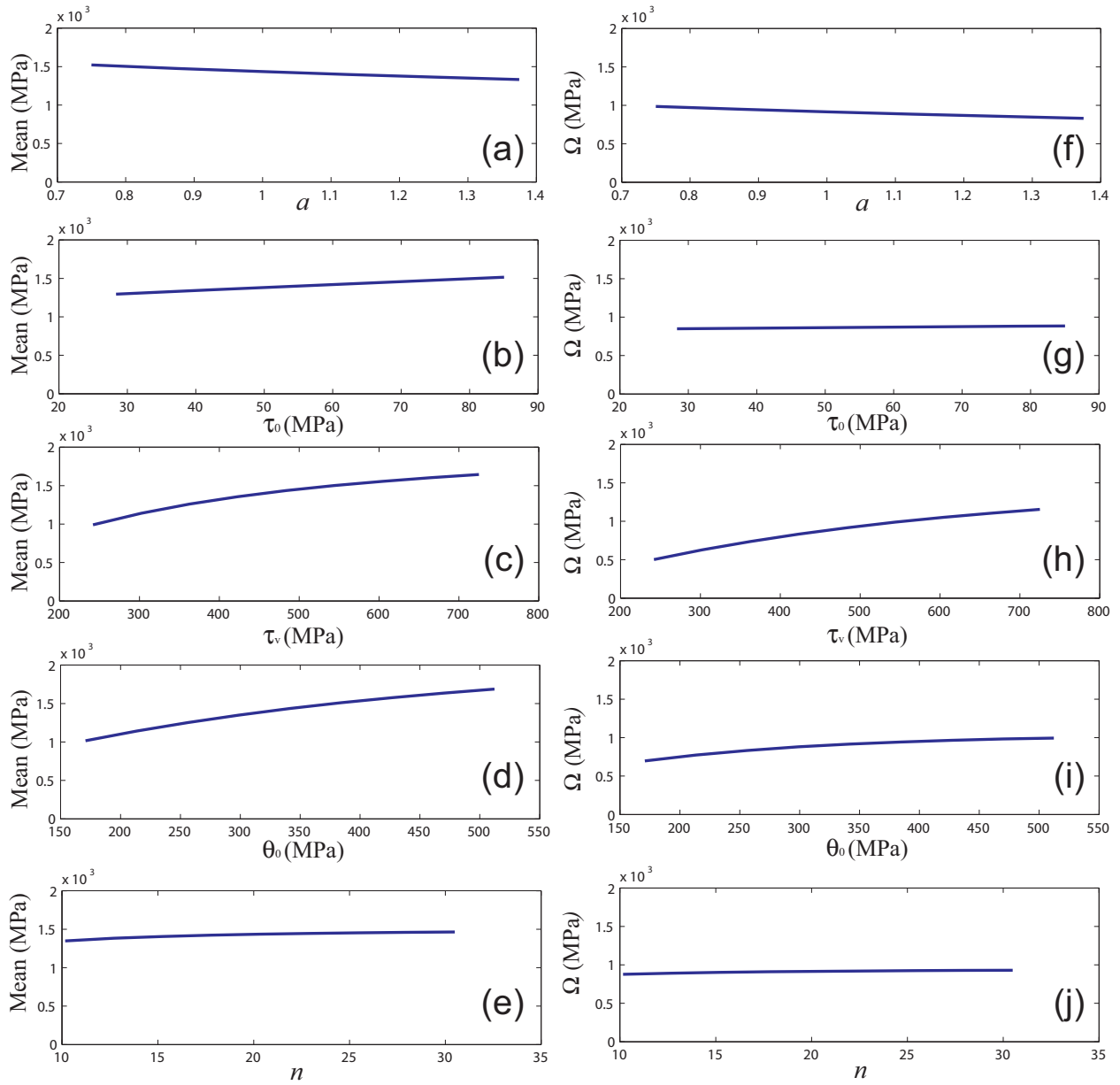


Figure 3.14: Effect of material parameters on mean M and amplitude Ω of specific energies for *copper*: (a)-(f) The exponent of the power law a ; (b)-(g) the initial reference stress τ_0 ; (c)-(h) the saturation stress τ_v ; (d)-(i) the initial hardening slope Θ_0 ; and (e)-(j) the exponent of rate sensitivity n .

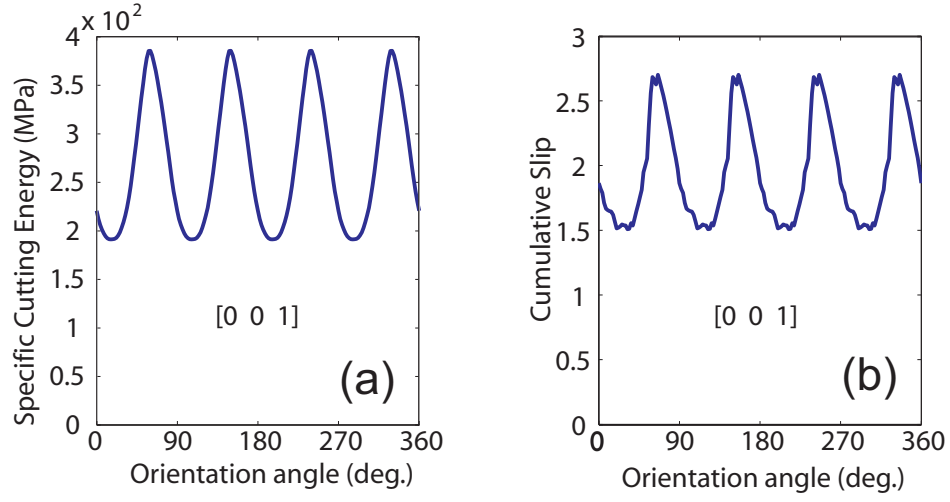


Figure 3.15: Comparison between the (a) variation of the specific energy and (b) variation of the cumulative slip about $[0\ 0\ 1]$ axis for aluminum ($\alpha = 40$ deg. and $\beta = 50$ deg.).

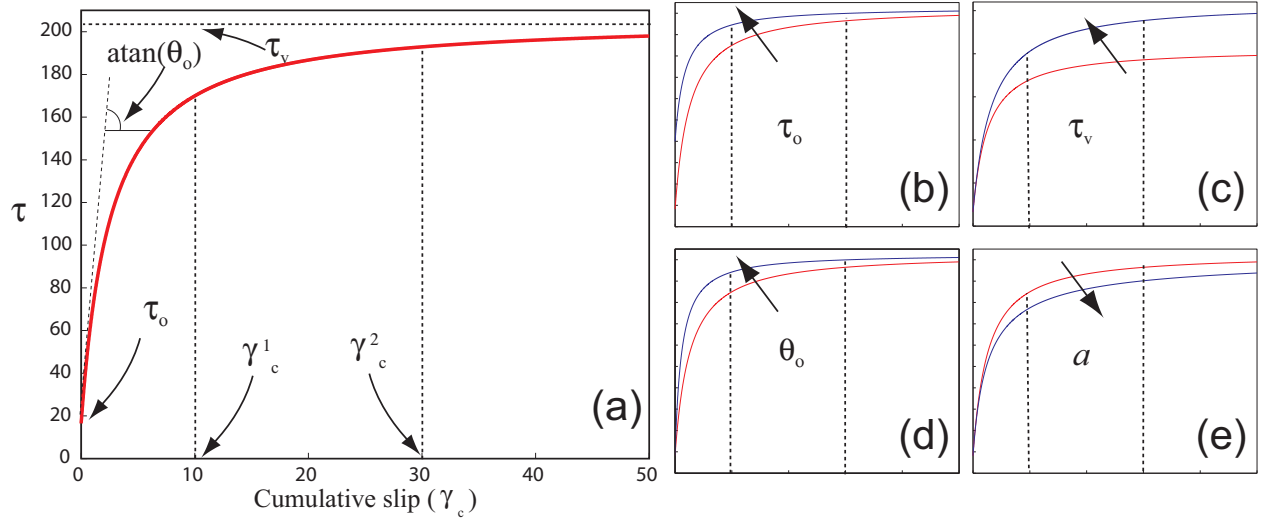


Figure 3.16: (a) The material model (plastic stress versus cumulative slip) with the hardening effect; and the effects of (b) the initial reference stress, (c) the saturation stress, (d) the initial hardening slope, and (e) the exponent of the power law on the material model.

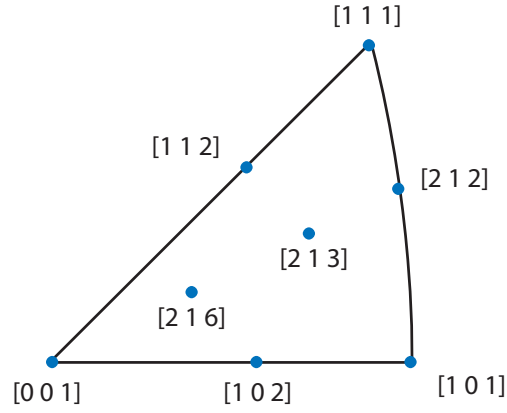


Figure 3.17: The selected zone axes in the basic stereographic triangle.

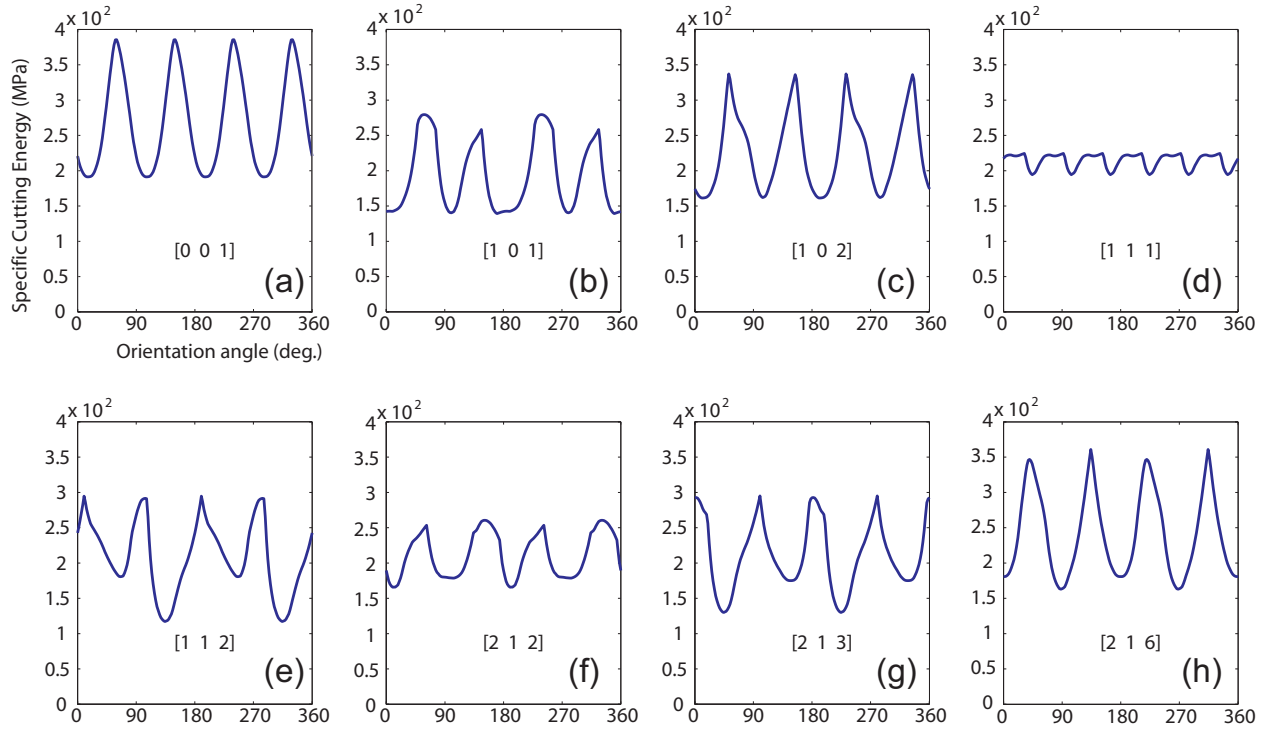


Figure 3.18: The effect of zone axis on specific cutting energy for aluminum for zone axes (a) $[0\ 0\ 1]$, (b) $[1\ 0\ 1]$, (c) $[1\ 0\ 2]$, (d) $[1\ 1\ 1]$, (e) $[1\ 1\ 2]$, (f) $[2\ 1\ 2]$, (g) $[2\ 1\ 3]$, and (h) $[2\ 1\ 6]$.

The specific cutting energies for the selected zone axes are shown in Fig. 3.18. The specific energy signatures show 2, 4, and 6-fold symmetries based on the crystal structure about the chosen zone axes, e.g., $[1\ 0\ 1]$ has a 2-fold symmetry and $[1\ 1\ 1]$ has a 6-fold symmetry. The deformation mechanics can be analyzed to facilitate further interpretation of the results.

As discussed above, the specific energies closely follows the associated cumulative slip required to accommodate the deformation. The amount of slip, in turn, is determined by the *proximity* of slip systems to the shear plane during deformation. Here, the term “proximity” indicates how favorably a slip system is oriented with respect to the shear plane, so that it can accommodate the deformation. Although the existence of lattice rotations prevents providing a generalized quantitative description of the proximity (e.g., by using Schmid’s analysis) between shear plane and slip plane/direction, a qualitative analysis of specific energy signatures can be performed based on the notion of proximity. For instance, it is expected that the lowest specific energy can be obtained at a zone axis that would allow the shear plane to be a slip plane, and the shear direction to be a slip direction associated with the slip plane. For such a scenario to occur, the slip plane must coincide with the shear plane, and the slip direction must be aligned with the shear direction. This indicates that both slip plane normal and the slip direction must be perpendicular to the zone axis. It can be verified that such a zone axis must belong to $\langle 112 \rangle$ family of directions. Hence, the minimum specific cutting energy value must occur at some orientation angle about $[1\ 1\ 2]$ zone axis. Figure 3.18 shows that the minimum specific energy occurs about $[1\ 1\ 2]$ zone axis, close to the orientation angles of 135 and 215 degrees (at which $[-1\ 1\ 0]$ direction becomes aligned along the shear direction). Indeed, without the lattice rotation and hardening effects, the minimum would have occurred exactly at 135 and 215 degrees.

The effect of zone axis can be analyzed more broadly based on the mean value M and amplitude of variation. The latter may be presented as a ratio of the mean as $\Delta = \Omega/M$, referred to here as the *deviation*, to facilitate meaningful comparisons across zone axes. Figures 3.19(a) and (b) provide the variations of mean value and deviation at different zone axes, calculated at 40 orientations across the basic stereographic triangle (crystallographic orientations). Associated average cumulative slip and average lattice rotation are given in Figs. 3.20(a)-(b). It is seen that the $[0\ 0\ 1]$ and $[1\ 0\ 1]$ zone axes result in the highest and the lowest mean specific cutting energy, respectively. A comparison of Figs. 3.19(a) and 3.20(a) indicates that the mean specific energy follows the cumulative slip. The cumulative slip increases with increasing number of slip systems required for accommodating the deformation. Thus, higher mean values are observed for those zone axes that necessitate a higher number of slip systems for accommodating the deformation. For $[0\ 0\ 1]$ zone axis, *at least* 4 active

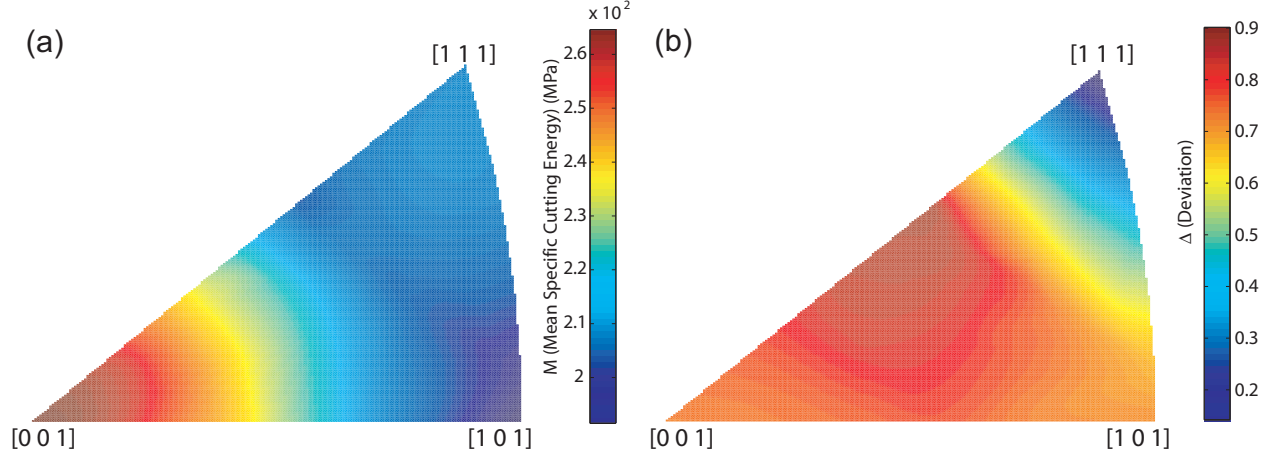


Figure 3.19: The effect of zone axis on (a) the mean and (b) the deviation of specific cutting energy for aluminum (*color online*).

slip systems are required to accommodate deformation for most of the orientation angles, whereas for $[1\ 0\ 1]$ zone axis, *at most* 4 active slip systems are sufficient (the majority of orientation angles requiring only two active slip systems). Thus, the mean specific energies are expected to be higher for the $[0\ 0\ 1]$ zone axis.

The deviation arises from the difference in proximity of slip systems at different orientation angles about a given zone axis. The $[1\ 1\ 2]$ and $[1\ 1\ 1]$ zone axes result in the maximum and minimum deviation, respectively. For $[1\ 1\ 2]$ zone axis, the deformation in few of the orientation occur via single slip, resulting in lower values of specific energy. Other orientations, however, require up to five slip systems to be simultaneously activated, and thus causing high values of specific energy. Therefore, the deviation of specific cutting energy about the mean value is very large. On the other hand, the six-fold symmetry associated with the $[1\ 1\ 1]$ zone axis yields the smallest value of deviation.

The effect of zone axis on the average value of lattice rotation (measured about the respective zone axis) is given in Fig. 3.20(b). Due to the plane strain nature of deformation, the zone axis is the axis of rotation. It is seen that the average lattice rotation closely follows the associated cumulative slip. This is due to the fact that higher cumulative slip induced a higher level of lattice rotation.

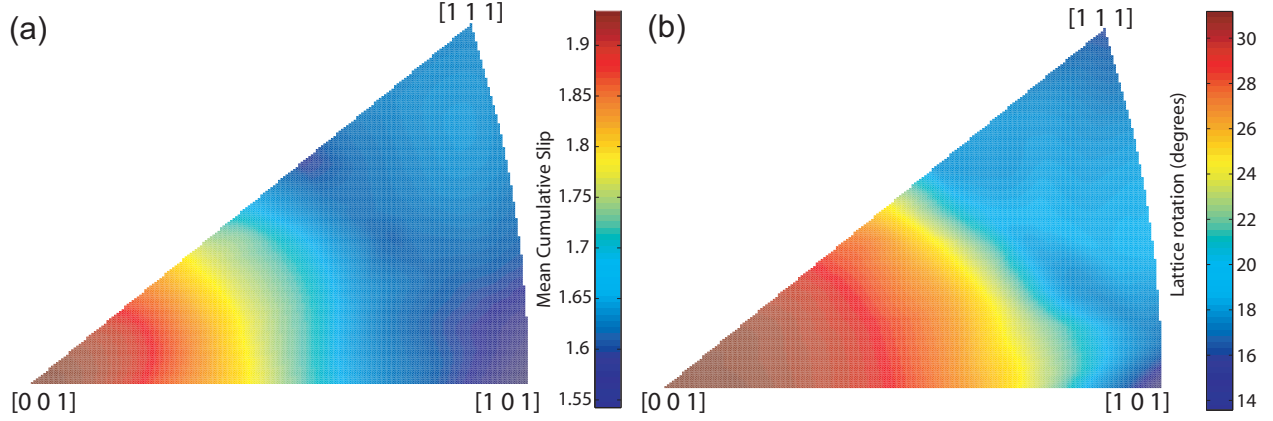


Figure 3.20: The effect of zone axis on (a) the average cumulative slip and (b) the average lattice rotation for aluminum (*color online*).

3.8.2 Effect of rake and friction angles

The rake angle (α , see Fig. 3.21) and the coefficient of friction (or the friction angle β) on rake face affect the machining forces and specific energies. Model Analysis section showed that the shape of specific energy signatures is determined by the arrangement of slip system with respect to machining geometry. Hence, the overall shape and phase angle of the specific energy curves do not vary significantly with the rake and friction angles, whereas the mean value M and amplitude Ω do. Unlike the simplified model presented in [45,48], in which the specific energy was dependent on only the value of $(\beta - \alpha)$, in the RSPM model, due to the inclusion of hardening and lattice rotation, α and β also have independent effects. Therefore, the analysis should be conducted in a two-dimensional variable space of α and β .

Figure 3.22 shows the variation of mean value and amplitude of specific cutting energy with rake and friction angles. At any value of rake angle the choice of friction angle is restricted by $(\beta - \alpha > 0)$ to avoid the possibility of negative and zero thrust forces. For the analysis presented here, the minimum value of $(\beta - \alpha)$ is chosen to be 5 degrees. The effect of rake and friction angles on the proportion of plastic to total power and on the plastic power are analyzed in Figs. 3.23 (a) and (b), respectively.

At a fixed rake angle, the mean value of specific cutting energy increases with increasing friction angle (increasing coefficient of friction) due to the increased amount of work required for overcoming the friction. At a fixed friction angle, the mean decreases with increasing rake angle because of reduced amount of shear (consequently reduced plastic work). Figure 3.23(a) also indicates that the fraction of mean power spent in plastic deformation is mostly determined by the friction angle. For

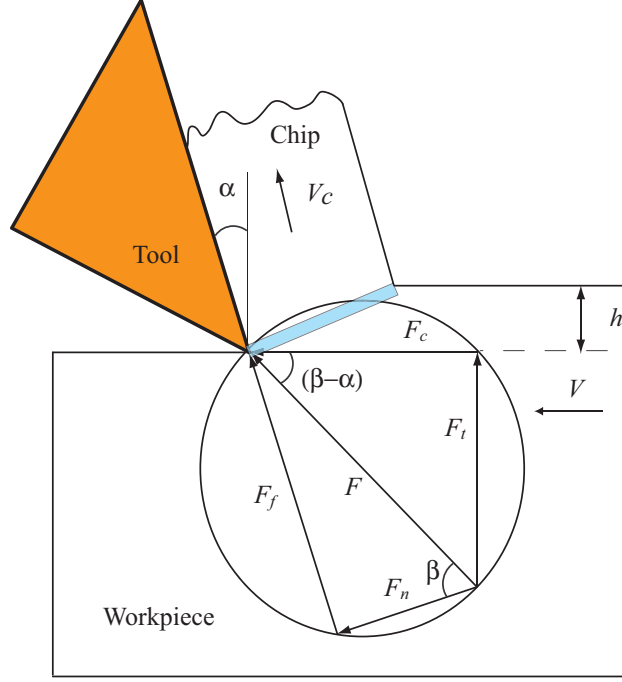


Figure 3.21: Orthogonal machining geometry.

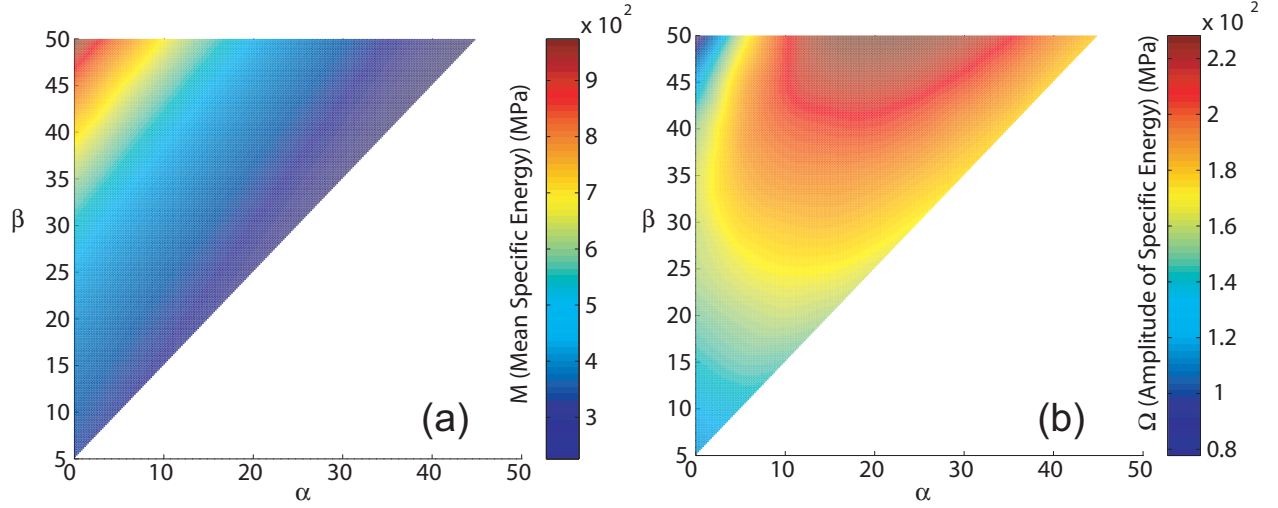


Figure 3.22: Variation of (a) the mean and (b) the amplitude with the rake and friction angles for aluminum (*color online*).

the Merchant model or for the anisotropy based simplified models in [45, 48], the fraction of power spent in plastic deformation is determined solely by the friction angle. In those cases contours of constant mean specific energy would lie along constant $(\beta - \alpha)$. A deviation from this behavior for the RSPM model is due to the incorporation of lattice rotation and hardening.

The effect of lattice rotation is strongly visible in Fig. 3.22(b) for the amplitude. For the range of values chosen, the amplitude is seen to peak around a rake angle of 20 degrees and a friction angle of 50 degrees (unlike the mean, which peaks at the highest $(\beta - \alpha)$ in the range). The position of the maximum amplitude is the result of the effect of lattice rotation. Although increasing values of specific energy at higher $(\beta - \alpha)$ tends to increase the absolute value of amplitude, the large deformations at higher $(\beta - \alpha)$ also results in large amount of lattice rotation. The resulting change in crystal orientation during machining causes the specific trend of specific energy signature to deviate from that shown in Fig. 3.8. For the $[0\ 0\ 1]$ zone axis considered, this change in the specific trend of the specific energy signature results in a reduction on the amplitude, thus shifting the position of peak from the highest $(\beta - \alpha)$.

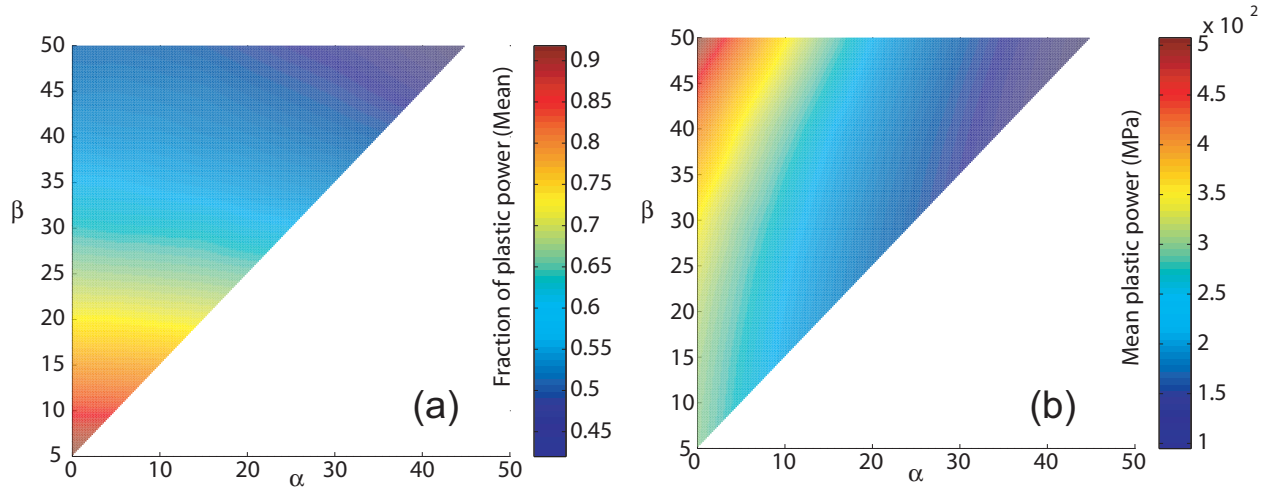


Figure 3.23: (a) The proportion of (average) power spent in plastic deformation (to total power) and (b) the actual power spent in plastic deformation for aluminum across the range of rake and friction angles (*color online*).

3.9 Simplification of the model using Merchant's shear angle

In [45], in the absence of lattice rotation and hardening effects, the Merchant's shear angle (ϕ_M) was seen to be similar to the shear angle values calculated from the simplified model. It was proven that Merchant's shear angle matches the shear angle found through minimization at maximum and minimum values of the specific cutting energy (as it varies with the orientation angle). Thus, although the use of Merchant's shear angle did not yield the exact trend of specific energy with orientation angle, it provided a close approximation to mean value and the amplitude of variation,

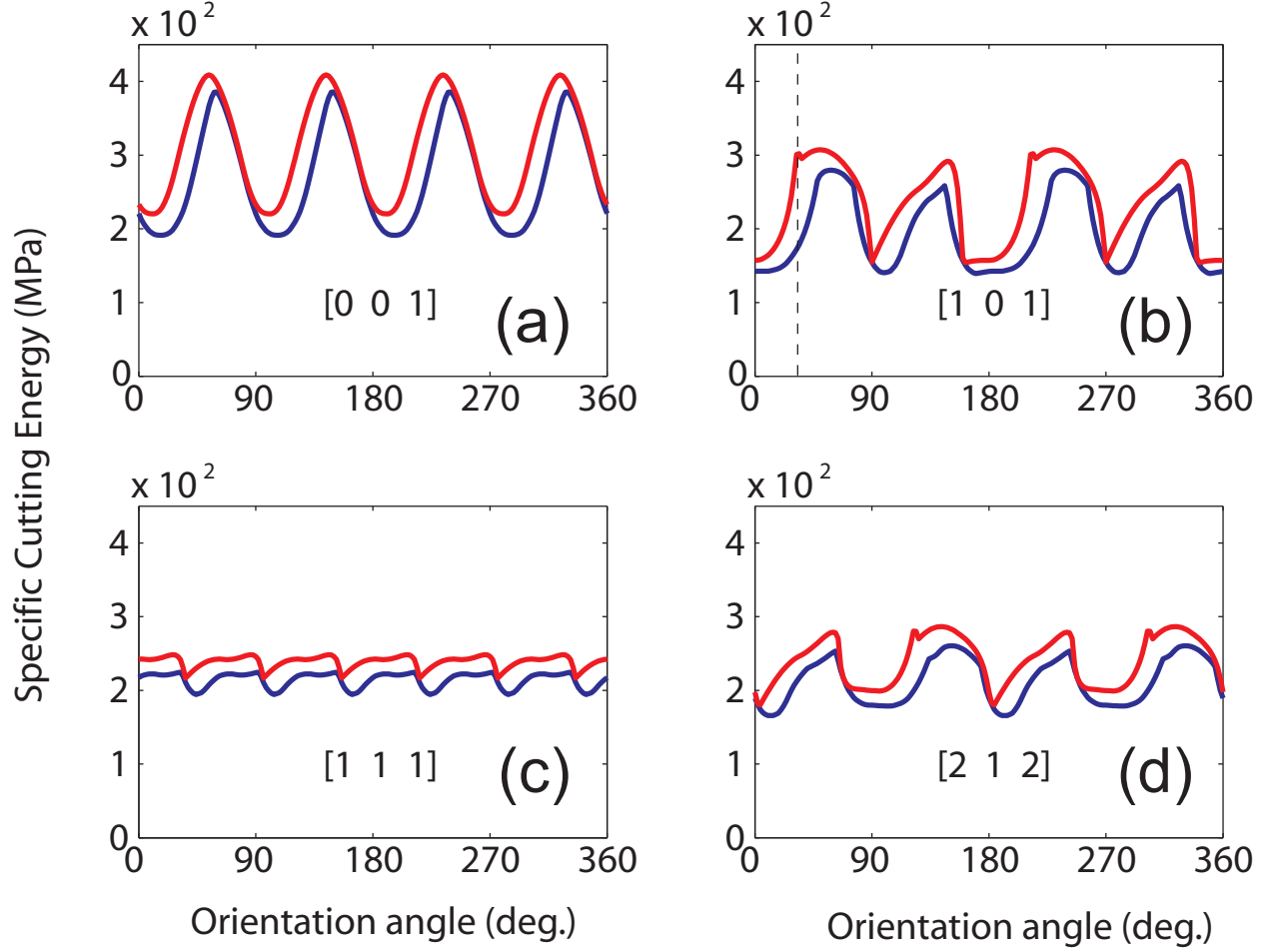


Figure 3.24: Comparison between the specific cutting energy obtained using Merchant's shear angle and that from the complete model including minimization of total work for (a) $[0\ 0\ 1]$, (b) $[1\ 0\ 1]$, (c) $[1\ 1\ 1]$, and (d) $[2\ 1\ 2]$ zone axes.

while reducing the computational burden by circumventing the need for power minimization to calculate the shear angle. Since such a simplification can potentially reduce the computation time significantly for the RSPM model, a similar analysis is performed for here.

To compare the specific energies from the complete RSPM model with that from the simplified RSPM model that uses the Merchant's shear angle, the rate-sensitive plastic work expression given in Eq. (3.7) can be written for Merchant's shear angle as

$$P_t = hwV W_p \left(1 - \frac{(\sin(\alpha) + \tan(\beta - \alpha) \cos(\alpha)) \sin(\phi_M)}{\cos(\phi_M - \alpha)} \right)^{-1}, \quad (3.41)$$

where

$$\phi_M = \frac{\pi}{4} - \frac{\beta - \alpha}{2}. \quad (3.42)$$

Figure 3.24 presents the results for the two cases for four zone axes, using calibrated material properties of aluminum, a 40-degree rake angle and a 50-degree friction angle. It is seen that the rate-sensitive model with Merchant's shear angle captures the trend in variation relatively well. As expected, since the complete RSPM model includes the minimization of total power over shear angle candidates, the specific energy obtained by using Merchant's shear angle is always greater than or equal to that of complete model. Therefore, it can be concluded that use of Merchant's shear angle within the RSPM model is sufficient to obtain the overall trend and amplitude (of variation) of the specific energy with crystallographic orientation. However, the phase angle and the mean value of the specific energies cannot be accurately determined using Merchant's shear angle formulation. Thus, large errors may result in specific energy predictions at certain orientation angles (e.g., a 80% error is seen around 30 deg. orientation angle when cutting $[1\ 0\ 1]$ zone axis.)

3.10 Summary

This chapter presented a machining force (specific energy) model for fcc single-crystal metals. The model uses the kinematics and geometry of orthogonal cutting process, and considers minimization of the total power, including the plastic power and friction power. The shear deformation is considered to occur in a finite shear zone. The *large* deformation is divided into a number of increments, the plastic work for each of which is determined using a rate-sensitive plasticity approach. Using the rate-sensitive approach enabled the active slip systems and amount of slip to be identified uniquely in each of those slip systems. For each incremental deformation, the lattice rotation and strain hardening (through an isotropic hardening scheme) are determined, and material properties are updated for the subsequent deformation increment. The friction power is calculated using an equivalent coefficient of friction between the chip and the tool rake face. Finally, the shear angle that results in the minimum total power (over geometrically-allowable shear angles) is identified as the shear angle solution for given cutting parameters (rake angle, cutting velocity, width of cut, uncut chip thickness, and coefficient of friction) and crystal orientation (workpiece zone axis, cutting plane orientation, and cutting direction). Using this shear angle, the cutting and thrust forces, and associated specific energies were calculated.

This model may be used to predict the variation of machining forces for given cutting parameters

and material properties (exponent of rate sensitivity, initial hardening slope, the saturation stress, the initial reference stress, and the exponent of the power law) for fcc single-crystal workpiece. Furthermore, if cutting occurs across multiple grains with different orientations, the RSPM model can be used to assess the force variations.

A Kriging-algorithm based calibration procedure was used to obtain the material parameters for the RSPM model from single-crystal cutting tests, and associated calibration parameters for copper and aluminum single crystals. Subsequently, a validation of the RSPM model was performed by comparing specific energies from model to experimental data from cutting tests on single-crystal aluminum. The effects of hardening and lattice rotation were then analyzed. Lastly, the model was applied to investigate the effect of sample zone axis, rake angle, and coefficient of friction on specific energies.

The following specific conclusions have been drawn from the presented analysis:

- The Kriging-based calibration procedure was seen to be effective in obtaining the five material parameters used in the RSPM model from single-crystal cutting data.
- The validation study showed that the RSPM model is able to capture accurately the variations of specific energies with the orientation angle (of the cutting plane) during orthogonal cutting of single-crystal fcc metals. The model captured the crystallographic symmetry, specific trend, mean value, amplitude (about the mean) and phase (of the peak) of the specific energy as it changes with the orientation angle.
- It was seen when both the lattice rotation and hardening effects (inclusion of either of which require rate-sensitivity) are neglected, although the amplitude of variation can be determined, the crystallographic symmetry, specific trend, and phase cannot be captured accurately. At a given orientation angle, this can cause considerable error on specific energy predictions. When hardening is included (without lattice rotation), the phase angle prediction improves slightly. However, the symmetry, specific trend, and phase angle still cannot be captured. When only the lattice rotation is included, all of the characteristics except the amplitude is captured accurately. Therefore, inclusion of the lattice rotation effect critical for capturing the crystallographic symmetry, specific trend, and phase angle of the specific energies as they vary with the orientation angle. Both the lattice rotation and hardening effects must be included to accurately determine the amplitude.
- The effect of material parameters on the crystallographic symmetry, specific trend, and phase angle are negligible. The amplitude and mean specific energies both increase with increasing

reference stress, saturation stress, and initial hardening slope; and both decrease with the exponent of (hardening) power law. The exponent of the rate sensitivity, on the other hand, only has a small effect on mean and amplitude of specific energies.

- It was observed that the behavior of mean and amplitude with material parameters is similar across different fcc materials, indicating that the deformation kinematics plays a major role in determining the specific energy signature. The change in specific energy values with crystallographic orientation was seen to follow closely the change in cumulative slip.
- At a fixed rake angle α , the mean value of specific cutting energy increased with increasing friction angle β (i.e., increasing coefficient of friction) due to the increased friction work. At a fixed friction angle, the mean decreases with increasing rake angle because of the reduced amount of shear (consequently, reduced plastic work). In the simplified model presented in [45,48], the mean specific energy was constant for constant $(\beta - \alpha)$ irrespective of the values of α or β . Due to the inclusion of lattice rotation and hardening, however, in the RSPM model the mean specific energy varies with not only their difference, but also individual values of α and β .
- A simplified version of the RSPM model is constructed by using the Merchant's shear angle instead of finding the shear angle through the minimization of total power. The simplified model was sufficient to obtain the overall trend and amplitude (of variation) of the specific energy with crystallographic orientation. However, the phase angle and the mean value of the specific energies were not accurately determined. As such, there may be large errors in specific energy prediction at certain orientation angles.

Chapter 4

Experimental Setups for Planing and Plunge-turning of Single Crystals and Coarse Grained Polycrystals

4.1 Motivation

The motivation for the experimental study on machining of coarse grained poly-crystals and single crystals is twofold: first, to understand the effects of anisotropy during micromachining; and second, to validate the machining force models developed earlier using the experimental machining data obtained from such studies.

The available experimental data on orthogonal machining in the presence of anisotropy was reviewed in Chapter 1. It was observed that studies in the literature can be divided into two categories, namely planing and plunge-turning, each with its own advantages and disadvantages. The available experimental data was focussed on primarily the machining forces. Since forces dictate surface finish it was naturally preferred to characterize machining behavior.

Although both planing and plunge-turning studies suggest a strong effect of crystallographic anisotropy on machining forces, the available data is insufficient to elaborate on the effects of rake angle, cutting velocity and uncut chip thickness in the presence of anisotropy. Furthermore, the available data is scattered sparsely over the possible cutting conditions, posing a difficulty for validating the machining models, i.e., a single study does not provide sufficient information for comparing with the models and due to the nature of machining experiments, which depend upon

the tool condition (edge sharpness ¹), and possibly machine stiffness [35], it is difficult to evaluate a model by comparing it across data from different studies.

This indicates a strong need for experimental data on machining of single-crystal and coarse-grained materials covering a broad range of machining conditions. Although planing experiments allow easier setups and provide access to more detailed data and visual inspections, they can be applied to only one (cutting) crystal orientation at a time. Alternatively, plunge turning experiments allow capturing the variation in machining response over a range of orientations, and enable wider ranges of cutting speeds to be used. To address these complementary capabilities, a planing apparatus and a plunge-turning apparatus are constructed.

4.2 Planing apparatus

A heavy duty sliding microtome was modified to create an orthogonal planing set-up as shown in Fig. 5.1. The microtome consists of a vertical stage with 1 μm resolution, and a horizontal slide capable of moving at velocities ranging from 1 mm/s to 100 mm/s. A tool post was constructed on the vertical stage as shown in Fig. 5.1. The tool is attached to the tool post (and stage) through a tool holder. The motion of stage along the feed direction specified the uncut chip thickness. The workpiece was attached to the horizontal slide, which provided the cutting velocity. The setup is equipped with a Kistler 9256C1 dynamometer fixed between the tool holder and the tool post for measuring the three orthogonal machining force components (see Fig. 5.1).

The tool post was designed to ensure high loop stiffness in order to avoid large variation of the uncut chip thickness from the prescribed value. A set of preliminary tests was conducted to verify that the variation is indeed minimal. To achieve this, a piece of aluminum (see Fig. 5.2) was machined at few prescribed uncut chip thicknesses and the thrust forces (along the feed direction in Fig. 5.1) were recorded. In between each cut, a replica of the wall was created (see Fig. 5.2) using a replica-set system. The replicas, which are channels, were measured for their depth using a white-light interferometer (WYKO). The difference in depth values between the replica from before and after the cut was considered as the actual uncut chip thickness. The results (see Table 5.1) show that irrespective of the thrust force, the difference between the measured and prescribed uncut chip thickness is within 1 μm .

¹While many of the cited studies do not provide edge radius of the tool, the available values vary from 10 nm [24] to 7 μm [31]

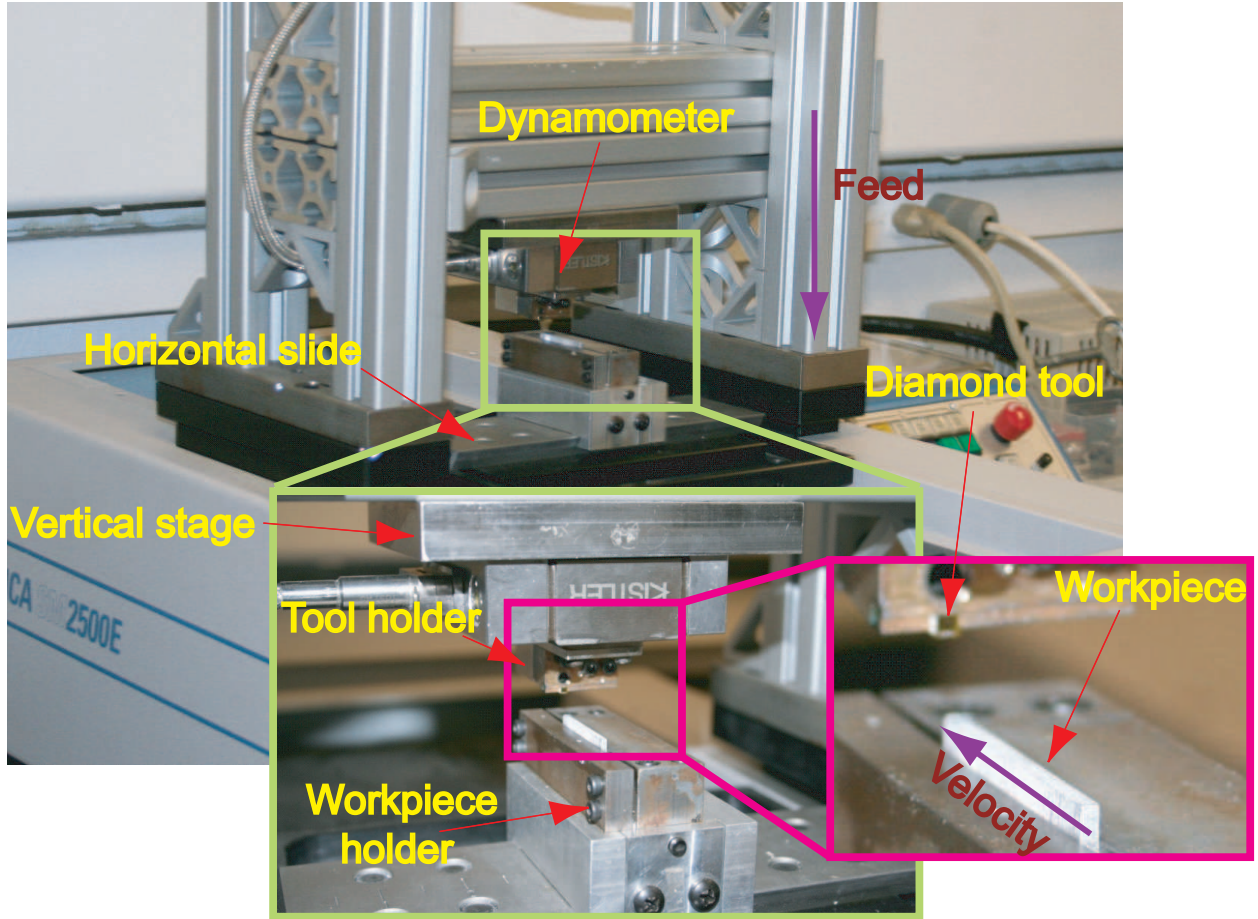


Figure 4.1: Planing apparatus.

4.2.1 Tool characterization

To minimize the complexities arising from non-sharp tools, especially while machining at the micro-scale, a custom made single crystal diamond tool was utilized for the experiments. The edge length of the tool was designed to be 2.5 mm. The tool geometry, shown in Fig. 4.3, was designed with an included angle of 60 degrees. This allowed the rake angle of the tool to be varied between 0-25 degrees using different tool holders as shown in Fig. 4.3, while maintaining a clearance angle of at least 5 degrees. In addition to holders for adjusting the rake angle, holders were also made for adjusting the inclination angle. Providing an inclination angle enables the tool to be used for oblique machining. The edge radius of the tool was measured at eight locations along the edge with an atomic force microscope using the technique similar to the ones described in [54–57]. The measured edge radius was found to be equal to $150.18 \text{ nm} \pm 20.26 \text{ nm}$ along the cutting edge.

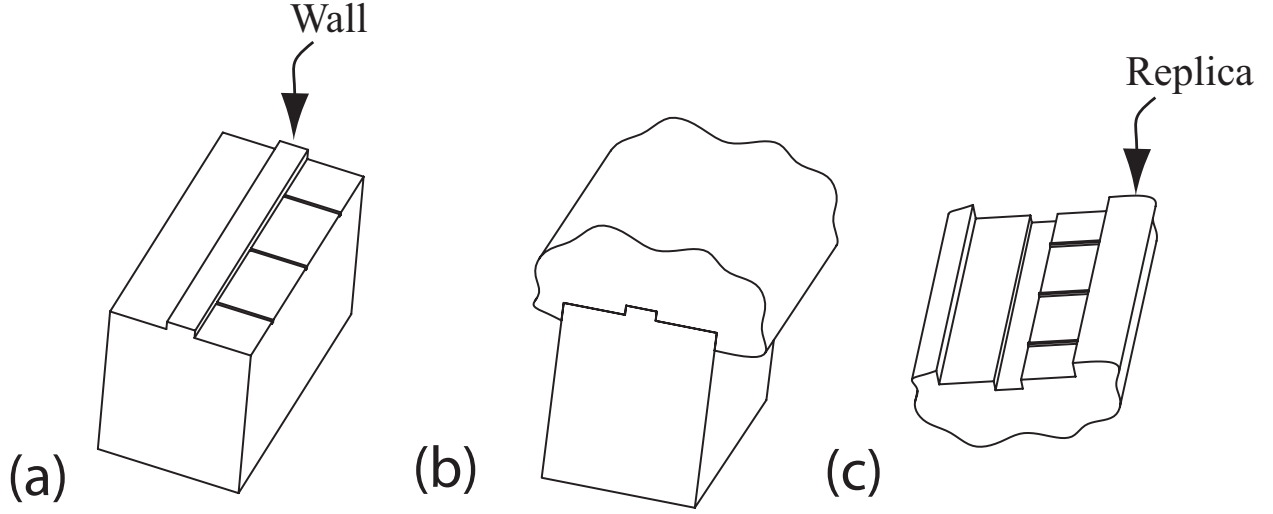


Figure 4.2: Replica based measurement procedure (a) Aluminum workpiece, (b) Replica material applied on top of the workpiece, and (c) Replica removed for measurement. The process is repeated after the prescribed cut and the two replicas are compared for depths at the location marked by ridges for obtaining the actual uncut chip thickness.

Table 4.1: Variation in uncut chip thickness.

Test	Prescribed (μm)	Measured (μm)	Thrust force (N)
1	10	10.1	4.8
2	10	10.8	4.6
3	20	19.9	5.4
4	20	20.5	5.6
5	40	40.9	9.9
6	40	39.9	11

4.3 Turning apparatus

Precision turning apparatus was assembled on a vibration isolation table. The setup consists of a precision spindle, a single-axis slide, a Kistler 9256C1 dynamometer, a single crystal diamond tool (same as the one described above), tool holders (to provide required rake and inclination angles) and a workpiece holder as shown in Fig. 4.4. The tool is connected to the slide, which provided the feed motion. A single-crystal aluminum workpiece used during plunge-turning experiments is given in Fig. 4.5. A square hole is created in the center of the workpiece to prevent slipping during machining. The workpiece is attached to the workpiece holder that is fixed on the spindle through a collet. The dynamometer was attached on the tool side to measure the forces during plunge turning.

The choice of the components was made based on the stiffness, load capacity and accuracy.

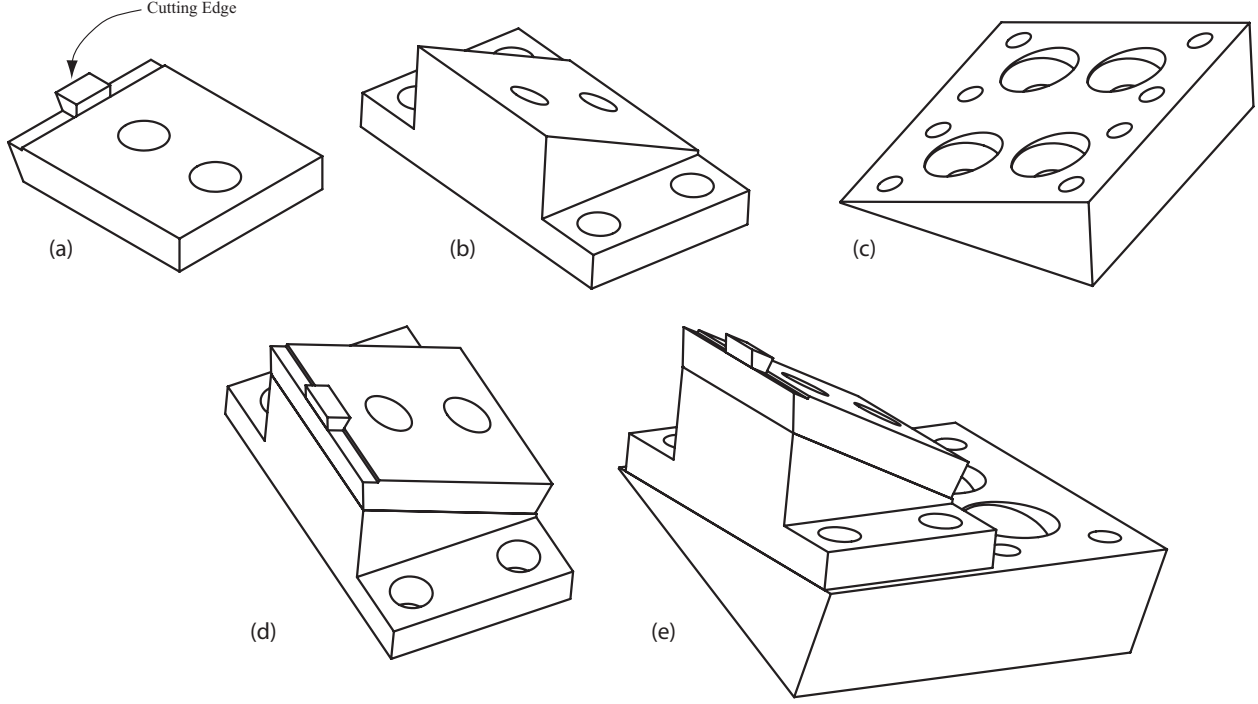


Figure 4.3: (a) Diamond tool design, (b) Holder for adjusting the rake angle, (c) Holder for adjusting the inclination angle, (d) Tool assembly with rake angle adjusted, and (e) Tool assembly with rake and inclination angles adjusted.

The set-up was designed to be of high rigidity to minimize experimental uncertainties. Since cutting forces are most strongly dependent on uncut chip thicknesses, the factors (and their values) affecting the uncertainty of uncut chip thickness are provided here for reference. These include the radial stiffness of the spindle, asynchronous component of the runout measured from the workpiece surface, alignment between slide motion axis and spindle rotation axis, and the accuracy of slide motion.

The radial and axial stiffness values obtained from the spindle manufacturer were 58 N/micron and 56 N/micron, respectively. The maximum asynchronous component of the runout measured from the surface of a XX gauge pin (0.75 inch diameter) using a laser Doppler vibrometer was equal to 205 nm. To minimize experimental errors resulting from vibrations, the spindle was belt driven using a speed controlled vector drive motor. The motion axis of the slide was aligned perpendicular to the rotation axis of the spindle within a tolerance of 0.1 degrees. The slide position was found to be within 1 micron from the commanded position.

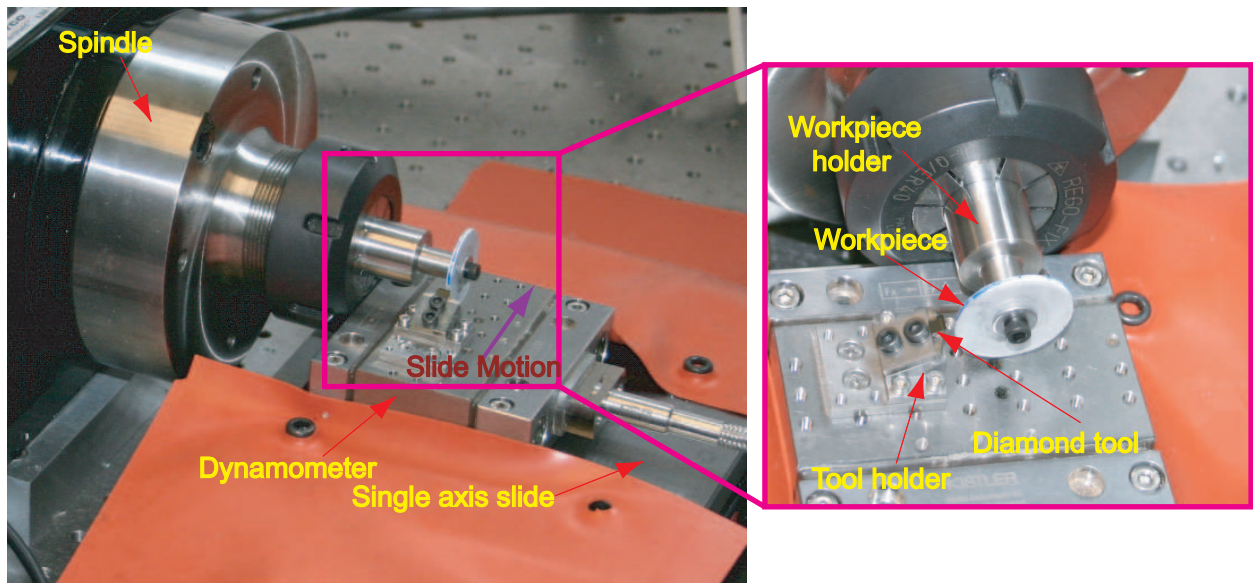


Figure 4.4: Turning apparatus.

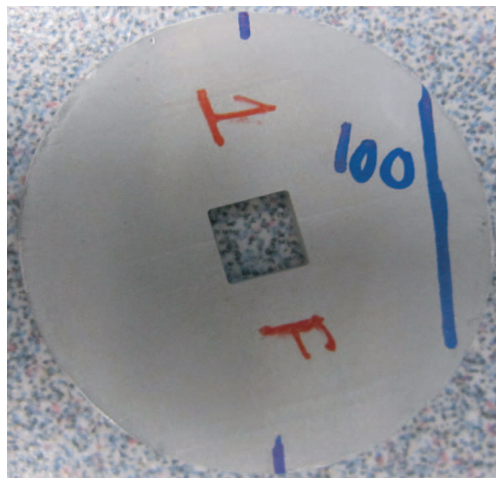


Figure 4.5: Single crystal workpiece.

Chapter 5

Machining of Coarse Grained Aluminum Including Crystallographic Effects

Although there exists a consensus in the literature that the crystallographic anisotropy of metals strongly affects their machining response [17, 19–26], quantitative observations on the effects of crystallographic anisotropy have been limited to only a few sets of cutting conditions and crystallographic orientations. Furthermore, although the subsurface deformation created by previous tool passes could change the machining response [24, 59] and its relationship with the crystallographic anisotropy significantly, no work in the literature provided comprehensive experimental data on the interaction effects between the subsurface damage and crystallography.

This chapter presents an experimental investigation on the effects of crystallographic anisotropy during orthogonal machining of coarse-grained pure aluminum. Orthogonal machining (planing) is chosen to simplify the kinematics of the process when analyzing the crystallographic effects. Experiments are conducted under varying feed (uncut chip thickness) values, cutting speeds, and rake angles, and the variations of machining forces (analyzed in terms of specific cutting energy and effective coefficient of friction) and surface roughnesses across different grains are measured. To analyze the effect of the subsurface damage in the presence of crystallographic anisotropy, experiments were conducted both with and without cleanup cuts that alleviate the subsurface deformation.

5.1 Experimental Methods

5.1.1 Experimental Facility

To conduct the experiments presented in this work, a sliding microtome was modified to create an orthogonal planing system shown in Fig. 5.1(a). The microtome consists of a vertical stage with 1 μm resolution, and a horizontal slide capable of moving at velocities ranging from 1 mm/s to 100 mm/s. A tool post was constructed on the vertical stage from extruded aluminum frames, and the tool is attached to the tool post through an adaptor plate. Therefore, the uncut chip thickness can be specified by moving the vertical stage. The workpiece was attached to the horizontal slide, which provides the cutting velocity. A force dynamometer (Kistler 9256C1) attached between the adaptor plate and the tool post facilitates measuring the three mutually-orthogonal machining force components (see Fig. 5.1(a)).

The stiffness of the structural loop is critical to ensure that the actual and specified uncut chip thickness (feed) values do not differ significantly due to deflections under machining forces. A set of preliminary tests was conducted to assess the difference between the specified and actual uncut chip thickness values: A protruded wall-like feature was machined on an aluminum 7075 workpiece (see Fig. 5.2) at different feed values, and the corresponding vertical forces were recorded. Between each cut, a negative replica of the wall was created (see Fig. 5.2) using a repliset system that, according to the manufacturer, is capable of replicating features less than 0.1 μm . The actual uncut chip thickness values were determined by measuring the change in feature depth on the replicas using white-light interferometry (WYKO). Table 5.1 provides the actual and prescribed uncut chip thickness values, and the associated vertical forces. It is seen that the difference between the measured and prescribed uncut chip thickness values never exceeded 1 μm for any of the test conditions. It is noted that the vertical forces considered in this evaluation study well-covers the range of vertical (thrust) forces measured during the experimentation on coarse-grained aluminum. Therefore, we expect the actual uncut chip thickness values during the experiments to be within 1 μm of the prescribed values.

5.1.2 Tool Characterization

The cutting edge sharpness, as measured by the radius of the cutting edge (the edge hone), has a profound effect in cutting mechanics. In particular, larger edge radii produces increased ploughing and more extensive deformations near the tool edge [60]. To minimize the aforementioned com-

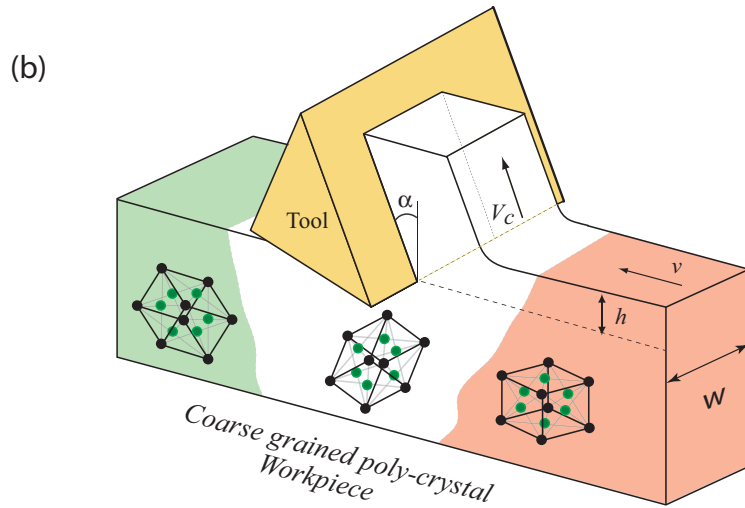
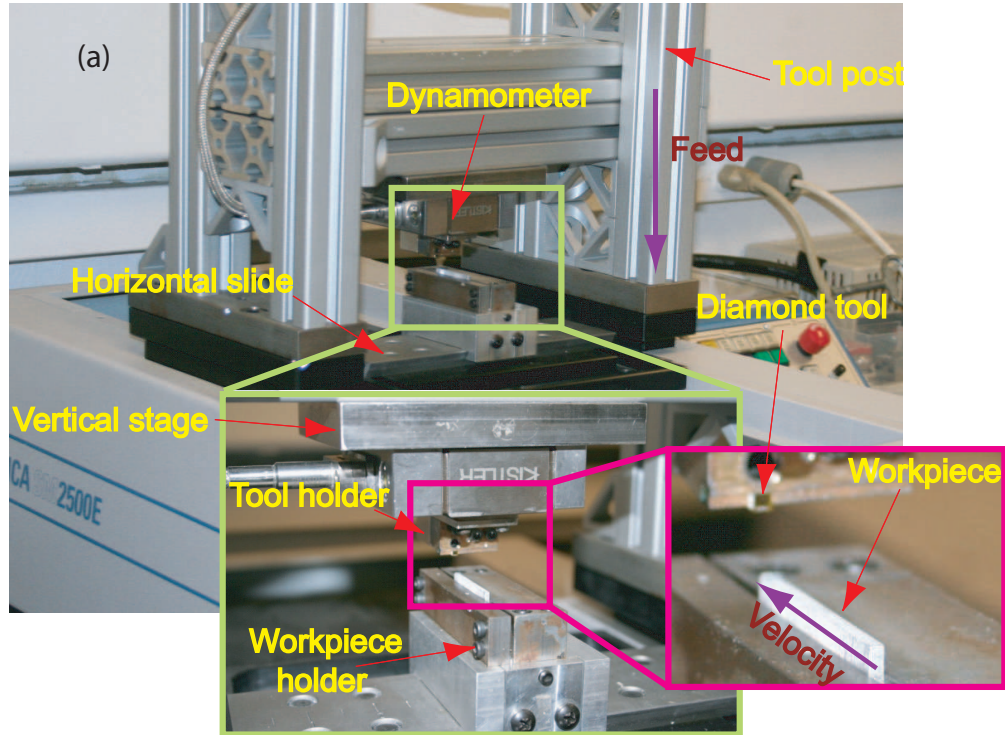


Figure 5.1: (a) Planing apparatus and (b) Schematic for machining coarse grained workpieces.

plexities arising from the use of non-sharp tools, especially while machining at the micro-scale, a custom made single crystal diamond tool was used during the experiments. The diamond tool has

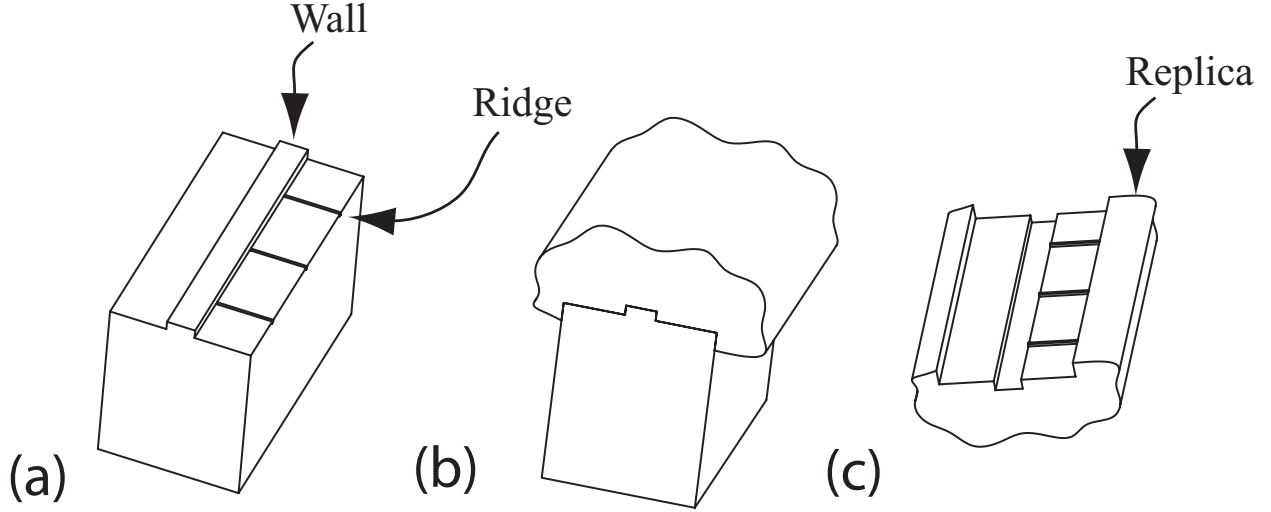


Figure 5.2: Replica based measurement procedure (a) Aluminum workpiece with the wall feature, (b) Replica material applied on top of the workpiece, and (c) Replica removed for measurement. The process is repeated after each cut and the depth of the replicas are measured at ridge locations to obtain the actual uncut chip thickness.

Table 5.1: Results of the preliminary study to measure the difference between the actual and prescribed uncut chip thicknesses.

Test	Prescribed (μm)	Measured (μm)	Vertical Force (N)
1	10	10.1	4.8
2	10	10.8	4.6
3	20	19.9	5.4
4	20	20.5	5.6
5	40	40.9	9.9
6	40	39.9	11

an edge length (cutting width) of 2.5 mm and an included angle of 60 degrees. The rake angles can be selected within 0 deg. to 25 deg. range by using different tool-holder adaptors, while still maintaining a clearance angle of at least 5 degrees. For a quantitative assessment of the tool, the edge radius was measured at eight locations along the edge with an atomic force microscope using the technique described in [26, 54–57]. The measured edge radius was found to be $150.18 \text{ nm} \pm 20.26 \text{ nm}$ along the cutting edge. Since the minimum uncut chip thickness during the experiments is $10 \mu\text{m}$, this level of edge sharpness is considered to eliminate the effects of tool edge radius on cutting mechanics.

5.1.3 Workpiece Characterization

Two samples of high purity aluminum (99.999%) were cut and polished to create workpieces with uniform widths (1.89 mm and 1.48 mm, respectively). To obtain coarse grained samples, the workpieces were subsequently annealed at 400°C for 30 minutes. The resulting coarse grained workpieces (with grain lengths ranging from 1 mm to 10 mm along the length of the workpiece) were etched with hydrochloric acid to reveal the underlying grain structure. The grains were then traced under oblique lighting conditions. Only those grains that span the entire width of the workpieces were indexed, and they were labeled as A_1 to A_6 for Workpiece 1 and B_1 to B_{11} for Workpiece 2. Figure 5.3 shows the side view of the two workpieces, where the grain boundaries are identified. To verify the location of grain boundaries, and to determine the orientation of each grain, orientation imaging microscopy (OIM) was used after the completion of the cutting tests. A typical orientation map obtained from OIM is overlapped on the workpiece image in Fig. 5.3. The measured orientations of each grain are given in Table 5.2 in terms of the three Euler angles.¹ Figure 5.4 shows cutting directions and cutting plane normals in terms of crystal coordinates projected on standard stereographic triangles. Since the orientations are well distributed over the stereographic triangles, the conclusions drawn from the experiments would not be biased towards specific crystallographic orientations.

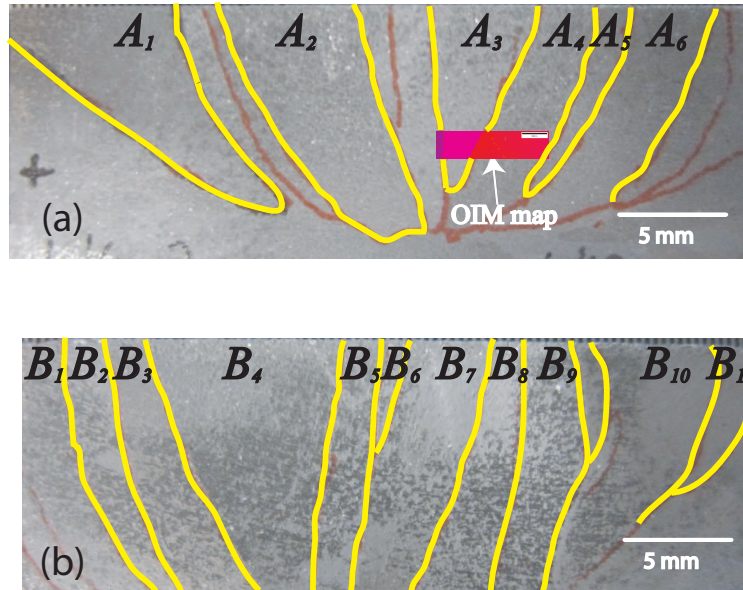


Figure 5.3: (a) Workpiece 1 and (b) Workpiece 2 with traced grain maps.

¹The orientation of grain B_6 could not be determined due to its insufficient size after the tests were completed.

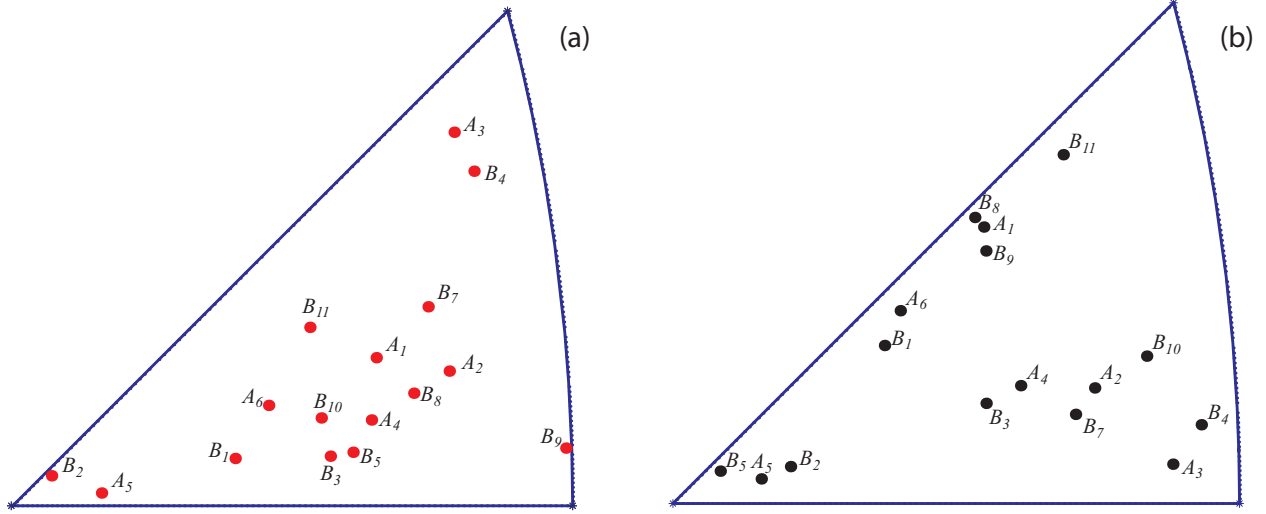


Figure 5.4: Projections of (a) Cutting plane normals and (b) Cutting directions, in the standard stereographic triangle.

5.1.4 Cutting Conditions

The effects of cutting velocity (v), uncut chip thickness (h), and rake angle (α) on machining forces and surface finish were studied in the presence of crystallographic anisotropy. To also analyze the effect of subsurface deformation, experiments were conducted both with and without cleanup cut. The experimental conditions were selected based on the capabilities of the experimental setup in terms of cutting velocity, uncut chip thickness, width of cut and rake angles, and a full factorial design of experiments was conducted. The cutting conditions used during the study are provided in Table 5.3.

5.1.5 Experimental Procedure

The experiments were performed on the coarse grained aluminum workpieces to enable analyzing the effects of cutting conditions and tool geometry on machining in the presence of crystallographic anisotropy. The adhesion of pure aluminum to the rake face of the diamond tool observed during the preliminary tests was eliminated by using a cutting fluid (Ecoline), which was applied on the rake face of the tool and the surface of the workpiece using a cotton swab prior to each test. The order of experiments were randomized, and two repetitions were performed for each set of conditions. The three-component force data was collected at a sampling rate of 5 kHz during the experiments. For each set of cutting conditions, experiments both with and without cleanup cuts were performed.

Table 5.2: Orientations of the grains.

Grain number	φ_1 (deg.)	ϕ (deg.)	φ_2 (deg.)
A_1	53	38	327
A_2	131	14	265
A_3	84	28	316
A_4	36	12	294
A_5	45	11	316
A_6	28	18	312
B_1	343	13	35
B_2	341	10	16
B_3	333	9	53
B_4	283	26	36
B_5	278	29	85
B_6			
B_7	246	17	171
B_8	305	42	36
B_9	296	51	46
B_{10}	215	49	147
B_{11}	220	40	163

Table 5.3: Experimental conditions for orthogonal machining studies.

Uncut chip thickness (μm), h	10, 20, 40
Rake angle (deg.), α	0, 10, 25
Cutting speed (mm/s), v	10, 50

Prior study in the literature [59] has indicated that the depth of the subsurface deformation imparted by the cutting process does not exceed the uncut chip thickness of the previous tool pass. Hence, in this work, the subsurface damage was mitigated significantly by performing multiple 2 μm cleanup cuts before each with-cleanup test, with a total removal depth equal to the uncut chip thickness of the previous cut.

The roughness of the cut surfaces were analyzed only for the with-cleanup tests. A replica-based roughness measurement procedure was followed to avoid removing the workpiece from the experimental setup between tests: A replica of the cut surface was made using the Repliset system after every cut (in a similar manner to that shown in Fig. 5.2). The roughness measurements were later taken from the replicas using an optical profilometer (Zygo NewView 7300). The measurements were performed over an area of $180 \mu\text{m} \times 50 \mu\text{m}$ on the center of each grain along the length direction from the mid section of the workpiece width. A set of preliminary experiments conducted to assess the accuracy of the replica-based roughness measurement capability indicated that the average surface roughnesses (R_a) measured from the actual surface and its replica differs by less than 4 nm.

5.2 Results and Discussion

The kinematics of orthogonal machining and associated machining forces are depicted in Figure 5.5, where F_c , F_t , and F are the cutting, the thrust and the resultant (machining) forces, respectively. ϕ and β represent the shear angle and the friction angle, respectively in Fig. 5.5. To represent the cutting process in a normalized fashion, the experimental machining forces are divided by the uncut chip area, which is equal to the product of the width of the workpiece (width of cut) and the uncut chip thickness, to obtain the specific cutting (u_c) and specific thrust (u_t) energies. A typical variation of specific energies across the grains along the length of the workpiece is shown for each workpiece in Fig. 5.6, where the solid lines indicate the specific energy averaged over two repetitions, and the gray band indicates the variation about the average. For presenting the specific energy data, the length axis is normalized to the total sample length, and shown as a percentage. To eliminate the transient effects observed during the transition from one grain to the next, average specific energy values were calculated for each grain from the forces averaged over the half-length of the grain about the center of the grain. The observed abrupt changes on specific energy signatures across the grain boundaries are due to the anisotropy of consecutive crystals, rather than a direct effect from the grain boundaries themselves, which are only a few atoms thick.

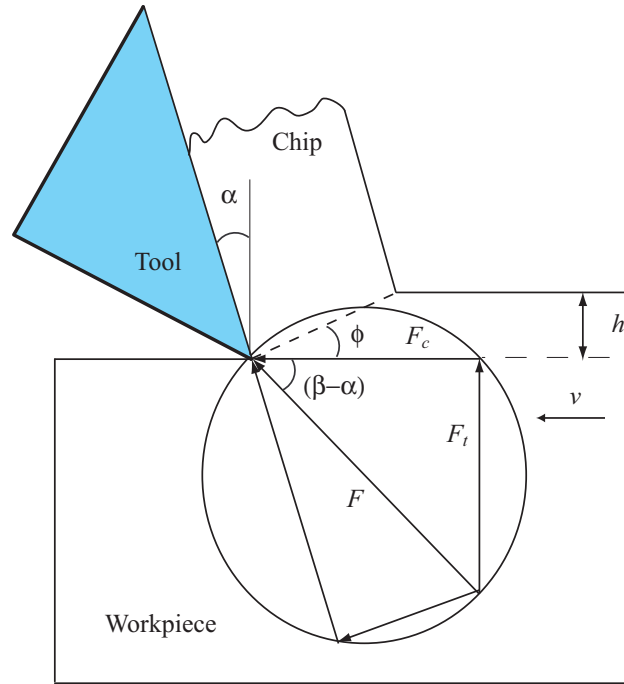


Figure 5.5: Kinematics of the orthogonal cutting and the Merchant's force circle diagram.

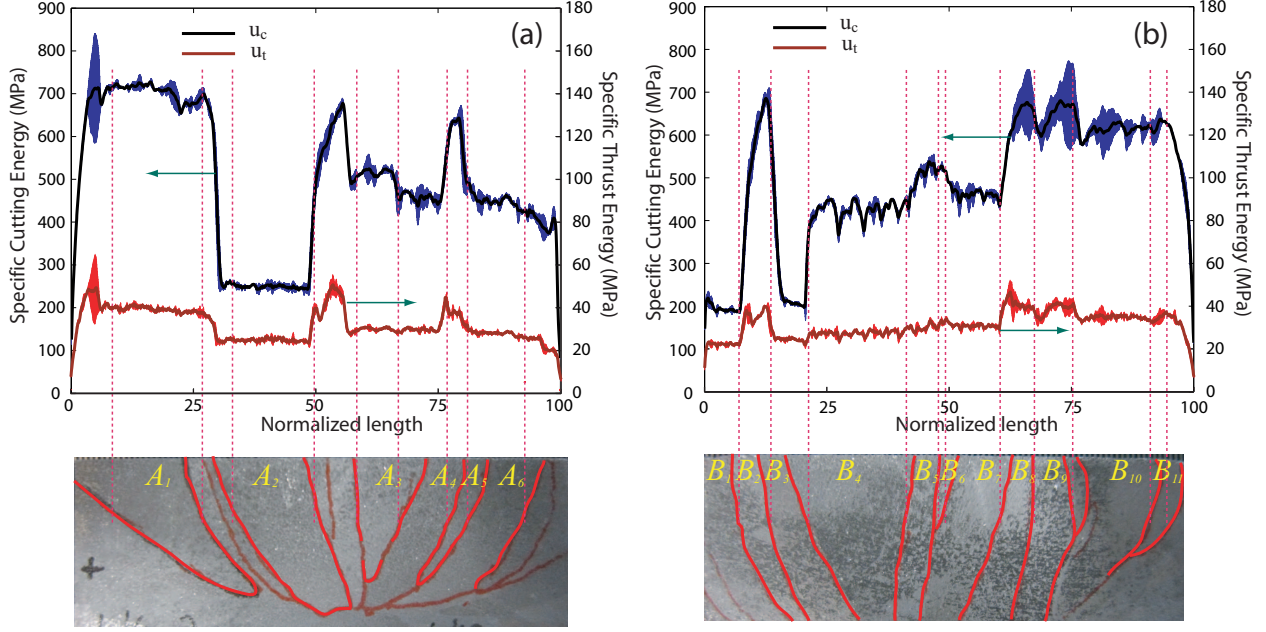


Figure 5.6: Typical specific energy variations for (a) Workpiece 1 and (b) Workpiece 2, for 0 degree rake angle, 10 mm/s cutting velocity, and 40 μm uncut chip thickness.

In general, the grain-to-grain variations of specific thrust energies were seen to follow those of specific cutting energies (see Fig. 5.6). However, while the specific cutting energy is always positive, the specific thrust energy exhibits both positive and negative values due to the force equilibrium in orthogonal cutting at higher rake-lower friction conditions. For this reason, a quantitative comparison between the maximum and minimum specific thrust energies across grain orientations is not informative. Therefore, the analysis presented here focuses mainly on the specific cutting energies and the effective coefficient of friction (μ), which is calculated as

$$\mu = \tan(\alpha + \arctan(\frac{u_t}{u_c})). \quad (5.1)$$

Together, the specific cutting energy (cutting force) and the effective coefficient of friction completely describe the kinematics of the orthogonal cutting process, allowing other force components to be calculated with the knowledge of the rake angle. It is important to note that the observed variations of effective coefficient of friction are not accompanied with physical explanations of the effects. This is due to the fact that the calculation of the effective coefficient of friction is only provided to characterize the change in cutting force ratios, rather than the changes in actual friction characteristics.

To assess the repeatability of the experimental results and their statistical significance, a multi-

variate analysis of variance (ANOVA) was performed on the average specific cutting energies and the effective coefficients of friction. In this analysis, the statistical significance of a factor was decided considering a 95% confidence interval (a P value less than 0.05) [65]. A preliminary analysis including all the interaction effects indicted that, while some high-level interaction effects were statistically significant, their F values (normalized magnitudes) were considerably smaller than those of the main and two-way interaction effects. Therefore, only the main and two-way interaction effects were considered in this study.

The factors used in the ANOVA analysis included crystallographic orientation (17 levels), rake angle (3 levels), cutting velocity (2 levels), uncut chip thickness (3 levels), and cleanup status (2 levels - with and without). Table 5.4 presents the results from the ANOVA analysis for the specific cutting energy and the effective coefficient of friction, where the statistically *insignificant* values are italicized: It is seen that except the interaction between orientation and cutting velocity, and that between velocity and uncut chip thickness, all the main and interaction effects are statistically significant for the specific cutting energy. For the effective coefficient of friction, three interaction effects were not statistically significant.

Table 5.4: ANOVA results for the specific cutting energy and the effective coefficient of friction, where “*” denotes the interaction between two parameters.

Parameter	P (u_c)	F (u_c)	P (μ)	F (μ)
Orientation (e_1)	0.000	236.02	0.000	185.67
α (e_2)	0.000	3109.18	0.000	348.49
v (e_3)	0.000	63.26	0.000	16.61
h (e_4)	0.000	164.26	0.000	497.28
Cleanup (e_5)	0.000	1204.92	0.000	52.14
$e_1^*e_2$	0.000	50.89	0.000	23.60
$e_1^*e_3$	0.621	0.86	0.015	4.07
$e_1^*e_4$	0.000	8.17	0.000	42.89
$e_1^*e_5$	0.000	42.74	0.000	3.38
$e_2^*e_3$	0.003	5.77	0.009	4.69
$e_2^*e_4$	0.000	7.48	0.000	51.84
$e_2^*e_5$	0.000	275.64	0.213	1.55
$e_3^*e_4$	0.121	2.11	0.084	2.49
$e_3^*e_5$	0.000	16.38	0.072	3.25
$e_4^*e_5$	0.000	11.52	0.000	11.49

5.2.1 Machining after Cleanup Cuts

In this section, the effects of cutting conditions and their interaction with the crystallographic anisotropy are analyzed in detail for surfaces that are prepared by performing the cleanup cuts.

5.2.2 The Main Effects of Crystallographic Anisotropy

The main-effect plot for the crystallographic orientation on specific cutting energy is given in Fig. 5.7(a). This plot averages the specific cutting energies over all the conditions: Although the exact variation between the orientations depends upon the specific set of cutting conditions, the main effect plot provides an overall perspective on the effect of anisotropy. The averaged specific cutting energies were seen to vary significantly with the crystallographic orientation. The specific cutting energy was seen to vary by as much as 360% (between grains B_1 and B_2).

The strong effect of crystallographic anisotropy arises from the dependence of the deformation behavior of crystals upon the arrangement of slip systems with respect to the cutting orientation (both the plane normal and the cutting direction). Some researchers [34, 66] attempted to capture the effect of crystallographic anisotropy by calculating the Schmid factors along the direction of the resultant machining force. To determine the variation of the Schmid factor during the experiments presented here, the resultant force magnitude and direction was calculated from the measured cutting and thrust forces. Subsequently, the associated Schmid factors for the average resultant force directions for each orientation were determined and presented in Fig. 5.8. It is seen that the maximum variation in Schmid factors was 16%. Thus, the observed variations due to crystallographic anisotropy cannot be explained through the Schmid factors. This is an expected result, since the Schmid-factor based models assume that the deformation occurs only along a single slip system: In reality, fcc metals have 12 slip systems, and generally five independent slip systems must be activated simultaneously to accommodate an arbitrary deformation. Prediction and quantitative analysis of the effect of anisotropy under such conditions would require more elaborate plasticity-based models of the machining process [45, 48], including multiple slip, hardening, and crystal rotation effects.

The variation in effective coefficient of friction with orientation is shown in Fig. 5.7 using the main effect plot obtained by averaging over uncut chip thicknesses, cutting velocities, and rake angles. Except for three crystals, the average coefficient of friction was observed to be within a narrow range of 0.07 to 0.1 (corresponding to 4 to 5.7 degrees in terms of friction angle). On closer observation and comparing with the main effects plot for the specific cutting energy, the three outliers were seen to be for orientations whose specific cutting energies are the lowest (A_2 , B_1 , B_3). It is possible that unbiased noise affects those low specific energy values, and thus, prevents accurate calculation of the effective coefficient of friction. Overall, within the range of parameters tested in this study, the variation of effective coefficient of friction with crystallographic orientation was seen to be minimal. This indicates that the cutting and thrust forces are well-correlated across

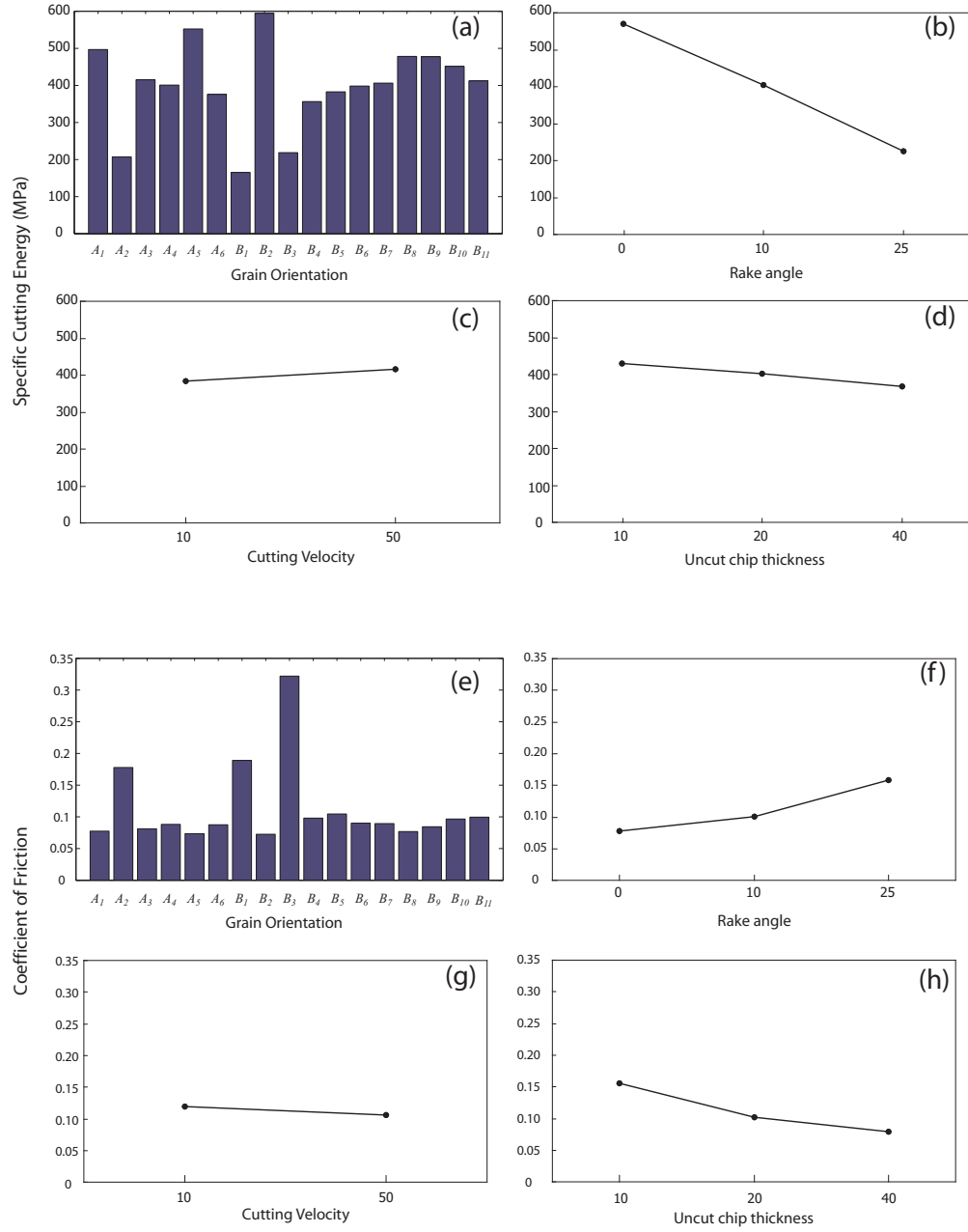


Figure 5.7: Main effect plots for (a-d) Specific cutting energy and (e-h) Effective coefficient of friction.

different crystallographic orientations.

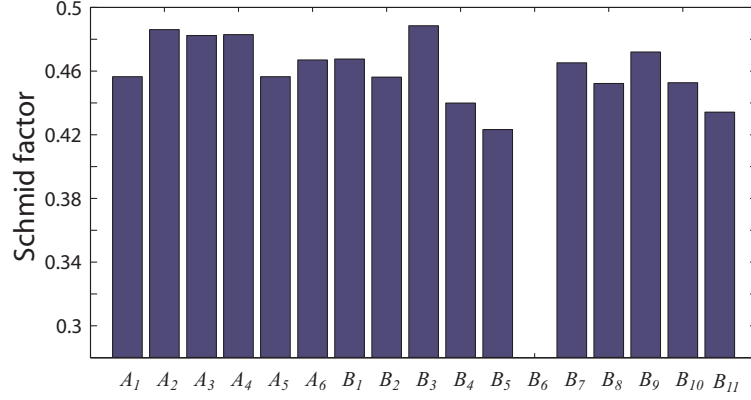


Figure 5.8: Schmid factors for the resultant machining force directions.

The Effects of Rake Angle

The main effect of the rake angle on specific cutting energy is seen in Fig. 5.7(b). It is seen that the increasing the rake angle reduces the specific cutting energy. The average specific cutting energy at zero degree rake angle is observed to be higher than that at 25 degree rake angle by approximately 250%. This effect is similar to that seen in machining of effectively isotropic materials, and is due to the lower shear strains that reduce the extent of deformation at increased rake angles.

More detailed observations about the effects of rake angle can be made by analyzing the specific cutting energy signatures. Figure 5.9 shows a sample data for both workpieces for 10 mm/s cutting speed at different uncut chip thickness values. The small shift observed in the individual grain signatures arises from the fact that the grain boundaries are not aligned with the feed direction, and thus, the starting and ending position of each crystal changes in subsequent tests. As concluded from the ANOVA analysis, the specific cutting energies were seen to reduce with increasing rake angles.

The interaction between the rake angle and orientation effects is critical to the current study. Figure 5.10(a) presents the specific cutting energies for each rake angle by averaging the data over all the cutting speeds and uncut chip thicknesses. It is clear that the effect of rake angle is not uniform across different crystallographic orientations: The maximum variation of average specific cutting energy was seen be 415% at 0 degree rake angle and 250% at 25 degree rake angle. This implies that the variation of specific cutting energy arising from the anisotropy increases with reducing rake angle. In other words, the cutting process is more sensitive to effects of anisotropy at lower rake angles.

A possible explanation for the observed phenomena may be offered by considering the change

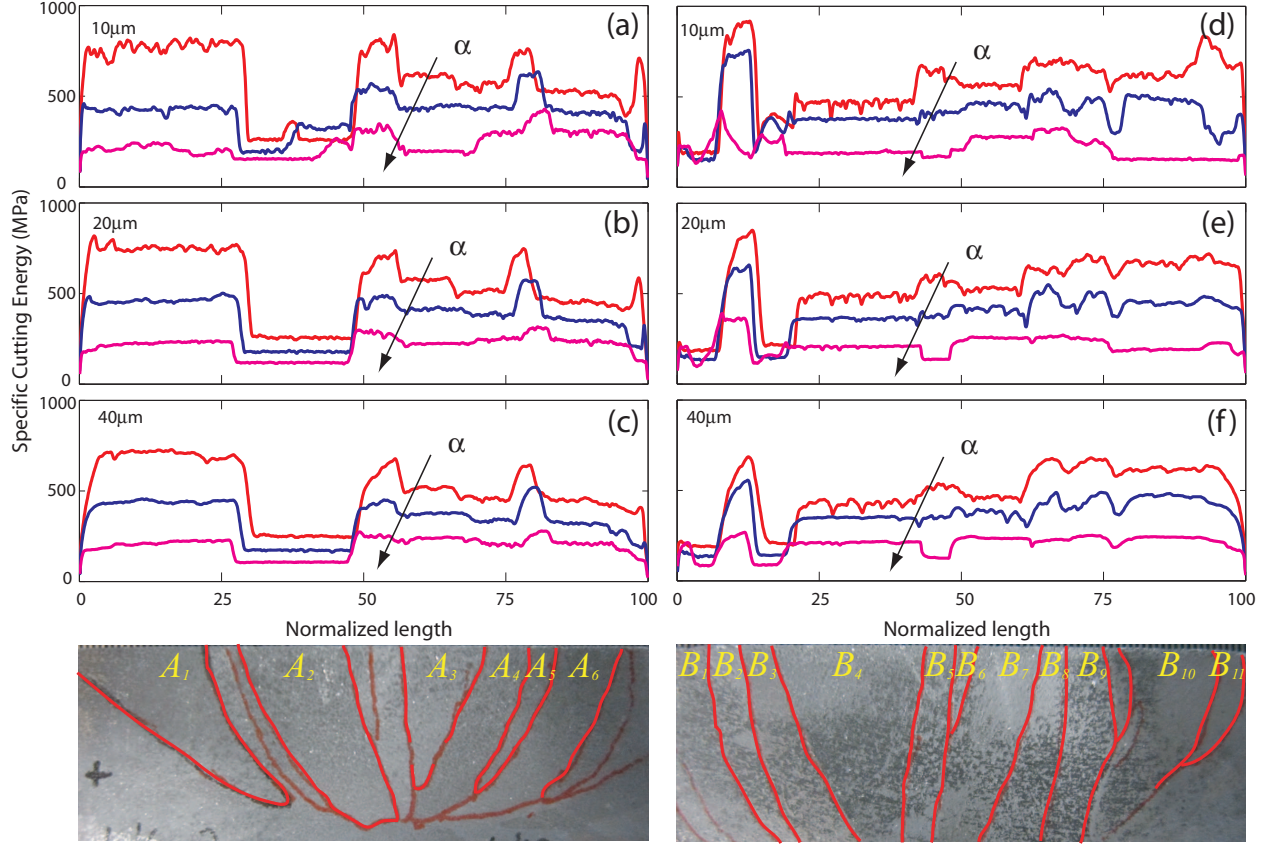


Figure 5.9: Effect of rake angle on specific cutting energy signatures at various cutting conditions for (a-c) Workpiece 1 and (d-f) Workpiece 2, at 10 mm/s cutting velocity. The guidelines show the approximate midpoint of each grain for visual correlation only.

in shear angle and shear strain with varying rake angle. Since a change in rake angle causes the average shear direction to change, even for the same cutting direction and crystal orientation, the plastic deformation during machining may vary significantly. Furthermore, the magnitude of strain experienced by the material also varies with the change in shear angle. Increased strains at lower rake angles, combined with the changes in orientation of the shear deformation, could result in increased variation in specific cutting energy with reducing rake angle.

The effective coefficient of friction (main effect) was seen to increase with increasing rake angles. The average value of the effective coefficient of friction was 0.16 at 25 degree rake angle and 0.08 at 0 degree rake angle. However, the variation of effective coefficient of friction across crystallographic orientations was found to be similar at all rake angles (see Fig. 5.11(a)).

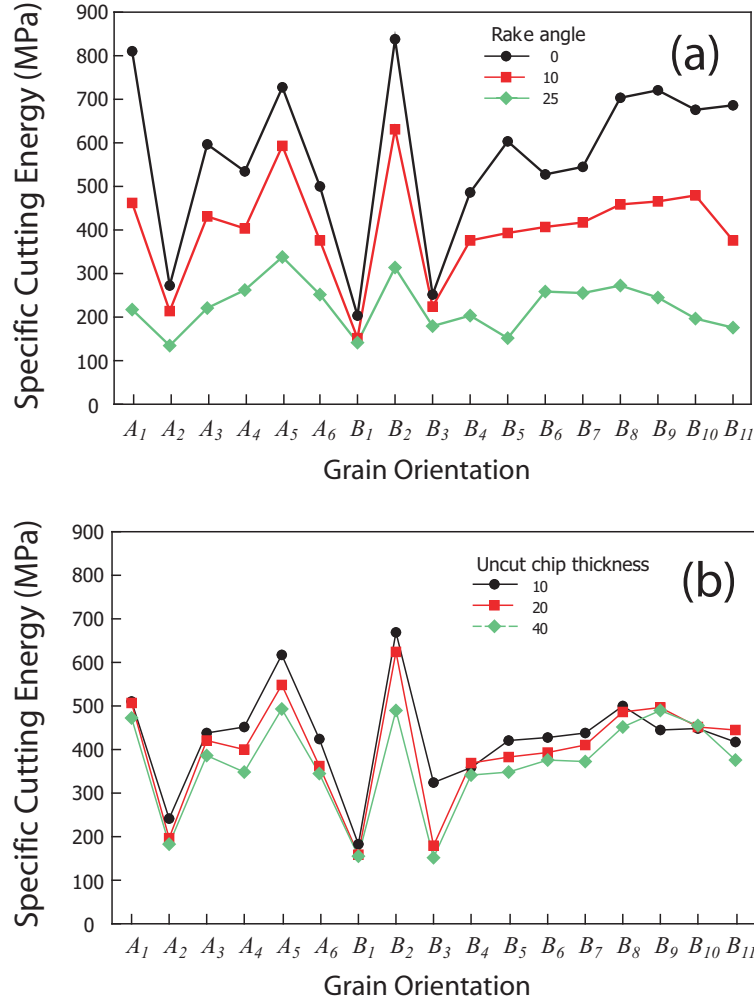


Figure 5.10: Two- way interaction effects for specific cutting energy between (a) the grain orientation and the rake angle and (b) the grain orientation and the uncut chip thickness.

The Effects of Cutting Velocity

As seen in Table 5.4 and Fig. 5.7(c), the main effect of the cutting velocity on specific cutting energy was seen to be statistically significant. Increased cutting speeds were observed to produce higher specific cutting energies. However, within the range of cutting velocities considered in this work, the effect of cutting velocity was seen to be small. Averaging over the crystallographic orientations, rake angles and uncut chip thicknesses, the specific cutting energy is only 8.6% higher at 50 mm/s than at 10 mm/s.

Changes in cutting velocities affects the cutting process through two opposing mechanisms. First, at increased strain rates experienced at higher cutting velocities, most metals show increased

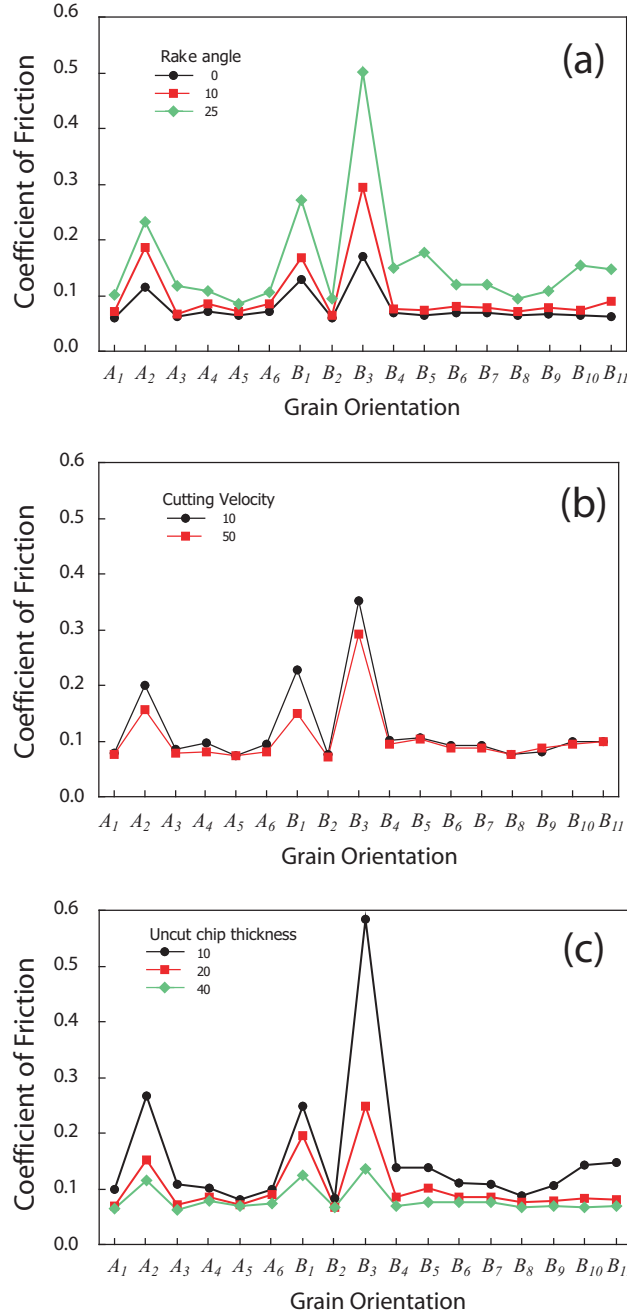


Figure 5.11: Two- way interaction effects for specific cutting energy between (a) the grain orientation and the rake angle, (b) the grain orientation and the cutting velocity, and (c) the grain orientation and the uncut chip thickness.

resistance against yielding, and thus, the specific cutting energies increase at higher velocities. Second, for a wide range of cutting speeds, increasing cutting velocity increases the workpiece temperatures, thereby softening the material, and thus, reducing the specific energies. For the

relatively low-speed regime considered in the current tests, the former effect is considerably more dominant. More specifically, the effect of cutting speed is seen mainly on the stress distribution for a given applied strain. The resulting stress distribution is related to the strain rate through a power law relationship, typically in the form of $\sigma \propto (\dot{\gamma})^{\frac{1}{n}}$, where σ is the stress, $\dot{\gamma}$ is the strain rate, and n is the coefficient of rate sensitivity. The strain rate is directly proportional to the cutting velocity, and typical values of n for metals range from 10 to 30. Consequently, the effect of strain rate, and thus, the cutting velocity, on the stress response is relatively small. For instance, for coefficient of rate sensitivities within a range of 10 to 30, a five fold increase in the cutting speed (strain rate) would result in a change of stress values within 5% and 17%. In the current set of experiments, the increase in specific cutting energy was seen to be 8.6% for a five-fold increase in the cutting velocity.

However, the interaction effect between the cutting velocity and crystallographic orientation on specific cutting energy was seen to be statistically insignificant. This can be explained by considering the stress-strain rate dependance described above: Since coefficient of rate sensitivity (n) is commonly independent of the orientation, the effect of speed is expected to be uniform across all orientations.

Although statistically significant, the cutting velocity was seen to have a little effect on the calculated average coefficient of friction (see Fig. 5.7(g)). In terms of friction angle the variation is less than one degree. The variation of effective coefficient of friction across crystallographic orientations was found to be similar at all cutting velocities (see Fig. 5.11(b)).

The Effects of Uncut Chip Thickness

Table 5.4 and Fig. 5.7(d) shows that the main effect of the uncut chip thickness is statistically significant, and reduced uncut chip thickness results in increased specific cutting energies. The specific cutting energy at 10 μm was seen to be 17% higher than that at 40 μm .

This phenomena, commonly referred to as the size effect, has been observed frequently in the machining literature for effectively isotropic materials, e.g., in [61–63]. Researchers have attributed the size effect to the deformation characteristics of the material [63], the edge radius of the tool, and the fracture energy [64] necessary for chip separation. Due to the sharp diamond tool used in the current set of experiments, the effect of edge radius can be considered negligible. Both the fracture energy for chip separation and shearing behavior of the material could be orientation dependent, and may be responsible for the observed size effect. However, since the raise in specific

cutting energy due to the uncut chip thickness reducing from 40 μm to 10 μm is approximately the same for each rake angle (18%, 16% and 19%, respectively at 0 degree, 10 degree, and 25 degree rake angles, respectively), it may be deduced that the amount of deformation does not affect the size effect significantly. Therefore, the observed size effect is most probably arising from the chip separation and new surface creation energies, which are commonly considered to be constant (and independent from the uncut chip thickness).

Figure 5.12 shows the change in specific energies at three levels of uncut chip thickness for the two workpieces. It is seen here that the size effect is not uniform across different crystals. Therefore, there is an interaction effect between the uncut chip thickness and crystallographic orientation. The interaction effect could be visualized more effectively by averaging the specific energies for each uncut chip thickness over the cutting speed and rake angles, as shown in Fig. 5.10(b).

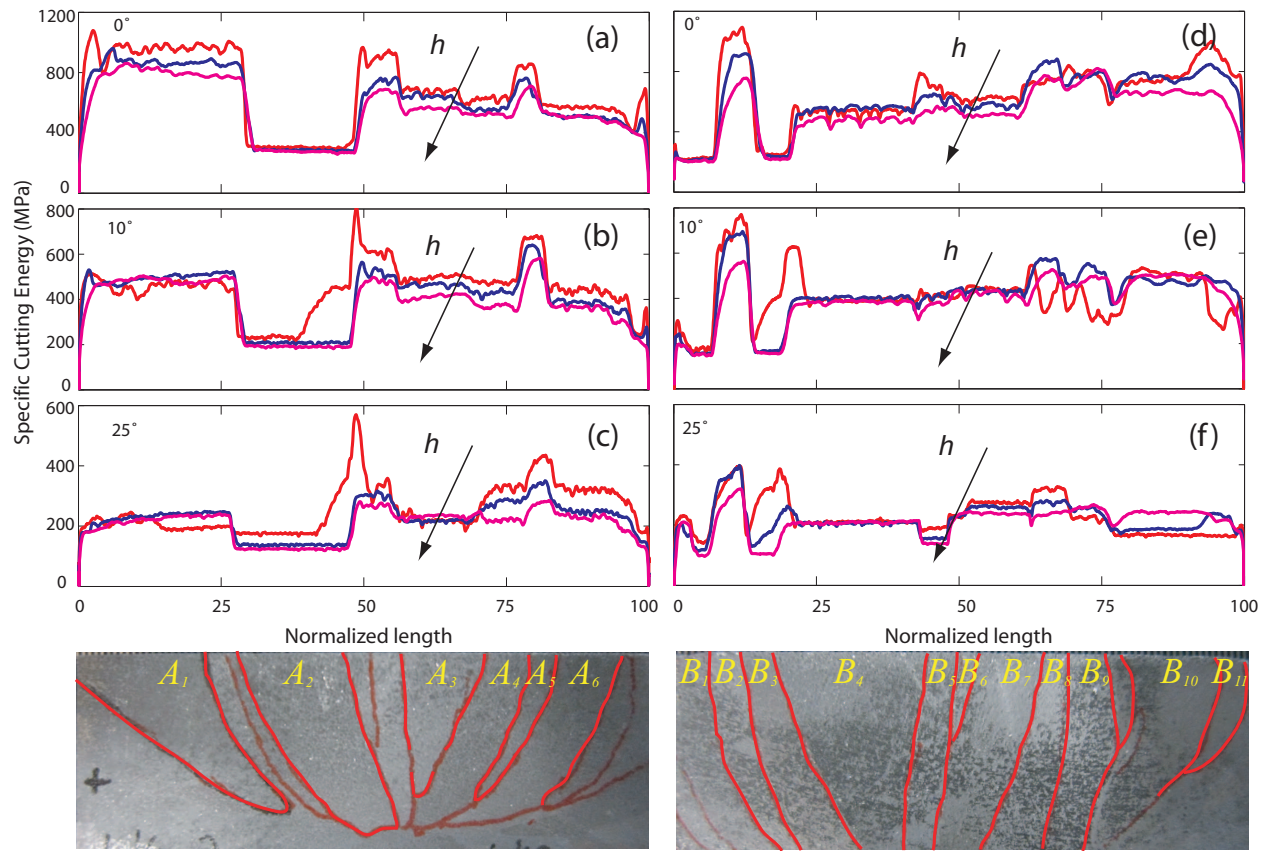


Figure 5.12: Effect of uncut chip thickness on specific cutting energy signatures at various cutting conditions for (a-c) Workpiece 1 and (d-f) Workpiece 2, at 50 mm/s cutting velocity. The guidelines show the approximate midpoint of each grain for visual correlation only.

The effective coefficient of friction (main effect) was seen to reduce at higher uncut chip thick-

nesses. Figure 5.7 shows that the average effective coefficient of friction at 10 μm uncut chip thickness is more than twice (212%) of that at 40 μm uncut chip thickness. Furthermore, the variation of effective coefficient of friction with crystallographic orientations was similar (see Fig. 5.11(c)) at all uncut chip thicknesses.

5.2.3 Machining Surfaces without Cleanup

The presence of subsurface deformation from the previous cuts affects the material properties experienced during the subsequent cut. As a result, both the deformation behavior and the specific energies vary due to existing subsurface deformation. For the results presented in the previous section, cleanup cuts were performed to minimize the effect of subsurface deformation. In this section, a systematic study is presented to assess the effect of subsurface deformation on specific energies in the presence of crystallographic anisotropy. As seen in Table 5.4, the main effect of the cleanup cuts, as well as its interaction effect with crystallographic orientations, are both statistically significant.

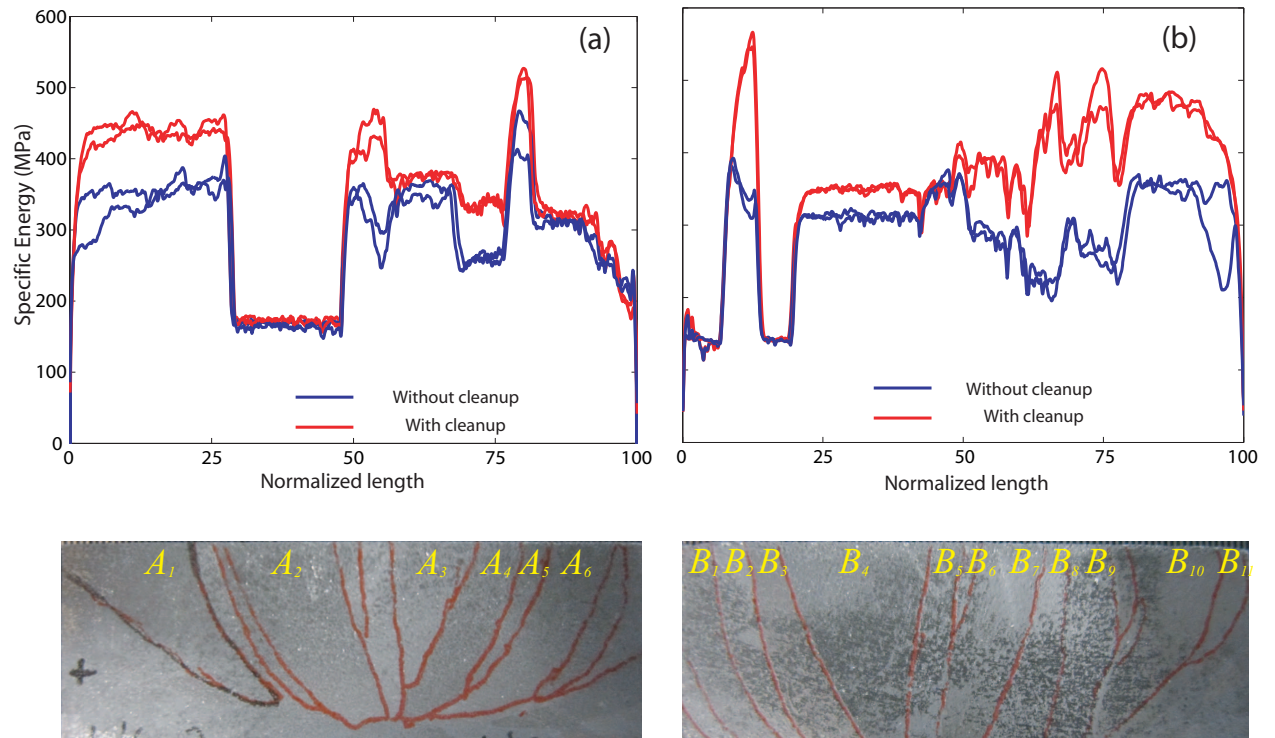


Figure 5.13: Typical effect of cleanup cut on specific cutting energy for (a) Workpiece 1 and (b) Workpiece 2.

A typical specific energy variation for a test with the cleanup cuts and the immediately following

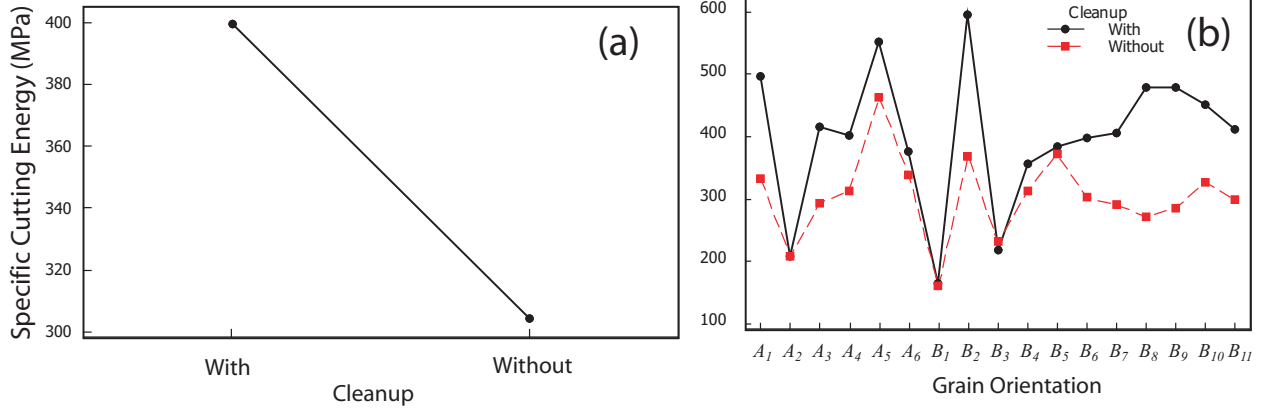


Figure 5.14: (a) Main effect of cleanup cut and (b) Two-way interaction effect for specific cutting energy between (a) the grain orientation and the cleanup cut.

test (without cleanup cuts) are given in Fig. 5.13, where a 10 degree rake angle, a 10 mm/s cutting velocity, and a 40 μm uncut chip thickness were used. The main effect of the cleanup is shown in Fig. 5.14(a). Averaging across all test conditions, the cases with cleanup cuts resulted in a 31% higher specific cutting energy than those without cleanup cuts. Furthermore, the interaction effect between the cleanup and the rake angle is also statistically significant: This is possibly due to the larger deformations at lower rake angles causing the effect of cleanup cut to become larger at lower rake angles. The average increase in specific cutting energy with cleanup cuts is 8.7%, 29% and 45% at 25 degree, 10 degree, and 0 degree rake angles, respectively.

Although the interaction effect of uncut chip thickness and cleanup were seen to be statistically significant, the effect of cleanup is observed to be similar at different uncut chip thickness values. The cases without cleanup at 10 μm and 40 μm uncut chip thicknesses showed 29% and 26% reduction in average cutting specific energies, respectively, when compared to cases with cleanup cuts.

When compared to the experiments conducted with (after) cleanup cuts, the cases without cleanup cuts showed lower variation in specific cutting energy with crystallographic orientation, as shown by the two-way interaction effect depicted in Fig. 5.14(b). The standard deviation (with orientation) of average specific energy without cleanup cuts was equal to 68 MPa, whereas that with cleanup cut was equal to 115 MPa. This reduction in standard deviation indicates that larger subsurface deformation reduces the effect of anisotropy. Within the deformed regions of the subsurface, the lattice is not uniformly oriented [59]. The orientation of the crystal changes gradually from the surface. Therefore, during a cut without cleanup, the orientation of a large

portion of the material begin removed is different from the original orientation of the bulk crystal.

For the effective coefficient of friction, the main effect of cleanup and its interaction effect with the uncut chip thickness are seen to be statistically significant. The effective coefficient of friction is seen to increase by 15% without cleanup, and the increase is seen to be higher at lower uncut chip thicknesses. The effective coefficient of friction without cleanup is seen to increase by 20%, 16%, and 5% at 10 μm , 20 μm , and 40 μm uncut chip thicknesses, respectively.

5.2.4 Analysis of Surface Roughness

It was observed in the literature that machining different crystallographic orientations under the same cutting conditions could result in different surface roughnesses [20, 22, 31]. However, these experiments were performed on a very few orientations (and cutting conditions) [20], and only qualitative observations were made [31].

When machining an effectively isotropic material, the roughness of the generated surface depends upon the quality of the tool, kinematics of the process, and the vibrational response of the machining system. In the current study, the same tool is used for each test across different crystals, and since the wear of the diamond tool is negligible, the effect of tool quality on the surface roughness is uniform across the crystals and under different conditions. The kinematics of the process for given set of cutting conditions were also identical across different grains. Furthermore, at the steady state (away from the transition region from one crystal to another), the vibrational response of the structure could be assumed to be uniform.

When considering machining of single crystals and coarse-grained samples, the surface generation mechanism may play an important role. The generated surface is directly correlated with the orientation of the crystals, since the surface is generated by large plastic deformation of the material ahead of the tool edge combined with the separation of the chip from the workpiece through a fracture mechanism [67] (both of which are orientation dependent).

In the current study, the surface roughness was measured for all the cases with the cleanup cuts. The repetitions of the surface roughness measurements were performed only at six conditions. The surface roughness data was analyzed thorough ANOVA based on the average surface roughness (R_a) values, as shown in Table 5.5, where the statistically *insignificant* effects are italicized. It is seen that the main effects of orientation, rake angle, cutting velocity, and uncut chip thickness, as well as various interaction effects are statistically significant.

The relevant main and interaction effects on average surface roughness are plotted in Fig. 5.15.

Table 5.5: ANOVA results for the surface roughness, where “*” denotes the interaction between two parameters.

Parameter	P (R_a)	F (R_a)
Orientation (e_1)	0.000	47.07
α (e_2)	0.000	51.39
v (e_3)	0.023	5.20
h (e_4)	0.000	42.40
$e_1^*e_2$	0.000	3.38
$e_1^*e_3$	0.801	0.69
$e_1^*e_4$	0.001	2.16
$e_2^*e_3$	0.121	2.13
$e_2^*e_4$	0.013	3.23
$e_3^*e_4$	0.757	0.28

As seen in Fig. 5.15(a), when averaged over all the cutting conditions, the surface roughness varies strongly with the crystallographic orientation. The largest variation was seen between grains B_2 and B_3 , where the surface roughness of grain B_2 ($R_a = 265$ nm) was seen to be 831% higher than that of grain B_3 ($R_a = 32$ nm). When Figs. 5.15 and 5.7(a) are analyzed, a correlation between the roughness values and the specific energies may be observed: generally, higher roughness values are seen at orientations that result in higher specific energies.

Averaging over all the crystallographic orientations, the surface roughness was seen to increase with reducing rake angle, increasing uncut chip thickness, and reducing cutting speed. The average R_a values at 0 degree rake angle are higher than those at 25 degree rake angle by 90%, and the average R_a values at 40 μm uncut chip thickness are higher than those at 10 μm by 85%.

The interaction effect between the crystallographic orientation and the rake angle is shown in Fig. 5.15(e). It is seen that the effect of rake angle on average surface roughness varies at different crystallographic orientations. Similarly, the interaction effect between the crystallographic orientation and the uncut chip thickness is shown in Fig. 5.15(f). Generally, the surface roughness variations across the grains are seen to be smaller at lower uncut chip thicknesses. However, in many orientations, especially those that produce lower R_a values, the surface roughness variations does not change significantly with the uncut chip thickness. It is possible that this low level of surface roughness is an inherent limitation of the experimental setup, and is uniform across different grain orientations and uncut chip thicknesses.

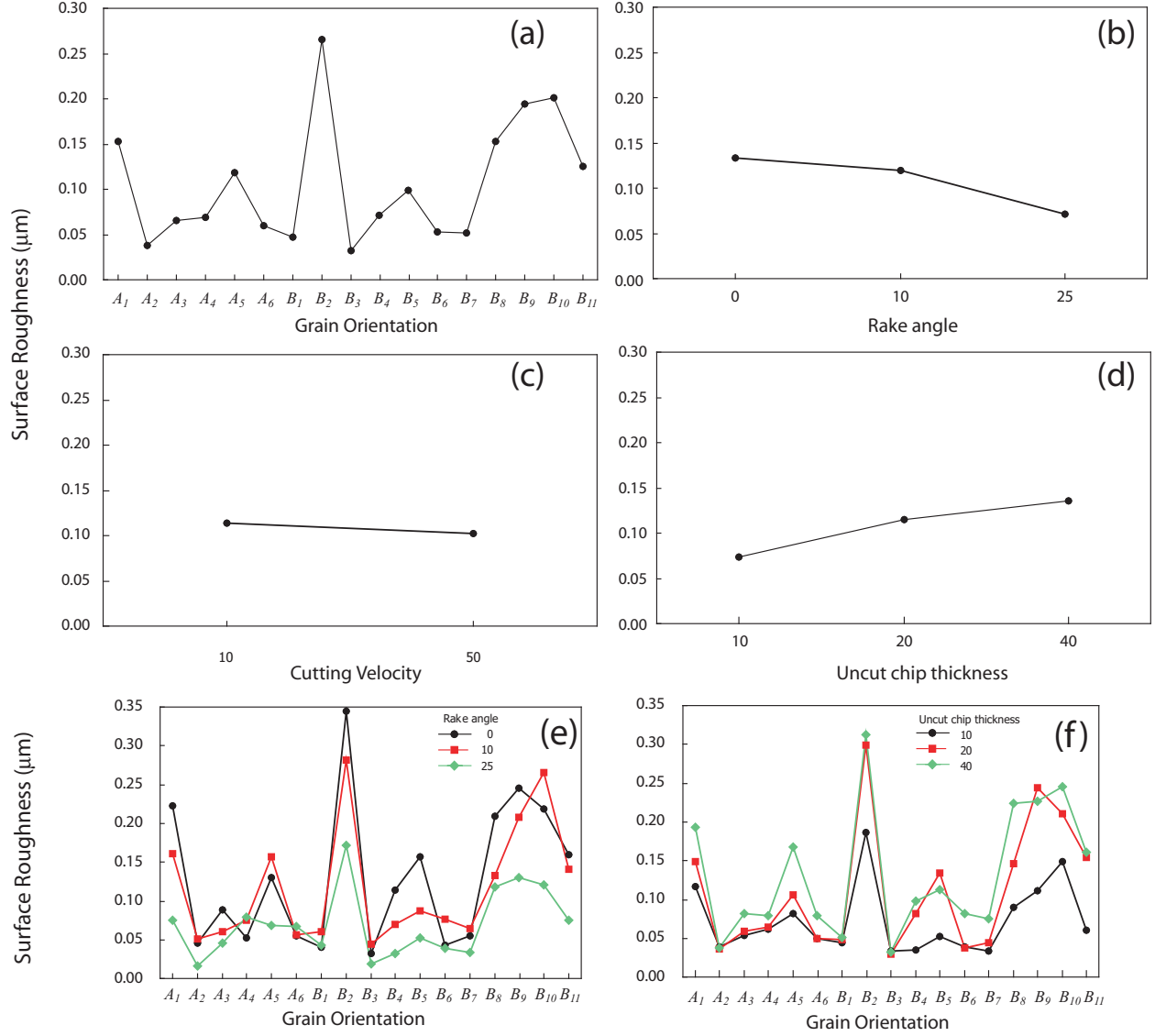


Figure 5.15: (a-d) Main effect plots for surface roughness, and (e-f) Two- way interaction effects for surface roughness between (e) the grain orientation and the rake angle, and (f) the grain orientation and the uncut chip thickness.

5.3 Comparison with the model

The observed experimental variation in specific cutting energy for the with-cleanup tests was also compared with the predicted variation from the RSPM model. While a recalibration of the model is necessary for performing an one to one comparison, the trends in variation with orientation can be compared using the material constants calibrated earlier (see Table 3.1) for pure aluminum. A constant uniform coefficient of friction (dependent on the rake angle) obtained from the experiments

was used for all the orientations at every rake angle.

For comparison with the model the specific cutting energies were averaged over cutting conditions (cutting velocity and uncut chip thickness) at each rake angle for every orientation. Qualitatively, it was observed that the predictions from the RSPM model followed the experimental behavior better at higher rake angle. The statistical R package was used to quantify the correlation between the experimental results and the model predictions.

The preliminary results from the statistical tests gave correlation coefficients of 0.04, 0.35, 0.71 at 0 degree, 10 degree and 25 degree rake angles, respectively, between the experimental and the simulated specific cutting energies. A higher correlation coefficient indicates a better match, with a correlation coefficient of 1 indicating a strong linear relationship between the two. The variations in specific cutting energies are compared in Fig. 5.16 for the 25 degree rake angle case. The magnitudes of the predicted specific energies are scaled uniformly in Fig. 5.16(b) to obtain the same average (over all orientations) specific energy value observed in experiment.

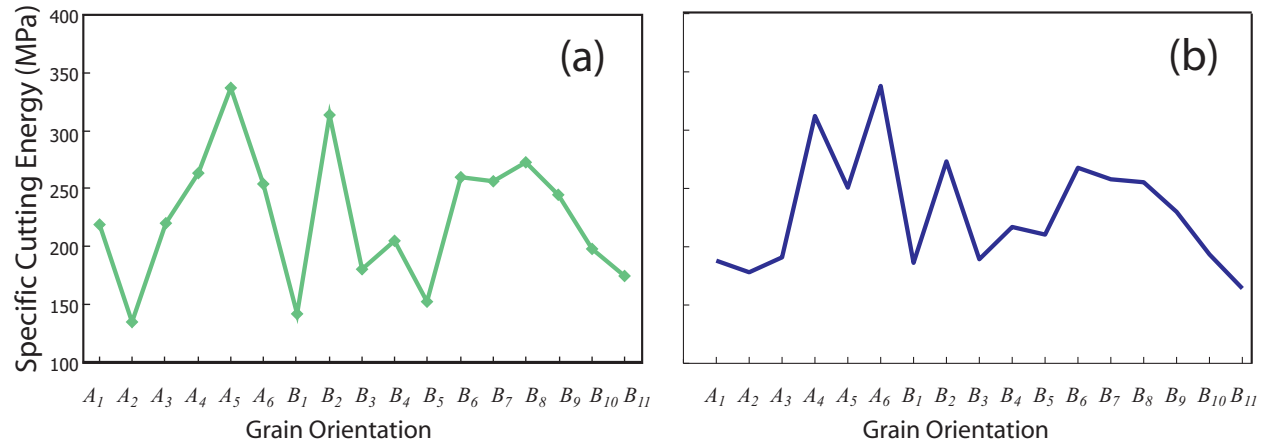


Figure 5.16: Comparison between (a) Experimental specific cutting energy and (b) Predicted specific energy (scaled) from the RSPM model, at 25 degree rake angle

Since the model relies on many simplifying assumptions, the predictive capability of the model is tied to the applicability of the underlying assumptions. In particular, the model assumes an uniform, thin and straight shear zone. At lower rake angles, the shear zone is thicker, not straight and most importantly not uniform. Hence, it is expected that the predictions from the model will follow the experimental observations better at higher rake angles.

5.4 Summary

This chapter presented an experimental analysis of orthogonal machining of coarse-grained aluminum including the crystallographic anisotropy. A planing setup is used to conduct experiments with a full-factorial design including 17 crystallographic orientations and varying cutting conditions, and the specific cutting energies and effective coefficients of friction were calculated from the measured forces. Multi-variate analysis of variance was used to assess the repeatability and statistical significance of different parameters and their interaction with crystallographic orientations. The tests with and without cleanup cuts were performed to determine the effect of subsurface damage and its interaction with crystallographic effects.

The effect of crystallographic anisotropy on specific cutting energy was seen to be strong, resulting in 360% variation for the experimental conditions and crystallographic orientations considered in this work. The effects of cutting conditions, when averaged over crystallographic orientations, was seen to follow those seen during machining of isotropic materials: the specific cutting energy was seen to increase with reducing rake angle, increasing cutting velocity, and reducing uncut chip thickness. The effect of anisotropy was seen to be stronger at lower rake angles; the maximum variation in specific cutting energy was 415% at 0 degree rake angle and 250% at 25 degree rake angle. The interaction effect between the cutting velocity and orientation was seen to be statistically insignificant, indicating that the effect of velocity was uniform across all orientations for the range of velocities considered in this study. Furthermore, the well-known size effect was observed in all orientations, and the amount of size effect was seen to be orientation dependent.

An equivalent coefficient of friction was calculated to facilitate analyzing different components of machining forces and different specific energies. The variation in the effective coefficient of friction (friction angle) was seen to be only between 4 degrees to 5.7 degrees for most crystallographic orientations. Based on the available data, when modeling the effects of anisotropy in machining, using a constant coefficient of friction could be a good approximation.

Comparing the results from the experiments without cleanup cuts to those with cleanup cuts, it was observed that the presence of larger subsurface deformation reduces the average (across cutting parameters and orientations) specific cutting energy. At lower rake angles, the effect of subsurface deformation was seen to be stronger: the specific cutting energies with cleanup cuts were higher by 8.7%, 29% and 45% at 25 degree, 10 degree and 0 degree rake angles, respectively. The effect of subsurface damage was also seen to be strongly depend upon the crystallographic orientation. Lastly, the subsurface deformation was not seen to influence the effective coefficient of friction

values significantly.

The crystallographic anisotropy was seen to strongly affect the surface roughness: The R_a values varies by as much as 831% due to crystallographic anisotropy. Furthermore, it is observed that the orientations that produce higher specific cutting energies result in higher surface roughnesses and increased uncut chip thicknesses exacerbated the effect of crystallographic anisotropy on surface roughness.

Chapter 6

Experiments on Single Crystal Aluminum

As a part of the research, experiments were also performed on single crystal aluminum to measure the effect of anisotropy during machining. The results from the initial experiments on single crystals are presented in this chapter. Since the infrastructure necessary for performing the complete set of experiments is now available, they will be performed in the near future. The chapter also describes the measurement of subsurface deformation after the machining of single crystal. The measurement technique using the combined OIM and focused ion beam (FIB) equipment not only reveals the extent of sub surface deformation but also the nature of the deformation.

6.1 Orthogonal machining of aluminum single crystals

Orthogonal machining was performed on aluminum single crystals (99.999% pure). The workpieces were created by slicing from larger crystals using wire electro-discharge machining (WEDM)¹. Both plunge turning and planing experiments were performed using a 25 degree rake angle tool while cutting samples with $[0\ 0\ 1]$ zone axis. Plunge turning experiments were also performed on workpieces with $[1\ 1\ 1]$ and $[1\ 0\ 1]$ zone axes, using 25 and 0 degree rake angles, respectively. In both setups, the cutting speed was maintained at 4 mm/s and the cutting depth was 20 μm . Cutting fluid was applied (using a brush) on the rake face prior to the experiments.

The cutting force variation during plunge turning about $[0\ 0\ 1]$ and $[1\ 1\ 1]$ zone axis are shown in

¹A 0.004 inch wire was used for WEDM, larger wires resulted in curling of the slices.

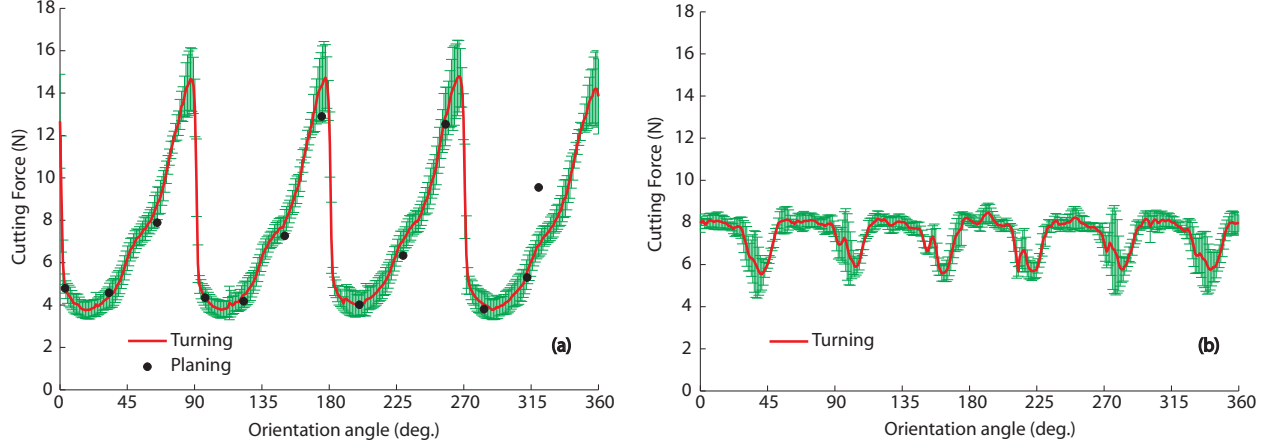


Figure 6.1: Cutting force variation about (a) $[0\ 0\ 1]$ and (b) $[1\ 1\ 1]$ zone axis

Fig. 6.1(a) and (b). The plunge turning force presented in the figure is the mean of data collected over six revolutions, along with the standard deviations indicated. The orientation angle of zero degrees corresponds to the cutting plane normal being $[1\ 0\ 0]$ direction in the case of $[0\ 0\ 1]$ zone axis, and $[1\ 0\ -1]$ direction in the case of $[1\ 1\ 1]$ zone axis. The force variations show expected symmetries (four-fold for $[0\ 0\ 1]$ and six-fold for $[1\ 1\ 1]$ zone axis). The thrust force was observed to follow the cutting force variation in each case.

Planing experiments were performed with the aim of comparing plunge-turning and planing forces. To compare forces, 13 orientations were randomly chosen about the $[0\ 0\ 1]$ zone axis for planing. To eliminate the effects of subsurface deformations, comparisons were made between planing data with and without clean-up cuts (5 cuts of $2\ \mu\text{m}$ deep each); the variations between those cases were found to be minimal. Figure 6.1(a) shows the comparison between cutting forces from planing and plunge turning. For planing, the experimental forces shown are the mean of four cutting passes. It is seen that the plunge turning and planing forces match well (except for one outlier).

Plunge turning experiments were also conducted using small(zero) rake angle. Same cutting conditions as those above were used, except the workpiece zone axis was chosen to be $[1\ 0\ 1]$ direction. The cutting force results from this study exhibited a large variation (the green lines indicating the standard deviation) in forces at certain orientations, as shown in Fig. 6.2(a). When observed closely by superimposing the machining results from consecutive revolutions, it was seen that the forces were alternating between two distinct levels, resulting in large standard deviations. This was also observed when machining at those orientations under planing configuration. The cutting force variation when cut consecutively at one such orientation during planing is shown in

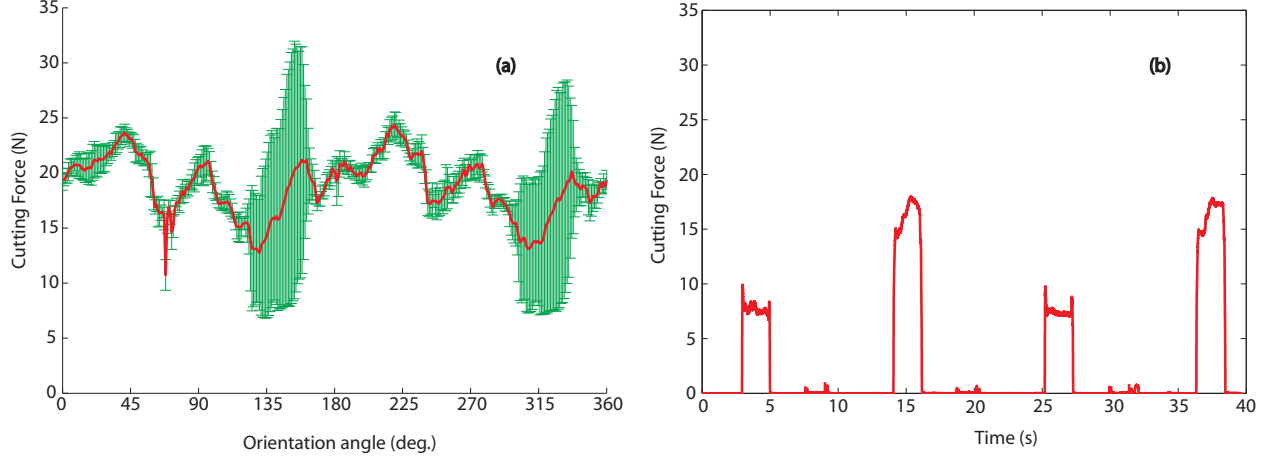


Figure 6.2: Cutting force variation about (a) $[1\ 0\ 1]$ zone axis, and (b) alternation of force at orientation about $[1\ 0\ 1]$ zone axis under planing

Fig. 6.2(b). In the case of planing, when cleanup cuts were performed between consecutive cuts, the force matched closely with the higher values.

A possible cause for such behavior is the subsurface deformation left on the workpiece surface from the previous tool pass. To test this hypothesis, the subsurface deformation in the crystal was subsequently analyzed.

6.1.1 Measurement of subsurface deformation

To analyze the subsurface damage on single-crystal aluminum workpieces, a combined OIM and focused ion beam (FIB) equipment was used. The equipment includes two 180 degrees apart stations for performing the FIB milling to polish the material, and then to subsequently image the polished area using OIM. To prevent the rounding of edge during FIB milling, a platinum layer is deposited on the cut surface as shown in Fig. 6.3(a). The technique also allows observing the changes in orientation below the cut surface. The $[1\ 0\ 1]$ workpiece machined using zero degree rake angle was analyzed for subsurface damage.

The resulting OIM scan on the region is shown in Fig. 6.3(b). Figure 6.3(c) shows the misorientation along the red line in the vertical direction of Fig. 6.3(b). The direction is also shown in Fig. 6.3(b) for clarity. The misorientation profile shows two slopes, while the smaller slope is hypothesized to be due to sample positioning accuracy, resulting in a small variation in the measured orientation over distance, the sudden change in this slope is, on the other hand, indicative of subsurface deformation. The depth at which this slope changes can be considered as a measure for

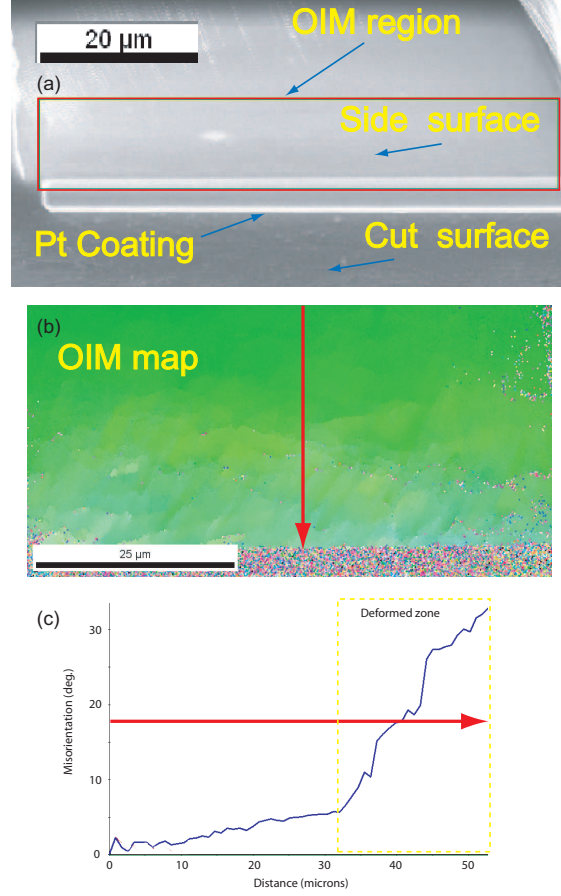


Figure 6.3: Orientation imaging (a) Capping Platinum layer, (b) Orientation map and (c) Misorientation along the depth of workpiece

the depth of subsurface deformation (in the case shown here, it is equal to approximately 20 μm).

Although based on the preliminary subsurface damage data presented (at only one position and orientation) it is hard to conclude whether the alternation of forces is due to sub-surface damage, the misorientation observed could be a potential cause. Considering that the uncut chip thickness was 20 μm for the cut surface, a damage layer of 20 μm implies the cutting orientation was different than the orientation expected from the macro geometry of the single crystal workpiece. As a result, the data for low rake angle machining of single crystals (including the ones in the literature) may not be accurately correlated to the crystallographic orientations.

Chapter 7

Conclusions

The research presented in this work aimed at understanding and predicting the effects of crystallographic anisotropy during machining. Although the presented framework could be applied to other types of crystals, the presented work was specifically focused on fcc metals. In the modeling part of the work, it was observed that by combining the machining kinematics and a shear angle determination scheme originally developed for isotropic materials with the plastic deformation behavior of single crystals, the effects of crystallographic anisotropy on machining forces can be captured. In particular, shear angle determination through minimization of the total power over shear angle candidates, and equations for machining kinematics developed by Merchant [16] provide a suitable framework for incorporating the effects of crystallography. Based on the modeling work, the following specific conclusions are obtained.

- The simplified model obtained by capturing the crystallographic effects through Bishop and Hill's micro-plasticity model can predict magnitude of variations in machining forces due to anisotropy.
- To overcome the deficiencies of the simplified model, it is necessary to incorporate physically realistic effects, including large deformations, strain hardening, and lattice rotation. Inclusion of these effects requires the knowledge of slip on individual slip system for any given amount of deformation. Consequently, rate sensitive constitutive equations are required for determining the slip rates uniquely on individual slip systems. To address these needs, a rate sensitive plasticity based machining (RSPM) model has been developed.
- Compared to the simplified model, the RSPM model is able to capture more accurately the

variations of specific energies (forces) with the crystallographic orientation during orthogonal cutting of single-crystal fcc metals.

- A further simplification for both models could be obtained by circumventing the power minimization procedure, and instead utilizing the Merchant's shear angle solution, to determine the shear angle. This simplification is successful in capturing the magnitude of variation observed in forces for a fraction of computational burden.

The experimental work has been successful in quantifying the effects of anisotropy on machining forces and surface finish. In addition to the effects of anisotropy, the interaction between the anisotropy and machining parameters were also explored. From the machining experiments on coarse grained polycrystal and single crystals, the following specific conclusions are obtained.

- From the machining experiments on polycrystal, when the results are averaged over responses from individual crystals from 17 or more orientations, the effect of the machining parameters follow the behavior that is seen at the macro scale on effectively-isotropic materials. More specifically, the specific cutting energy was seen increase with reducing rake angle, increasing cutting velocity, and reducing uncut chip thickness.
- Both specific energy and surface finish are strongly affected by crystallographic anisotropy. The effects of rake angle and uncut chip thickness on specific energy depend upon the orientation of the crystal, whereas the effect of cutting velocity is uniform across all orientations.
- To reduce the effect of the subsurface deformation left by a previously machined surface, multiple small cleanup cuts can be performed. When the cleanup cuts are conducted, with respect to experiments without the cleanup cuts, the effect of anisotropy changes significantly. The specific energies obtained after the cleanup cuts are higher than those obtained without the use of cleanup cuts for all crystals.
- When machining with large (positive) rake angles, the specific energies obtained from plunge-turning experiments, where the crystallographic orientation changes continuously for a fixed zone axis, are equal to those obtained from planing experiments on the same orientations. The latter, however, is significantly more time consuming, since each individual crystal must be separately tested. On the other hand, for small and negative rake angles, the results from the two experimental configurations do not consistently match. During plunge turning of single crystal disks, $[1\ 1\ 1]$ zone axis results in the minimum variation of specific energy out of other zone-axis orientations.

- Subsurface deformation can be experimentally quantified by using a combined FIB and OIM technique. At lower rake angles, the depth of subsurface deformation is commensurate with the uncut chip thickness.

Chapter 8

Future Work

The research conducted as a part of this thesis has created more opportunities to explore and better understand the effects of anisotropy on micromachining. Depending on the nature, scope and available infrastructure, the opportunities are divided into near term and long term future work. The specifics of the two categories are described in the following sections.

8.1 Near Term Work

Considering the fully functional turning and planing experimental set-ups and the single crystal workpieces that have already been procured the following experimental studies will be performed in the near future.

8.1.1 Experimental Measurement of Subsurface Deformation

During the initial experiments it was observed that the subsurface deformation was commensurate with the uncut chip thickness while machining with the zero degree rake angle tool. A deformed subsurface (and the resulting lattice rotation) can result in the cutting orientation being different from the one expected of the single crystal workpiece. Furthermore, the subsurface deformation can cause a polycrystalline region below the cut surface, which can result in the machining response (during subsequent cuts) being different from the response expected from single crystals.

Gaining a through understanding of machining of single crystals would require the study of subsurface deformation, which may be an integral part of the machining response. Furthermore, since the measured forces are compared with the predictions from the model, a possible source

of mismatch between the two is the subsurface deformation. Depending on the extent and the nature of the subsurface deformation, modifications to the model may be required for recreating the experimental conditions while comparing with the experimental results. Hence a systematic measurement of the extent and the nature of subsurface deformation will be performed.

8.1.2 Orthogonal Machining of Single Crystals

Despite the large number of studies in the literature on machining of single crystals, the available force data is scattered sparsely over the possible cutting conditions. As a result, it is difficult to use the available data for validating with the machining models and gaining a thorough understanding on the effects of crystallographic anisotropy. Furthermore, the available data is insufficient to elaborate on the effects of rake angle, cutting velocity and uncut chip thickness while machining single crystal fcc metals. Consequently, there is a strong need for experimental machining study of single crystal over a wide range of cutting conditions.

In the near future, orthogonal planing and orthogonal plunge turning experiments will be performed on single crystal aluminum and the variation in forces and surface finish with orientation will be studied at different cutting conditions. Furthermore, the RSPM model will be recalibrated using newer experimental data. The subsequent model predictions will be compared with the experimental results to analyze the applicability of the model at various cutting conditions.

8.1.3 Oblique Machining of Single Crystals

Realistic machining operations involve complicated tool geometries. While orthogonal machining models and experiments serve as ideal cases which can be extended to complicated machining geometries, it is useful to perform one such extension to the case of oblique machining. Oblique machining geometry results in the tool edge being non perpendicular to the cutting velocity. Unlike orthogonal machining, the deformation during oblique machining is not of plane strain.

In this work, oblique machining experiments will be performed on single crystal aluminum at various inclination angles, rake angles, cutting velocity and uncut chip thickness in both planing and plunge turning set-ups. These experiments will be the first oblique machining experiments performed on single crystals. Furthermore, the RSPM model will be extended to include the oblique machining geometry and used for predicting forces at various inclination angles.

8.2 Long term work

In the longer term, the following tasks are proposed to improve the modeling efforts and obtain additional experimental data.

Non Homogeneity of Deformation

Under the presented modeling efforts the shear zone is assumed to be homogenous. All the material being removed as chip is assumed to undergo the same amount of deformation. Whereas it is known that the shear deformation of the material is inhomogeneous, especially so at lower rake angles. Extending the machining force model to include the inhomogeneity of the shear zone will improve the predictive capability of the model.

Improved Modeling of Rake Face Conditions

Currently a simplified average friction coefficient is used for incorporating rake face friction condition. Such modeling based on Coulomb friction assumption overlooks the complex boundary conditions on the rake face. Using more complicated friction models will aid in capturing the physical behavior more accurately. Researchers have observed a significant shear deformation caused due to rubbing on rake face. As an alternate approach, a second shear deformation (along with the primary shear deformation) applied to the material can aid in capturing the behavior on the rake face.

Improved Hardening Schemes

The current model relies on isotropic hardening (all slip systems harden at the same rate), whereas latent hardening (with inactive slip systems hardening more than active ones) is observed in fcc metals. While latent hardening may not affect the results for orientations in which the slip is accommodated by multiple systems during any point/stage of deformation (in the shear zone), it will affect cases which accommodate slip with few (single/double) slip systems (at any stage). Incorporating latent hardening into the RSPM model may improve the predictive capability of the model.

Extension to Non FCC Metals

Body Centered Cubic (BCC) metals have enough slip systems for accommodating arbitrary strains. Modeling of plasticity in BCC materials can be performed on the lines of FCC materials if restricted glide is considered. The RSPM model can be modified to consider the restricted glide scenario in BCC materials, and the resulting predictions can be compared with the experimental results by machining BCC materials. In the case of Hexagonal close packed (HCP) metals there are

not enough slip systems to accommodate arbitrary strain. Hence, modeling their behavior during machining may be difficult. However, an experimental analysis of the effects of anisotropy during machining of HCP metals can be performed.

Simulation Tool for Predicting Forces for Actual Machining Operations

The oblique machining force model incorporating anisotropy can be combined with the tool geometry and used to predict forces during machining operations like milling and drilling. Since different parts of material may be cutting along different crystallographic directions while machining with complex tools, a chip continuity condition may be necessary for realistic modeling. Such a simulation tool combined with a voxel based microstructure map (obtained from non destructive testing) can be used to predict machining forces for actual workpieces.

Effect of Grain Boundary Character Distribution Apart from crystallographic anisotropy, grain boundary character distribution can also affect the machining response at the micro-scale. Machining across individual grain boundaries cannot be used to quantify the effect of grain boundaries, as the effect crystallographic anisotropy masks the effect of grain boundary character. Alternately, specially prepared grain boundary engineered (GBE) materials can be machined and compared with reference material to observe the effect of Grain boundary character distribution.

Appendix

Schmid tensor and Euler angles

The Schmid tensor for the s -th slip system is given by $(b_s \otimes n_s) + (b_s \otimes n_s)^T$, where b_s is the slip direction and n_s is the slip plane normal. The symmetric part m_s and skew-symmetric part q_s of the Schmid tensor, and can be written as

$$m_s = \frac{(b_s \otimes n_s) + (b_s \otimes n_s)^T}{2} \quad \text{and} \quad q_s = \frac{(b_s \otimes n_s) - (b_s \otimes n_s)^T}{2}.$$

The components of Ω^k are used to update P^k through an Euler angle based update scheme. P^k can be written in terms of three Euler angles, $0 \leq \varphi_1 \leq 2\pi$, $0 \leq \theta \leq \pi$ and $0 \leq \varphi_2 \leq 2\pi$, as

$$P^k = \begin{bmatrix} \cos \varphi_1 \cos \varphi_2 - \sin \varphi_1 \sin \varphi_2 \cos \theta & \sin \varphi_1 \cos \varphi_2 + \cos \varphi_1 \sin \varphi_2 \cos \theta & \sin \varphi_2 \sin \theta \\ -\cos \varphi_1 \sin \varphi_2 - \sin \varphi_1 \cos \varphi_2 \cos \theta & -\sin \varphi_1 \sin \varphi_2 + \cos \varphi_1 \cos \varphi_2 \cos \theta & \cos \varphi_2 \sin \theta \\ \sin \varphi_1 \sin \theta & -\cos \varphi_1 \sin \theta & \cos \theta \end{bmatrix}.$$

P^{k+1} is obtained by updating the Euler angles. The change in Euler angles can be written in terms of components of Ω^k from the following set of equations.

$$\begin{aligned} \Delta \varphi_1 &= \left(\frac{\sin \varphi_2}{\sin \theta} (\Omega^k)_{23} + \frac{\cos \varphi_2}{\sin \theta} (\Omega^k)_{31} \right) \Delta t. \\ \Delta \theta &= (\cos \varphi_2 (\Omega^k)_{23} - \sin \varphi_2 (\Omega^k)_{31}) \Delta t. \\ \Delta \varphi_2 &= -\Delta \varphi_1 \cos \theta + ((\Omega^k)_{12}) \Delta t. \end{aligned}$$

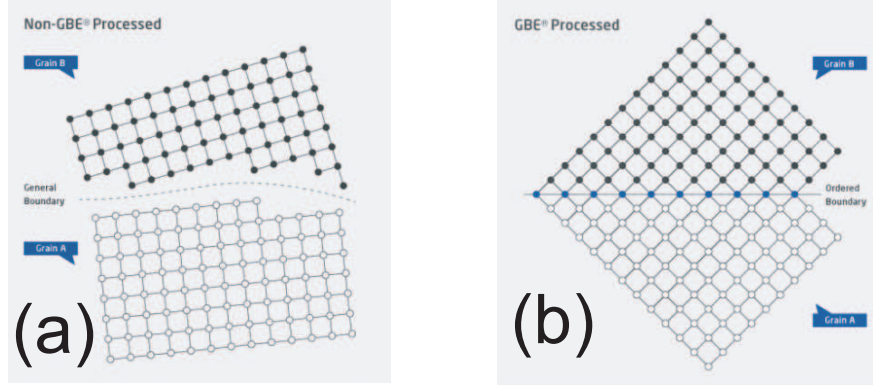


Figure 8.1: (a) Reference nickel and (b) GBE nickel (source:www.integran.com)

Machining of GBE materials

Apart from crystallographic anisotropy, grain boundary character distribution can also affect the machining response at the micro-scale. Machining across individual grain boundaries cannot be used to quantify the effect of grain boundaries, as the effect crystallographic anisotropy masks the effect of grain boundary character. Alternately, specially prepared grain boundary engineered (GBE) materials can be machined and compared with reference material.

To perform such experiments, GBE nickel and reference nickel samples was obtained from Integran. Figure 8.1 shows the difference between the two according to the manufacturer. GBE nickel is seen to have significantly higher proportion of $\Sigma 3, 9, 27$ boundaries [58].

The experiments were performed on the planing apparatus at 2 speeds (2mm/s and 20mm/s) with an uncut chip thickness of 5 μm . Since diamond tools cannot be used with nickel, a carbide tool was used. Typical forces along a length of the workpiece at 20 mm/s cutting speed is shown in Fig. 8.2(a). At least 6 repetitions were performed at each cutting conditions. The forces (mainly cutting) were consistently observed to be higher while cutting reference nickel. However, on close observation it was seen that the reference nickel samples were thicker than GBE nickel samples. Hence the cutting forces were normalized to obtain specific cutting energy and an ANOVA analysis was performed. The resulting main effects and interactions plots are shown in Figs. 8.2(b) and (c). The corresponding F and P values given in Table 8.1 indicate that while the effects of both material and speed on specific energy is statistically significant, the effect of interaction is not.

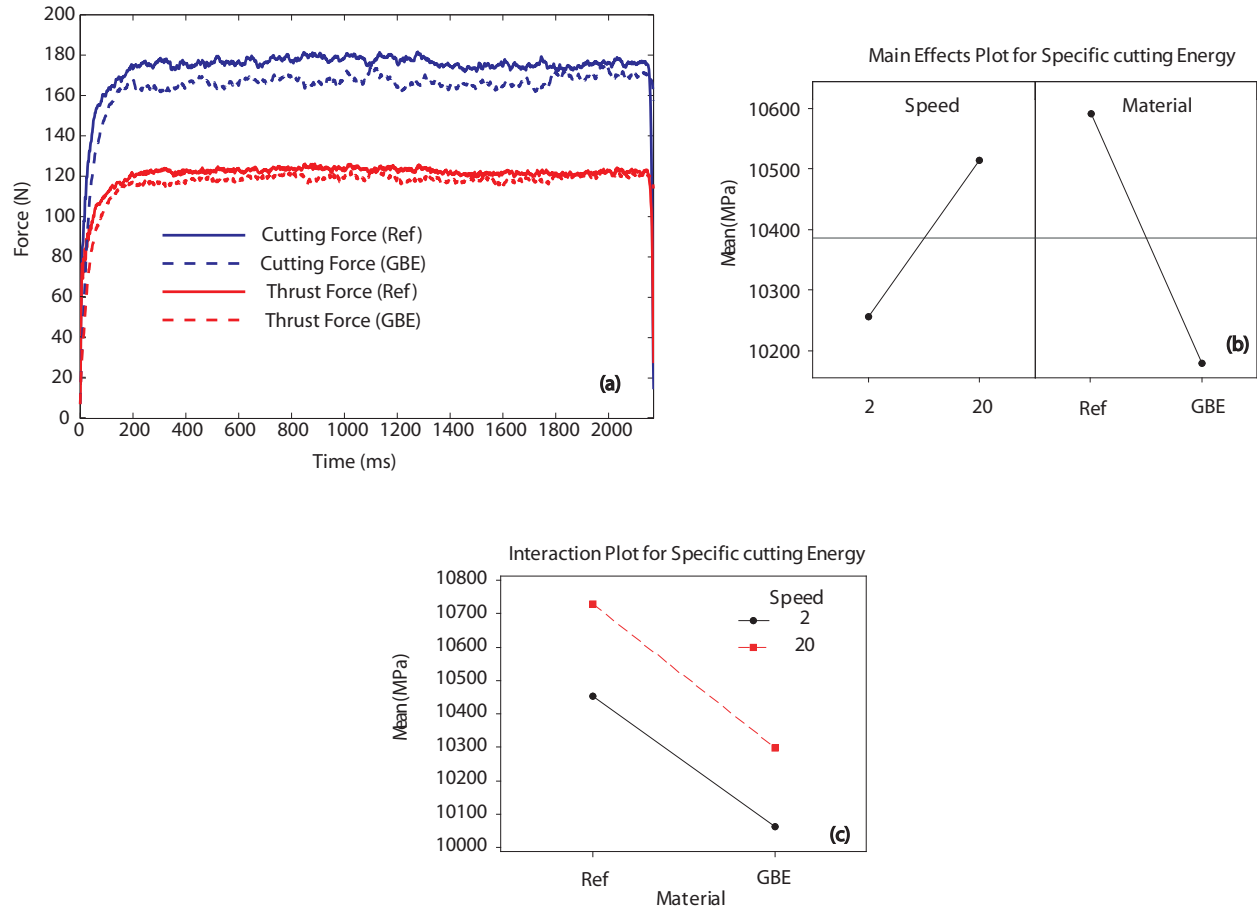


Figure 8.2: (a) Machining force comparison, (b) Main effects plot, and (c) Interaction plot

Table 8.1: ANOVA results for machining of GBE materials.

Parameter	F value	P value
Material	36.22	0.000
Speed	14.19	0.001
Interaction	0.10	0.758

Bibliography

- [1] Benavides, G. L., Adams, D. P., and Yang, P., “Meso-machining capabilities,” Tech. Rep. SAND2001-1708, Sandia National Laboratories, Albuquerque, New Mexico 87185, June 2001.
- [2] *Proceedings of U.S. and International Assessments of Research and Development in Manufacturing*. World Technology Evaluation Center, Inc.
- [3] Wilson, M. E., Kota, N., Kim, Y., Wang, Y., Stolz, D., LeDuc, P. R., and Ozdoganlar, O. B., “Fabrication of Circular Microfluidic Channels by Combining Mechanical Micromilling and Soft Lithography,” *Lab on a Chip*, **11**, pp. 1550-1555.
- [4] Liu, X., DeVor, R. E., Kapoor, S. G., and Ehmann, K. F., 2004, “The mechanics of machining at the microscale: Assessment of the current state of the science,” *Journal of Manufacturing Science and Engineering, Transactions of the ASME*, **126**, pp. 666–678.
- [5] Filiz, S., Conley, C., Wasserman, M., and Ozdoganlar, O. B., 2007, “An experimental investigation of micro-machinability of copper 101 using tungsten carbide micro-endmills,” *International Journal of Machine Tools and Manufacture*, **47**, pp. 1088–1100.
- [6] Xie, L., Brownridge, S. D., Ozdoganlar, O. B., and Weiss, L. E., 2006, “The viability of micromilling for manufacturing mechanical attachment components for medical applications,” *Transactions of the North American Manufacturing Research Institute of SME*, **34**, pp. 445–452.
- [7] Filiz, S., Xie, L., Weiss, L., Ozdoganlar, O. B., 2008, “Micromilling of microbarbs for medical implants,” *International Journal of Machine Tools and Manufacture*, **48**, 459–472.
- [8] Kim, C. J., Bono, M., and Ni, J., 2002, “Experimental analysis of chip formation in micro-milling,” *Transactions of NAMRI/SME*, **30**, pp. 247–254.

- [9] Vogler, M. P., DeVor, R. E., and Kapoor, S. G., “On the modeling and analysis of machine performance in micro-endmilling, part 1: Surface generation,” *Journal of Manufacturing Science and Engineering, Transactions of the ASME*, **126**, no. 4, pp. 685–694.
- [10] Vogler, M. P., DeVor, R. E., and Kapoor, S. G., “On the modeling and analysis of machine performance in micro-endmilling, part 2: Cutting force prediction,” *Journal of Manufacturing Science and Engineering, Transactions of the ASME*, **126**, no. 4, pp. 695–705.
- [11] Dow, T. A. and Scattergood, R. O., 2003, “Mesoscale and microscale manufacturing processes: Challenges for materials, fabrication and metrology,” *Proceedings of the ASPE Winter Topical Meeting*, **28**, pp. 14–19.
- [12] Spath, D. and Huntrup, V., 1999, “Micro-milling of steel for mold manufacturing - influences of material, tools and process parameters,” *Precision Engineering - Nanotechnology: Proceedings of the 1st International euspen conference*, **1**, pp. 203–206.
- [13] Vogler, M. P., DeVor, R. E., and Kapoor, S. G., May 2003, “Microstructure-level force prediction model for micro-milling of multi-phase materials,” *ASME J. of Manufacturing Science and Engineering*, **125**, pp. 202–209.
- [14] Wang, Z. Y., Sahay, C., and Rajurkar, K. P., 1994, “Micro-turning of copper with monocrystal diamond tool,” *Proceedings of the First S.M. Wu Symposium on Manufacturing Science*, **1**, pp. 97–100.
- [15] Trent, E. M., and Wright, P. K., 2000, *Metal Cutting*. Butterworth Heinemann.
- [16] Merchant, M. E., 1945, “Mechanics of metal cutting process. i. orthogonal cutting and a type 2 chip,” *Journal of Applied Physics*, **16**, pp. 267–275.
- [17] Ramalingam, S. and Hazra, J., 1973, “Dynamic shear stress-analysis of single crystal machining studies,” *Trans. ASME, J. Eng. Ind.*, **95B**, pp. 939–944.
- [18] Koenig, W. and Spenrath, N., 1991, “Influence of the crystallographic structure of the substrate material on surface quality and cutting forces in micromachining,” *Proceedings of the International Precision Engineering Seminar*, pp. 141–151.
- [19] Cohen, P. H., 1982, “The orthogonal in-situ machining of single and polycrystalline aluminum and copper,” PhD thesis, Ohio state university.

- [20] To, S., Lee, W. B., and Chan, C. Y., 1997, "Ultraprecision diamond turning of aluminum single crystals," *Journal of Materials Processing Technology*, **63**, pp. 157–162.
- [21] Williams, J. and Horne, J., 1982, "Crystallographic effects in metal cutting," *Journal of Material Science*, **17**, pp. 2618–2624.
- [22] Moriwaki, T., Okuda, K., and Shen, J. G., 1993, "Study on ultraprecision orthogonal micro-diamond cutting of single-crystal copper," *JSME International Journal, Series C: Dynamics, Control, Robotics, Design and Manufacturing*, **36**, pp. 400–406.
- [23] Sato, M., Kato, Y., and Tsutiya, K., 1979, "Effects of crystal orientation on the flow mechanism in cutting aluminum single crystal," *Transactions of the Japanese Institute of Metals*, **20**, pp. 414–422.
- [24] Sato, M., Yamazaki, T., Shimizu, Y., and Takabayashi, T., 1991, "A study on the microcutting of aluminum single crystals," *Japanese Society of Mechanical Engineering International Journal*, **34**, no. 4, pp. 540–545.
- [25] Yuan, Z. J., Lee, W. B., Yao, Y. X., and Zhou, M., 1994, "Effect of crystallographic orientation on cutting forces and surface quality in diamond cutting of single crystal," *CIRP Annals - Manufacturing Technology*, **43**, no. 1, pp. 39–42.
- [26] Lawson, B. L., Kota, N., and Ozdoganlar, O. B., 2008, "Effects of crystallographic anisotropy on orthogonal micromachining of single-crystal aluminum," *Journal of Manufacturing Science and Engineering, Transactions of the ASME*, **130**, no. 3, pp. 0311161–03111611.
- [27] Clarebrough, L. M. and Ogilvie, G. J., "Microstructure by machining," in *Machining Theory and Practice*, pp. 110–121, ASM, 1950.
- [28] Turkovich, B. von and Black, J. T., 1970, "Micro-machining of copper and aluminum crystals," *ASME J. of Engineering for Industry*, **92 Ser B.**, pp. 130–134.
- [29] Black, J. T., 1969, "Plastic deformation in ultramicrotomy of copper and aluminum," PhD thesis, University of Illinois.
- [30] Ueda, K., Iwata, K., and Nakajama, K., 1980, "Chip formation mechanism in single crystal cutting β -brass," *CIRP Annals - Manufacturing Technology*, **29**, no. 1, pp. 41–46.
- [31] Sato, M., Kato, Y., Aoki, S., and Ikoma, A., 1983, "Effects of crystal orientation on the cutting mechanism of aluminum single crystal," *Bulletin of the JSME*, **26**, no. 215, pp. 890–896.

- [32] Black, J. T., 1971, "On the fundamental mechanism of large strain plastic deformation," J. Eng. Ind.-Trans. ASME, **93**, pp. 507–526.
- [33] Black, J. T., 1972, "Shear front-lamella structure in large strain plastic deformation processes," J. Eng. Ind.-Trans. ASME, **94**, pp. 307–316.
- [34] Sato, M., Kato, Y., Tsutiya, K., and Aoki, S., 1981, "Effects of crystal orientation on the cutting mechanism of aluminum single crystal," Bulletin of the JSME, **24**, pp. 1864–1870.
- [35] Willams, J. and Gane, N., 1977, "Some observations on the flow stress of metals during metal cutting," Wear, **42**, pp. 341–353.
- [36] Shirakashi, T., Yoshino, M., and Kurashima, H., 1991, "Study on cutting mechanism of single crystal based on simple shear plane model," International journal of the Japan society for precision engineering, **25**, no. 2, pp. 96–97.
- [37] Lee, W. B. and Zhou, M., 1993, "A theoretical analysis of the effect of crystallographic orientation on chip formation in micromachining," International Journal of Machine Tools and Manufacture, **33**, no. 3, pp. 439–447.
- [38] Lee, W. B., Cheung, C. F., and To, S., 2002, "A microplasticity analysis of micro-cutting force variation in ultra-precision diamond turning," Journal of Manufacturing Science and Engineering, **124**, pp. 170–177.
- [39] Reid, C. N., 1973, *Deformation geometry for material scientists*. Pergamon Press.
- [40] Zhou, M. and Ngoi, B. K. A., 2001, "Effect of tool and workpiece anisotropy on microcutting processes," IMechE Journal of Engineering Manufacture, **215**, pp. 13–19.
- [41] Bishop, J. and Hill, R., 1951, "A theory of the plastic distortion of a polycrystalline aggregate under combined stresses," Philosophical Magazine, **42**, pp. 414–427.
- [42] Hill, R., 1950, *Mathematical Theory of Plasticity*. Oxford.
- [43] Taylor, G. I., 1938, "Plastic strain in metals," J. Inst. Metals, **68**, pp. 307–324.
- [44] Chin, G. Y. and Mammel, W. L., 1969, "Generalization and equivalence of the minimum work -taylor, and maximum work -bishop-hill- principles for crystal plasticity," Trans. Met. Soc. AIME., **245**, pp. 1211–1214.

- [45] Kota, N. and Ozdoganlar, O., 2010, “A model-based analysis of orthogonal cutting for single-crystal fcc metals including crystallographic anisotropy,” *Machining Science and Technology*, **14**, no. 1, pp. 102–127.
- [46] Altintas, Y., 2000, *Manufacturing Automation: Metal Cutting Mechanics, Machine Tool Vibrations, and CNC Design Manufacturing Automation: Metal Cutting Mechanics, Machine Tool Vibrations, and Cnc Design*. Cambridge University Press.
- [47] Kocks, U. F., Tome, C. N., and Wenk, H. R., (Eds.), 1998, *Texture and Anisotropy: Preferred Orientations in Polycrystals and their Effect on Materials Properties*. Cambridge University Press.
- [48] Kota, N. and Ozdoganlar, O. B., 2008, “A Simplified Model for Orthogonal Micromachining of fcc Single-Crystal Materials,” *Transactions of NAMRI/SME*, **36**, pp. 193–200
- [49] Jog, C. S., 2002, *Foundations and Applications of Mechanics: Continuum Mechanics, Volume I*. Narosa.
- [50] Oxley, P. L. B., 1989, *The mechanics of machining an analytical approach to assessing machinability*. Halsted Press.
- [51] Dunne, F., and Petrinic, N., 2005, *Introduction to computational plasticity*. Oxford University Press.
- [52] Chandrasekharan, V., Kapoor, S. G., and Devor, R. E., 1995, “A mechanistic approach to predicting the cutting forces in drilling : with application to fiber-reinforced composite materials,” *J. Eng. Ind.-Trans. ASME*, **117**, pp. 559–570.
- [53] Sasena, M. J., 2002, “Flexibility and Efficiency Enhancements for Constrained Global Design Optimization with Kriging Approximations,” PhD Thesis, University of Michigan, Ann Arbor.
- [54] Ikawa, N., Donaldson, R., Komanduri, R., Koenig, W., Aachen, T., McKeown, P., Moriwaki, T., and Stowers, I., 1991, “Ultraprecision metal cutting. the past, the present and the future,” *CIRP Annals - Manufacturing Technology*, **40**, no. 2, pp. 587–594.
- [55] Lucca, D. A. and Seo, Y. W., 1993, “Effect of tool edge geometry on energy dissipation in ultraprecision machining,” *CIRP Annals - Manufacturing Technology*, **42**, no. 1, pp. 83–86.
- [56] Drescher, J., 1993, “Scanning electron microscopic technique for imaging a diamond tool edge,” *Precision Engineering*, **15**, no. 1, pp. 112–114.

- [57] Evans, C., Polvani, R., Postek, M., and Rhorer, R., 1987, “Some observations on tool sharpness and sub-surface damage in single point diamond turning,” SPIE, **802**, pp. 52–66.
- [58] Randle, V., Rohrer, G. S., Miller, H. M., Coleman, M., and Owen, G. T., 2008, “Five-parameter grain boundary distribution of commercially grain boundary engineered nickel and copper,” *Acta Materialia*, **56**, pp. 2363–2373.
- [59] Kota, N. and Ozdoganlar, O. B., 2011, “A Simplified Model for Orthogonal Micromachining of fcc Single-Crystal Materials,” Accepted for publication in Transactions of the North American Manufacturing Research Institution of SME.
- [60] Bitans, K. and Brown, R. H., 1965, “An investigation of the deformation in orthogonal cutting,” *International Journal of Machine Tool Design and Research*, **5**, no. 3, pp. 155–165.
- [61] Backer, W. R., Marshall, E. R., and Shaw, M. C., 1952, *The Size Effect in Metal Cutting*, Trans. ASME, **74**, pp. 61
- [62] Dinesh, D., Swaminathan, S., Chandrasekar, S., and Farris, T. N., 2001, *An Intrinsic Size Effect in Machining due to the Strain Gradient*, Proc. of ASME IMECE, Nov 1116, NY, USA, CD-ROM Proc., pp. 1-8.
- [63] Joshi, S. S. and Melkote, S. N., 2004, “An explanation for the size-effect in machining using strain gradient plasticity,” *Journal of manufacturing science and engineering*, **126**, pp. 679–684.
- [64] Atkins, A. G., “Modelling metal cutting using modern ductile fracture mechanics: quantitative explanations for some longstanding problems,” *International journal of mechanical sciences*, **45**, no. 2, pp. 373–396.
- [65] DeVor, R., Chang, T., and Sutherland, J., 1992, *Statistical quality design and control: contemporary concepts and methods*. MacMillan Publishing Company, New York, NY.
- [66] Sato, M., Yamazaki, T., and Kubo, M., 1985, “The Cutting Mechanism of an Aluminum Single Crystal based on the Crystal Slip Theory,” *Transactions of the Japan Institute of Metals*, **26**, no. 4, pp. 251–258.
- [67] Subbiah, S. and Melkote, S. N., 2007, “Evidence of ductile tearing ahead of the cutting tool and modeling the energy consumed in material separation in micro-cutting,” *Journal of engineering materials and technology*, **129**, pp. 321–331.